Altered 3D Vascular Architecture and Cerebral Blood Flow in a Mouse Model of TBI

by

Joe Steinman

A thesis submitted in conformity with the requirements
for the degree of Doctor of Philosophy
Graduate Department of Medical Biophysics
University of Toronto

Altered 3D Vascular Architecture and Cerebral Blood Flow in a Mouse Model of TBI

Joe Steinman

Graduate Department of Medical Biophysics

University of Toronto

Abstract

It is established in traumatic brain injury (TBI) animal models that the vasculature undergoes loss and recovery. Although past studies have correlated vascular structural alterations with cerebral blood flow (CBF) changes or functional outcome, analysis has largely focused on histological measures of vessel density and diameter. However, it is the 3D organization of cerebral blood vessels that determines the overall capacity of the cerebral circulation to meet the metabolic requirements of the brain. To examine function and 3D organization in the same mouse brain, a methodology was developed combining in vivo Arterial Spin Labeling (ASL) MRI to quantify blood flow under rest and hypercapnia followed by ex vivo 2-photon fluorescence microscopy (2PFM) to quantify 3D vascular structure. Application of this methodology to a controlled cortical impact mouse model of TBI enabled analysis of the evolution of vascular architecture and its relation to blood flow. Despite early (1-day) loss of vasculature, vessel density and vascular volume recovered 1-month post-TBI. However, the reorganized vasculature possessed a radial pattern that corresponded to low blood flow. Since these microvascular alterations are difficult to directly detect with in vivo technologies, ultrasound wave reflection analysis was applied to the carotid arteries of these mice. It was demonstrated that quantification of cerebral vascular resistance with ultrasound has the potential to detect whether a mouse received a TBI. Ultrasound therefore may present an efficient, non-invasive method for detecting TBI via changes in vascular architecture.

Acknowledgements

I should like to thank the following Senior Scientists and supervisors, research staff, and colleagues for their unwavering encouragement, support, assistance, patience, and stellar and solid advice and wisdom throughout my MSc and PhD studies in Medical Biophysics at the University of Toronto.

Dr. John Sled was my supervisor and Principal Investigator throughout my Graduate studies. His support and encouragement were endless. I appreciate our weekly meetings and the time and care Dr. Sled provided. He was always available to discuss my project and provided much guidance and support. He has helped me grow as a scientist and encouraged me to develop necessary research skills, such as computer programing and understanding imaging technologies.

Dr. Sled stressed thoroughness, critical thinking, and analysis as essential in advancing research. In addition to his extensive knowledge and expertise in imaging physics and vasculature, he was collegial in his approach, reaching out to colleagues. The view was to incorporate diverse ideas and views to produce the best possible research. He is an excellent mentor and the lessons he taught me will be influential in shaping my career.

I would like to thank Dr. Lindsay Cahill, Research Associate in the Sled Lab, for many discussions, performing the MRI acquisition for the TBI experiments, helping with ultrasound, answering my numerous questions, and endless patience and thoroughness in the critical review of numerous drafts of my papers. She was integral to my PhD and I am fortunate to have her as a colleague.

Thank you to Margaret Koletar, Research Technician in the Stefanovic Lab, for her invaluable assistance. Her advice and efforts were indispensable to the start-up of this project. She was a perfectionist in all aspects of our mice surgery from preparation to animal recovery. Her instructions on every possible and necessary aspect of surgical techniques enabled my TBI project to become a reality. I recognize the many hours she spent training me on craniotomies and animal surgeries, and that included a visit to Kingston to examine equipment for the project.

Adrienne Dorr, Research Assistant in the Stefanovic Lab, was a true partner and my trainer in 2-photon imaging. I very much appreciate her trip downtown to the Mouse Imaging Centre to provide advice on surgeries and for her experimental assistance in addressing reviewer comments for my first paper. I very much value both Adrienne's and Margaret's contributions to my project.

To Dr. Bob Harrison: Thank you very much for having served as a Committee Member for both my MSc and PhD. Dr. Harrison's comments during our committee meetings were insightful and focused on addressing relevant biological questions. I enjoyed our discussions during the years, and I appreciate his taking an interest in me and my project.

I appreciate Dr. Hutchison's efforts and support as a PhD Committee Member. His clinical experience as a Critical Care specialist was invaluable and he gave me a new perspective on the field of TBI. I appreciate the opportunity to speak at the SickKids 5T TBI group and his advice to present at the CTRC Meeting at the end of my PhD. Our early discussions on choosing a TBI model and research directions to explore were extremely helpful in designing the PhD project.

I would like to thank Dr. Bojana Stefanovic, a Committee Member during the MSc and PhD. She welcomed me into her lab as a collaborator and was always available for meetings. She was generous in providing access to research members of her lab, as well as her 2-photon imaging lab equipment. This assistance was integral to both the MSc and PhD, and served as a catalyst in the development of my interest in 2-photon microscopy. She was, in addition, insightful and enthusiastic in critiquing my drafts. Her comments and inputs were highly useful.

I would like to thank Dr. Mark Henkelman, Director of the Mouse Imaging Centre. He served on my MSc Committee, and took an interest in my project and personal development as a scientist. His appearance at my final committee meeting was a pleasant surprise, where, as always, he provided creative insight and challenged me to think of new angles.

I would like to thank Dr. Chris Macgowan for his willingness to meet and discuss the ultrasound-related aspects of my project. His comments were insightful and extremely helpful.

Thank you to Dr. Greg Stortz from the Macgowan lab for his coding assistance for the ultrasound analysis. He answered all emails promptly and was always available to meet and discuss in depth.

Thank you to Henry Hu, the IT specialist at the Mouse Imaging Centre. Since our research has such a heavy computer-element, his assistance is critical. His efforts in troubleshooting technological issues are prompt, reliable, and excellent. He was particularly helpful in solving problems related to TissueVision, to ensure my project continued to progress at an appropriate pace.

Finally, thank you to my parents for their unwavering support and encouragement.

Table of Contents

List of Tables

List of Figures

Supplemental Figures

List of Abbreviations

2D	2-dimensional
2PFM	2-photon fluorescence microscopy
3D	3-dimensional
α-SMA	alpha smooth muscle actin
ASL MRI	Arterial Spin Labeling Magnetic Resonance Imaging
AUC	area under the receiver operating characteristics curve
BDNF	brain-derived neurotrophic factor
CASL	continuous Arterial Spin Labeling
CBF	cerebral blood flow
CBV	cerebral blood volume
CCI	controlled cortical impact
CCP	critical closing pressure
CI	confidence interval
CNR	contrast to noise ratio
CO_2	carbon dioxide
COV	coefficient of variation
CPP	cerebral perfusion pressure
CT	computed tomography
DAI	diffuse axonal injury
DMSO	dimethyl sulfoxide
EEG	electroencephalography
FITC	fluorescein isothiocyanate
FOV	field-of-view
FPI	fluid percussion injury
FWHM	full-width-half-maximum
GFP	green fluorescent protein

ICP	intracranial pressure
LCCA	left common carotid artery
LDA	linear discriminant analysis
MCA	middle cerebral artery
MIP	maximum intensity projection
O_2	oxygen
PASL	pulsed Arterial Spin Labeling
PBS	phosphate buffered saline
PFA	paraformaldehyde
PI	pulsatility index
PSF	point spread function
PWV	pulse wave velocity
RBC	red blood cell
RCCA	right common carotid artery
RF	radio-frequency
ROC	receiver operating characteristics curve
SNR	signal-to-noise ratio
STPT	Serial Two-Photon Tomography
TBI	traumatic brain injury
TCD	transcranial Doppler
VEGF	vascular endothelial growth factor
TPS	thin plate splines

Chapter 1

Introduction and Overview

This thesis analyzes 3D vascular structure and function in a mouse traumatic brain injury (TBI) model through development of an imaging methodology combining optical measurements of vascular architecture with mesoscopic blood flow imaging. The background to the research is introduced in Chapter 1. The findings and a description of the experimental design are detailed in the main body of the thesis (Chapters 2 – 4).

The goal of Chapter 1 is to provide a motivation for the thesis and highlight the current state of knowledge on the cerebral vasculature, TBI research, vascular injury, and imaging of vascular structure and function. This background provides context for the techniques and findings described in Chapters 2 – 4.

The Introduction is divided into separate sections, with each considering a separate theme. The first outlines the motivation for the research. The second discusses the structure and function of vascular architecture in the brain, and its alteration in disease. Animal models of TBI are highlighted, together with the effects of TBI on the vasculature. Techniques for probing vascular structure and function are examined, specifically microscopy [1], Arterial Spin Labeling (ASL) MRI for perfusion imaging [2, 3], and ultrasound [4].

1.1 Motivation

The cerebral vasculature transports oxygen, glucose, and nutrients (such as vitamins and minerals) throughout the brain. Despite its inability to store glucose in contrast to other organs, the brain accounts for 20 % of the body's resting metabolism [5]. In the healthy adult rodent brain, it is estimated that propagation of action potentials through neurons contribute to nearly half (47 %) the energy expenditure. There is additional consumption of energy due to postsynaptic effects of glutamate (estimated at 34 %) and the maintenance of the resting potential (estimated at 13 %) [5]. These metabolic demands and inability to rely on stored glucose render the brain susceptible to injury where blood flow is reduced. Neuron cell bodies are on average 15 µm from the nearest microvessel [6], with dendritic spines approximately 13 µm from capillaries in healthy tissue [7, 8]. Theoretical models predict that dendrites receive sufficient oxygenation to maintain their dendritic structure if they are within 30 – 40 µm of a flowing vessel [7, 9]. A high density of vessels therefore protects against ischemic occlusion by allowing a 'safety factor' between normal density of vessels and reduced density that leads to impaired neuronal structure or function [6]. Interestingly, dendritic structure is still maintained within 80 µm of a flowing vessel in a mouse model of focal stroke, although it is proposed that astrocytes may increase the diffusion limit by trafficking additional metabolic substrates such as lactate [7, 10].

The cerebral vasculature is plastic, and adjusts its structure in response to environmental factors such as exercise [11] or acquired disease [12, 13]. This plasticity is critical to normal brain development [14] and for restoring tissue oxygenation following stroke [15]. Therapies that increase blood flow via addition of new vessels have been proposed to treat stroke [16] and TBI [17].

The addition of new vessels, however, does not guarantee increased blood flow. In a study by Vogel et al. (2004) [18], vascular endothelial growth factor (VEGF, a signaling molecule that promotes vessel growth) overexpressing mice showed a three-fold increase in capillary density relative to controls, with no observable flow increase [18]. This lack of flow increase is partially attributed by Vogel et al. to ‘vascular architecture’ [18]. Architecture refers to the shape of vessels (ie. curvature, diameter, length) and their topology (their connections in 3D space). These parameters influence flow resistance [19], blood volume [20], transit time (time required for blood to travel through the arterial network; a measure of network efficiency) [12], and vascular reserve (ability to increase flow in response to perturbations) [18]. An understanding of how vascular remodeling impacts blood flow requires consideration of the network architecture in addition to vessel density. As demonstrated in Figure 1.1, two networks with identical vessel numbers may not equally perfuse tissue.

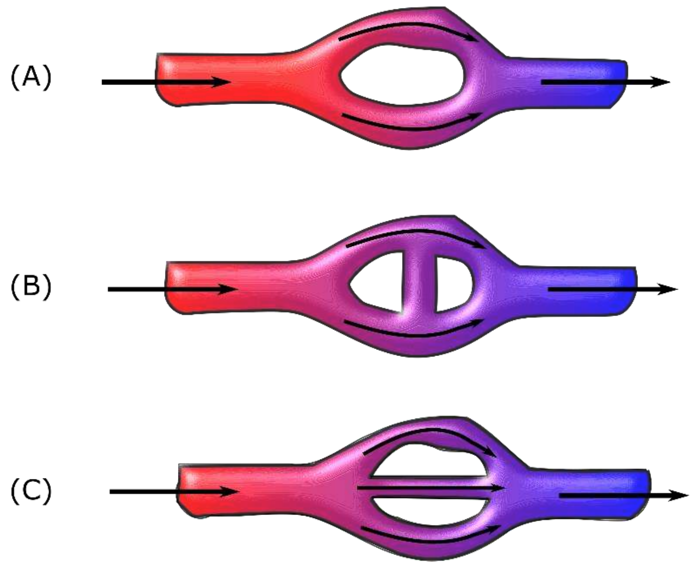

Figure 1.1. Effect of vascular architecture on blood flow. Figure adapted from the study by Vogel et al. [18]. Arrows indicate direction of blood flow, from the arteries (red) to veins (blue). (A) Sketch of a simplified vessel network, with two smaller vessels (capillaries) branching from the input artery. (B) If a new capillary is added to the network perpendicular to the pre-existing capillaries, there is no effect on blood flow (although possibly there are slight differences in tissue oxygenation due to differences in oxygen permeability between a vessel wall and tissue) since the pressure at both endpoints of the capillary is the same, rendering no net driving force across the new capillary. (C) Addition of a capillary in parallel to the pre-existing capillaries will increase flow by increasing the number of pathways for blood and decreasing the overall resistance of the vascular network.

Many studies of vascular remodeling have been based on metrics obtained through 2D microscopy imaging such as density and diameter [21, 22, 23]. In healthy mice, regions of high vascularization display high blood flow [24]. In this situation, 2D analysis of vessel density might be indicative of vascular network function and tissue oxygenation. This relationship may differ in injury or disease. In Alzheimer’s Disease, despite maintenance of capillary density, vessels are tortuous (twisted) and capillaries shrink to form unperfused ‘string’ vessels [25]. These morphological abnormalities are believed to contribute to hypoperfusion [25]. To develop therapies that restore blood flow, an understanding is required of structural mechanisms by which networks remodel during injury, and the functional consequences of these adaptations.

This can be obtained via application of 3D technologies that image both microvascular structure and tissue perfusion.

3D microscopy-based imaging technologies and analysis techniques have been developed for visualizing and segmenting the microvasculature in large volumes of brain tissue [26, 27, 28]. Since these techniques are not combined with blood flow measurements, they provide only structural information, rendering it difficult to determine how structural changes influence flow. This is ultimately significant because studies that apply these techniques would only be able to compare vascular phenotypes between healthy mice and those with acquired disease. Applicability in humans is limited without knowledge of microvascular structure and blood flow relations.

This thesis: (1) Develops an imaging methodology for quantification of vascular structure and cerebral blood flow; (2) Applies this methodology to understand the evolution of vascular structure and function following brain injury; (3) Applies an ultrasound wave reflection technique for non-invasive in vivo detection of changes in vascular architecture.

The imaging methodology that is presented combines an ex vivo 2-photon fluorescence microscopy imaging technique, Serial Two-Photon Tomography (STPT) [29], with in vivo Arterial Spin Labeling (ASL) MRI. STPT is used to obtain images at an isotropic voxel size of 2 µm, enabling 3D capillary quantification and analysis. Through registration of the STPT data to the ASL MRI images, perfusion at each ASL voxel is correlated with vascular structure. Since STPT is ex vivo, this methodology cannot be translated to the clinic. Ultrasound wave reflection is therefore proposed as an alternative, non-invasive method for cerebrovascular quantification.

This combined imaging approach is applied to a mouse model of TBI. This model was selected to study vascular remodeling since animals exposed to injury undergo loss and recovery of cerebral vasculature [21], with reductions in blood flow and abnormalities in vascular structure that persist weeks to months following the initial injury [30, 31]. This is described in further detail later in this chapter. In humans, there is significant variation in the type and severity of brain injury [32]. Animal TBI models enable precise control of biomechanical injury parameters, minimizing between-sample variation. Overall, mice serve as a controlled model system for studying abnormal vascular remodeling in brain tissue following injury.

1.2 Cerebrovascular Architecture and Traumatic Brain Injury

The cerebral vasculature transports blood over long distances across the cortical surface, delivering the blood to capillary beds inside the brain to oxygenate the tissue. This section describes vascular architecture in healthy and diseased mice as a basis for understanding the functional significance of changes to blood vessel structure. Prior to outlining the TBI animal models, general concepts in TBI are described such as primary and secondary injuries, and focal and diffuse injuries. These details are important for understanding how TBI animal models characterize aspects of the human condition. A review of the effects of TBI on vascular structure and function is provided.

1.2.1 Cerebral vascular architecture and function

Mice possess higher neuronal and vessel density than humans, although vascular architecture and topology are similar between mammals [6]. The vascular network in both species consists of pial vessels (large diameter vessels at the cortical surface) and penetrating vessels that enter the cortex at right angles to deliver blood into the capillary bed that permeates tissue.

The pial network is composed of a backbone of 2D interconnected loops [33]. As demonstrated with fluorescence microscopy in rodents, these loops comprise fewer than 10 % of all branches on the cortical surface, while more than 80 % of offshoots from the loops end in a penetrating arteriole [33]. Loops re-route blood flow following occlusion of a single vessel within a loop, ensuring neuronal viability even if local flow is reduced [33]. The large diameters of pial vessels enable transport of blood across the cortical surface with minimal resistance. Capillaries, less than 8 – 10 μm in diameter, are the smallest vessels with a wall thickness of one cell layer. Values of microvessel/capillary density typically range from about 600 – 1300 mm/mm^3, depending on brain region or cortical layer [34]. For example, capillary density in the CA1 of hippocampus is approximately 600 mm/mm^3, 700 mm/mm^3 in layers 2/3 of auditory cortex, and over 1000 mm/mm^3 in layer 4 of auditory cortex [34]. Similar to the pial vasculature, the 3D capillary network is comprised of loops, although with a greater number of branches compared to the pial vasculature [35]. These loops protect against the effects of occlusion, with only a minute volume of microinfarct produced following blockage of individual capillaries two or more branch points away from a penetrating vessel [36]. Nevertheless, their collateral flow does not overcome occlusion of single penetrating vessels. This leads to perfusion loss in a columnar region approximately 0.5 mm in diameter, as demonstrated both in vivo in rodents and through numerical simulations [35]. The perfusion loss is attributed to venules acting as low pressure 'sinks' which shunt flow from neighbouring penetrating arterioles and prevent perfusion of the capillary bed which normally receives blood from the occluded vessel [35]. Due to their thin walls, oxygen diffuses from capillaries to support tissue metabolic processes such as neurotransmitter recycling, intracellular signaling, axonal transport, and CO_2 and metabolic waste removal.

Penetrating arterioles and venules enter the cortex at right angles to the cortical surface, connecting the pial vasculature with the subsurface capillary network. Flow through the vessel network depends significantly on the tone of the penetrating arterioles, with their smooth muscle cells enabling them to contract or dilate, dictating overall network resistance. As blood flows through the network and oxygen diffuses from the arterioles and capillary bed, there is a reduction in the oxygen tension. Sakadzic et al. (2014) [37] used 2-photon fluorescence microscopy to map oxygen partial pressure (PO_2) in isoflurane anesthetized mice. They found PO_2 values above 100 mmHg for pial arterioles with diameters larger than 40 µm, about 65 mmHg for the smallest arterioles less than 10 µm diameter, 36 – 56 mmHg for capillaries, and 35 – 48 mmHg for venules [37]. See Figure 1.2 for an image of the cortical vasculature.

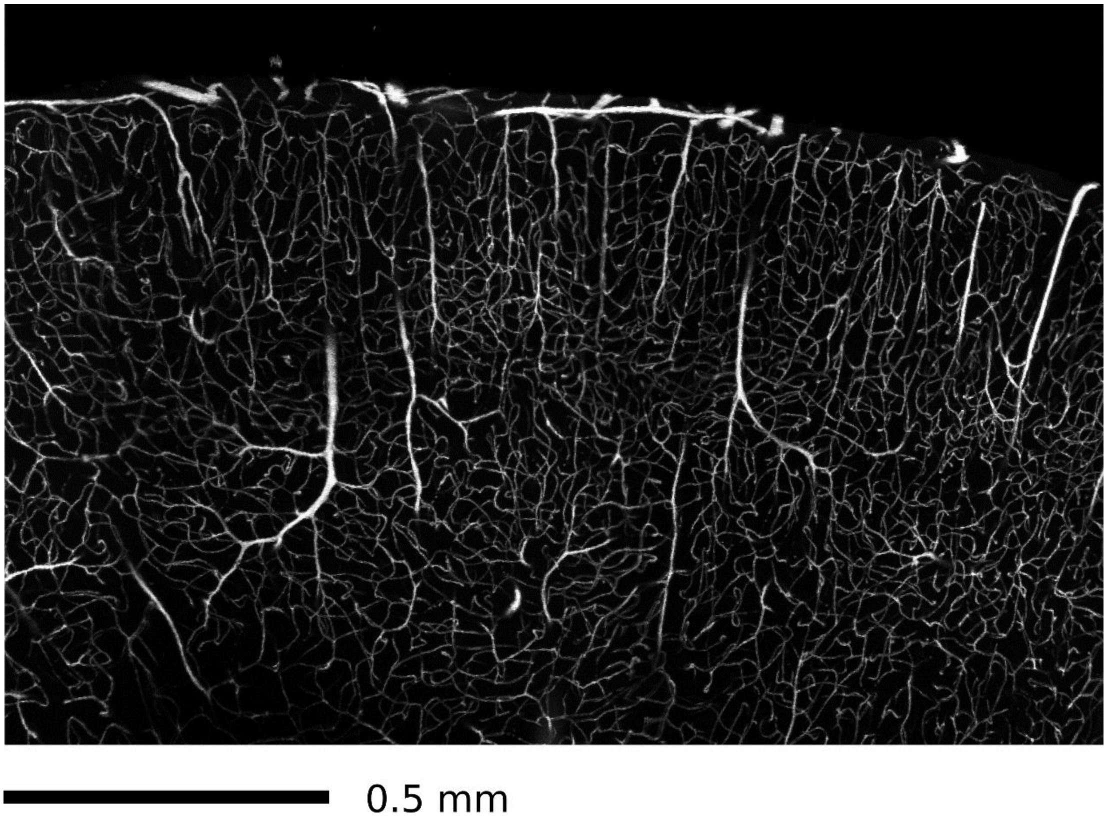

Figure 1.2. Cortical vascular architecture. Maximum intensity projection image of a 100 µm-thick mouse brain coronal section. Vessels were perfused with a FITC fluorescent gel and imaged at 920 nm with a 2-photon fluorescence microscope.

Abnormal architecture is frequently a feature of disease. In Alzheimer's, increased vessel density is common in humans and rodents [38, 39]. This density does not correlate with flow increases, as demonstrated in a study combining whole-brain microscopy with ASL MRI in mice [39]. This could be due to the presence of non-functional, degenerating capillaries which promote hypoperfusion [40]. A 2-photon fluorescence microscopy study by Dorr et al. (2012) [12] in an Alzheimer's mouse model found increased penetrating arteriole tortuosity relative to controls. This increased tortuosity negatively affected network function, resulting in increased vascular transit times (ie. reduced network efficiency) and impaired reactivity to hypercapnia [12]. The tortuosity was attributed to the presence of plaques deposited near vessels [12].

In a study from Lund University in Sweden of Parkinson Disease in humans [41], enhanced concentration of angiogenesis biomarkers such as VEGF correlated with blood brain barrier leakage, white matter lesions, and movement difficulties. In mice administered MPTP (a neurotoxin that destroys dopaminergic neurons in the substantia nigra, similar to Parkinson in humans), microvessel networks in the substantia nigra contained regressing vessels, with endothelial cells clustered together [42]. Such changes are believed to reduce nutrient availability [42] and possibly expose brain tissue to toxic substances and inflammation [43].

A malfunctioning vessel network compromises neuronal stability through impaired delivery of oxygen and glucose [40]. Deficient vascular networks may contribute to cognitive decline through metabolic cascades involving synaptic loss, mitochondrial dysfunction, decreased energy molecule production, and oxidative stress [40]. Understanding the consequences of changes to vascular architecture is therefore critical to understanding disease progression.

1.2.2 Animal models of TBI

Traumatic brain injury (TBI) is damage to the brain by an external force, such as an object or pressure wave [44]. TBI severity is dependent on primary and secondary injury mechanisms. Primary injury is due to the initial impact. Secondary injury is the period following impact associated with inflammation, mitochondrial dysfunction, apoptosis, excitotoxicity, and oxidative stress [45].

During the primary impact, an external force deforms the tissue. This force compresses the cortex, causing swelling, hemorrhage, and ischemia. Damage to axons may occur via stretching and tearing [46]. Tissue deformation results in release of excitatory neurotransmitters that may be toxic in high concentrations. These neurotransmitters, such as glutamate and aspartate, lead to an influx of calcium into neurons, inducing apoptosis at high concentrations and activating enzymes which degrade proteins, lipids, and nucleic acids [46]. Excitotoxicity expands the initial lesion at the site of impact into the surrounding tissue [47]. While neurotransmitters are normally absorbed by astrocytes following release into the synapse, subsequent to injury, there is a decrease in the astrocytic glutamate transporter. This causes extracellular glutamate to remain in the synapse and further contribute to excitotoxicity [47].

In humans, brain injuries are usually classified as focal or diffuse, or a combination of both [48]. Focal trauma is visible with imaging techniques such as CT or MRI and occurs in severe and moderately head-injured populations [49]. Focal injuries may damage the vasculature and can cause bleeding within the brain (intracerebral hematoma), at the brain surface (subdural hematoma or subarachnoid hemorrhage), or within grey matter (cerebral contusion) [49]. Diffuse brain injuries are not localized to a single brain region. The most common diffuse injury is diffuse axonal injury (DAI), with lesions in cortex and white matter tracts. DAI is initiated by shearing forces due to rapid head rotation and acceleration [48, 50]. It leads to axonal swelling and impaired axonal transport, with minimal signs of focal vascular damage [51]. Axons are susceptible to shearing forces due to their organized structure within white matter tracts and viscoelastic properties [52].

Due to differences in size and shape of brains between rodents and humans, animal TBI models do not exactly replicate the human condition. Nevertheless, models reproduce features of trauma such as contusion, blast, and rotational forces causing axonal injury. Examples of widely used models include blast injury, fluid percussion injury (FPI), weight-drop, and controlled cortical impact (CCI). A brief description of these models follows below.

Blast injuries in humans most often occur during military conflict [53]. Blast animal models do not require craniotomy. The animal is placed in a chamber where shockwaves transmit forces to the brain [54]. In rodents, pathological changes induced by these shockwaves include DAI, astrocytic apoptosis, and vasospasm (arterial contraction causing vasoconstriction and reduced blood flow) [54, 55, 56, 57].

Fluid percussion injury (FPI) is the most commonly used pre-clinical TBI model and was initially applied to rabbits in 1965 [52, 58]. The dura and cortical surface are exposed via craniotomy. A pendulum strikes a piston that drives a saline-filled reservoir. This transmits a force through the reservoir, causing saline to be ejected and compress the cortical surface. The fluid moves into the epidural space concentrically from the point of contact [52]. The force with which the fluid bolus strikes the tissue is controlled by adjusting the height of the pendulum. Using a silicon vascular perfusion methodology and light microscopy, Park et al. (2009) [21] demonstrated in rats that the injured cortex undergoes a reduction in vessel density, with a 13 % decrease in capillary diameter in the injury core 24-hours post-injury. The reduction in density extends beyond the injury core, occurring up to 4 mm rostral and caudal from the injury epicenter [21]. FPI reproduces features of human TBI such as cortical contusions, damage to subcortical regions such as the hippocampus, and cognitive impairments such as memory and movement difficulties [46].

There are disadvantages to FPI. Pulse pressure is not a direct measurement of impact force to tissue, and it is difficult to compare pre-clinical and clinical injury severity. Once the fluid strikes the brain, brain geometry will affect fluid flow, rendering biomechanical analysis of the injury challenging [52]. FPI shows aspects of DAI similar to that in humans, demonstrating in rats accumulation of β-amyloid precursor protein in white matter and upregulation of tumor necrosis factor α, a cell signaling protein involved in inflammation [59]. In humans, however, rotational motion generates the shear forces that contribute to axonal injury, possibly due to the bulk modulus being five to six times larger than the shear modulus in human brain tissue [60]. This has been confirmed in animal models, with significant axonal injury in monkeys generated by lateral head motion [61]. Rotational motion is minimal in FPI.

Unlike FPI where only craniotomy position or size and pulse pressure (pendulum height) may be adjusted, there are several variants of the weight drop model. An early (1981) device in rats involved dropping a weight through a cylindrical tube onto cortex exposed via craniotomy [62]. Injury severity is adjusted by changing the diameter, height, and mass of the weight. Hemorrhages occur in the white matter directly underneath contused cortex. A tissue cavity develops by 24 hours, which expands over two weeks and is lined with macrophages [62].

In contrast to open-skull models, closed skull impacts display minimal tissue cavitation or swelling [63]. Closed-skull models show axonal injury similar to that observed in humans, such as swollen axons in white matter regions. Results vary between laboratories, despite usage of similar injury parameters. This variability is possibly due to an inability to precisely control impact parameters and biomechanical forces [46, 64]. Skull deformation and thickness are also contributing factors to susceptibility to TBI [65], with increased skull thickness reducing impact force on underlying cortical tissue in mice [66]. Since skull thickness and morphology vary across mouse strains and regions [67], differences in strain, age, sex, and impact location across studies may also contribute to variability.

CCI employs a metal rod to compress the cortex following craniotomy. Injury severity is adjusted through selection of impactor tip size, tip velocity, tissue deformation depth, and impactor dwell time. Similar parameters can also be controlled with the weight drop model, such as weight size and velocity (ie. through controlling the height of drop). Tissue deformation depth is difficult to regulate with weight drop. There is no risk of rebound injury with CCI. This is an advantage over free-falling weights since rebound injury from the weight can contribute to lack of reproducibility [52, 68]. In CCI, the head is restrained in a stereotaxic frame, whereas with weight drop models the head may or may not be restrained. Nevertheless, there is still room for brain movement following CCI, although tissue injury is greatest in the impact core [69]. Similar to FPI, CCI induces hemorrhage via direct tissue deformation, though neither model has a rotational injury component.

CCI induces morphological and cerebrovascular injury responses such as edema, elevated intracranial pressure, and decreased CBF [70]. Severe injuries result in significant hemorrhage [71] and loss of cortical tissue [72]. In the contusion core, there is blood-brain barrier leakage, astrocyte and microglia reactivity, neuron degeneration, and axonal injury [73]. These may contribute to inflammation, edema leading to increased intracranial pressure, cognitive deficits, and formation of a tissue cavity.

CCI may be employed in closed-skull format as described by Adams et al. (2018) [74]. The mouse head is stabilized in a stereotaxic frame and the skin over the skull is peeled apart, exposing the skull. A craniotomy is not performed, and the rod impacts the skull. This model is suitable for studying repeated head trauma, which may lead to chronic traumatic encephalopathy, a neurodegenerative disease in humans. In mice exposed to three impacts, Adams et al. (2018) [74] demonstrated evidence of cerebrovascular dysfunction two weeks following the final impact, such as elongated arterial transit times and impaired reactivity. This vascular dysfunction was accompanied by reduced neuronal activation in peri-contusional tissue [74].

1.2.3 TBI as a vascular injury

Open skull models (weight drop with craniotomy, FPI, and CCI) produce severe vascular injuries due to the absence of skull protection. By 3-hours post-injury, open skull weight drop in rats collapses vessels in the contusion core, causes intra- and extra-vascular clotting in capillaries that reduce blood flow, and induces capillary wall thinning with loss of surrounding tissue [75]. At the lightest level of injury, damage to the vasculature extends beyond the cortical contusion area into subcortical white matter. For the most severe injuries, vascular damage extends across the midline into the contralateral hemisphere [75]. Cortical contusion at the acute injury stage (3-hours) induced via CCI in rats enlarges pial vessels and increases their tortuosity [71].

Tortuous vessels are associated with mechanical factors such as connective tissue degradation, high blood pressure, reduced vessel tension, and vessel wall weakening [76]. Penetrating vessels display regions of swelling and constrictions through the cortical depth [71].

Vessel diameters are enlarged at 1-day post-injury as revealed with ex vivo X-ray micro-CT in rats following fluid percussion [77]. Vasodilation has been reported in vivo in human TBI [78] and in pial arterioles in cats at least 1-hour post-injury [79]. Dilation is sometimes attributed to shrinkage of larger diameter vessels due to extravascular blood products [80] and compensatory diameter increases by small arterioles to promote tissue perfusion [81]. An alternative explanation for enlarged diameters is enlargement of the perivascular space post-injury. This is possibly due to torn or swollen astrocyte processes, sheared cellular membranes, and fluid leakage into tissues [75]. The dilation of the perivascular space occurs concurrently with dilation of capillaries and venules in humans [75, 82, 83].

While vasodilation could increase flow to injured tissue in some cases, the resulting increased blood volume may contribute to elevated intracranial pressure (ICP) following TBI [84]. Elevated ICP in humans is associated with impaired autoregulation, contributing to poor outcomes in patients due to presence of ischemia/hypoxia [85].

Numerous rodent studies indicate reductions in cortical vessel density in open-skull models following trauma. These density decreases persist for several days: CCI in mice and rats 1 – 3 days post-injury [86, 87, 88]; FPI in rats 1 - 7 days [21, 89, 90]; and 1 – 2 weeks following stab wounds in rat brains [89]. Closed-skull injuries induce fewer loss of vessels, and in some situations, possibly no loss of vessels. For example, in the Marmarou weight drop (a weight is dropped over a metal helmet placed over the skull) vessel density is increased after two days with no reported loss of vasculature [91].

Damage still occurs to the vasculature in closed-skull models. For example, Stein et al. (2002) [92] demonstrated in a pig head rotation acceleration injury that intravascular coagulation occurred in small arterioles and venules throughout the brain. In a mouse rotational trauma model developed by Tagge et al. (2018) [93], capillaries are tortuous and compressed by swollen astrocytic feet at 2-weeks. At 24 hours post-injury, there is focal blood-brain-barrier leakage in the region of skull directly impacted [93].

Reduction in density is attributable to different factors. In the contusion core following FPI, lack of endothelial cell staining is coincident with infiltration of the region by macrophages. This indicates possible destruction of microvessels by the macrophages [89]. In peri-contusional and remote sites where macrophage presence is reduced, possibly vessel compression due to edema contributes to diminished ability to detect vessels [89, 94].

In addition to vascular structural alterations, functional deficits are present. In humans, autoregulation (maintenance of CBF over a range of pressures) is impaired. This could be due to arteries losing their myogenic response (ability to constrict) due to mitochondrial production of the vasodilator H_2O_2 in smooth muscle cells [95]. Loss of tone may also be caused by build-up of lactic acid [96] due to oxygen-limited glycolysis [97]. Lactic acid increases tissue CO_2 and prolongs vasodilation, limiting the extent to which vessels may further expand [79]. Free radical activation may also injure endothelial and smooth muscle cells necessary for diameter adjustments [98]. In addition, impairment of cerebrovascular autoregulation may be related to reduced autonomic drive, with heart rate variability (a metric of autonomic nervous system health) predicting impaired autoregulation following TBI [99].

Additional factors contribute to diminished CBF. Subarachnoid hemorrhage and edema increase intracranial pressure by distorting tissue and compressing vasculature [100]. This ‘strangling’ of blood vessels contributes to ischemia, a state of significantly reduced CBF.

To counteract reduced CBF, the vessel network undergoes angiogenesis and remodeling. In a rat model of FPI, Park et al. (2009) [21] showed that vessel recovery is dependent on injury severity, with density failing to recover by 2-weeks in the case of severe injury. Since Park et al. [21] measured density via vascular perfusion, possibly some vessels were constricted or collapsed, preventing their detection [101].

Despite categorization as a focal injury, Obenaus et al. (2017) [86] used a fluorescence perfusion technique in combination with widefield fluorescence microscopy to demonstrate that CCI induces loss of vasculature in rats in ipsilateral and contralateral cortices [86]. This vasculature regrows within two weeks [102], similar to the FPI study by Park et al. (2009) [21]. While it is difficult to determine precisely when remodeling begins, Morgan et al. (2007) [91] detected pre-mature capillaries in cortex two days following an impact-acceleration (Marmarou model) injury in mice [102]. In a rat cerebral focal contusion injury, VEGF mRNA expression in the contusion core peaks from 4 – 6 days post-injury and is reduced to baseline levels by 16 days [103]. This is in agreement with recovery of vessel density in a time frame of 1 – 2 weeks [21, 22, 87, 102].

Despite vascular regrowth, studies indicate that remodeled vasculature may differ structurally from animals that did not undergo injury. In the Park et al. (2009) study [21], rats subject to severe FPI display an increased number of enlarged or tortuous vessels at 2-weeks post-injury [102]. A study from that lab found abnormal vasculature persists 1-month post-injury, such as a 20 % shrinkage in capillary diameter [104]. In a rat blast injury model, intraventricular hemorrhage is present within a focal lesion 6 – 10 months following blast exposure, with tortuous vessels at the margin of the lesion [105]. Vascular abnormalities, such as disruption of the tunica media and regions of vacuolation, may extend beyond the injury margins into tissue with no glial or neuronal pathology [105]. These changes are proposed by Salehi et al. (2017) [102] to contribute to hypoperfusion and hemorrhage. In addition to vascular damage, changes in vessel wall associated cells may contribute to hypoperfusion. Capillaries not surrounded by pericytes may display abnormal properties such as leakage, dilation, hemorrhage, and reduced flow [106, 107, 108]. In TBI, pericytes migrate away from the vessel wall [109] and are often detached from vessels 5-days post-CCI injury [110]. This would contribute to low blood flow and impaired reactivity.

In CCI, the network architecture is significantly altered. Vessels radiate outwards from the central injury site in the cortex (see Figure 1.3) [87]. Similar findings are reported in a focal stroke model in mice at 6-weeks post-injury as visualized with 2-photon fluorescence microscopy [111]. Since formation of these vessels correlated temporally with the formation of scar tissue and a ‘dimple’ in the cortex, mechanical forces are possibly involved in the formation of the radial vasculature [111]. Radial vessels have been observed in skin injuries in mice, demonstrating this phenomenon is not restricted to the brain [112]. These radial vessels extended from the outer margins of the injury, where vessels of large diameters circled around the margin [112].

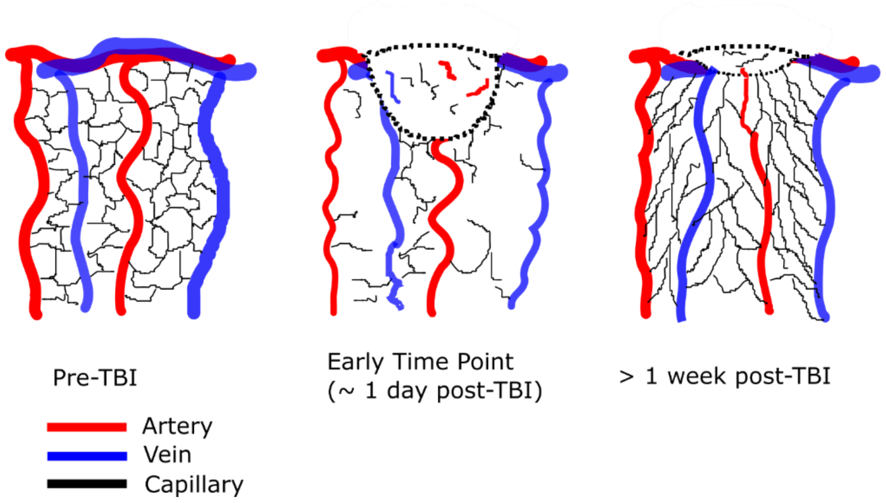

Figure 1.3. Evolution of vascular architecture following focal cortical injury*.* Prior to TBI, the capillary network possesses a net-like architecture with capillaries randomly oriented with respect to the cortical surface. Following injury, there is a reduction in vessel density both in the impact core (see dotted lines) and surrounding tissue. Over time, vessels regrow, and impact core size is reduced. The newly formed microvessel radially extending outward from the injury core.

1.3 Imaging Microvascular Structure and Blood Flow

This section describes imaging techniques for analysis of microvessel structure and blood flow. The techniques described are applied in Chapters 2 and 3: Two-photon fluorescence microscopy and Serial Two-Photon Tomography, and Arterial Spin Labeling (ASL) MRI for quantification of tissue perfusion.

1.3.1 3D microscopy for visualization of vascular structure

Vascular analysis traditionally relies on analysis of histological sections. Tissue is sliced into thin sections, with vessels labelled via perfusion of the vasculature with a dye prior to animal sacrifice, or section staining. Quantitative parameters extracted by this type of analysis may include diameter, density, surface area, volume, and length [113]. Histology does not capture other metrics that contribute to cerebral blood flow (CBF), defined as the volume of arterial blood (in mL) delivered to the capillary bed per 100 g of brain tissue per minute [114]. For example, vessel branching diameter ratios influence CBF and differ between healthy and diseased organs but are not captured by 2D imaging [115].

3D imaging provides a more accurate model of the vessel network. Nonetheless, commonly utilized 3D techniques have drawbacks. X-ray micro-computed tomography images entire mouse brains, but resolution of bench top systems (20 µm) prevents capillary visualization [20]. In vivo confocal microscopy, though capable of visualizing capillaries, only images 100 - 200 µm into cortex due to light scattering [116].

An imaging modality suited for visualizing the microvasculature is 2-Photon Fluorescence Microscopy (2PFM). In 2-photon fluorescence, two photons are absorbed in the same quantum event. Each photon has approximately half the energy required to transition the fluorophore to a higher energy level. Near infrared light (700 – 1000 nm), with deeper penetration into tissue, is employed [116]. This deeper penetration is due to decreased scattering at longer wavelengths and reduced tissue absorption. Absorption is strongest in the focal region, with minimal fluorescent signal generated from out of focus planes. 2-photon excitation eliminates the need for a pinhole to block scattered light as per confocal microscopy. This allows for increased detected fluorescence and enhanced imaging depth.

Imaging depth in vivo is limited to 1 mm in cortex due to scattering [117]. Light scattering may be minimized, and imaging depth increased, by rendering tissue transparent via ‘optical clearing’. In optical clearing, water in the tissues is replaced with a substance having a high refractive index similar to tissue membranes. Variability of refractive index in tissue is decreased, enhancing transparency.

Organic clearing materials reduce fluorescent protein signal due to dehydration prior to clearing [118]. This could affect cell visualization in mice expressing fluorescent protein. In addition, the high refractive index of clearing materials also causes spherical aberrations when imaging is performed with a water-immersion objective.

Several techniques exist for imaging large regions of mouse brain tissue in 3D without optical clearing. These techniques typically slice, cut, or evaporate tissue to increase imaging depth. Examples include micro-optical sectioning tomography (light microscope with microtome) [119, 120], serial block face scanning electron microscopy (scanning electron microscope with diamond knife for cutting) [121], and All-Optical Histology [122]. All-Optical Histology uses laser pulses to cut and ablate tissue. Following tissue cutting, a 2-photon fluorescence microscope acquires a 3D image of a block of tissue, typically about 200 µm thick [122]. If the thickness of the cut is less than the imaging depth, images through the tissue depth overlap in space and may be stitched together. Serial Two-Photon Tomography (STPT) [1] operates on a similar principle to All-Optical Histology, with a vibratome for sectioning as an alternative to lasers.

1.3.2 ASL MRI for quantification of CBF

ASL MRI has detected 85 % decreases in CBF in the contused cortical region 3 hours after CCI in rats [123], and perfusion increases greater than 100 mL/100 g/min in response to increased arterial pCO_2 in healthy rats [2]. It is useful for studying blood flow regulatory mechanisms [124] and quantifying CBF acutely and months following TBI [22, 30].

The initial step of the imaging procedure is inversion of the magnetization of hydrogen spins in arterial vessels such as the common carotids leading to the brain. A time delay (post-label delay) prior to imaging is allowed for the labelled blood to perfuse the tissue of interest. This post-label delay minimizes signal from large arteries that could lead to quantification errors and ensures that labeled blood has enough time to reach all imaging voxels. The delay should be greater than the arterial transit time. Delays of 500 ms [125] have therefore been used, since transit time values in mice are under 300 ms [126]. The observed magnetization with MRI is a mix of labelled water magnetization and static tissue water magnetization. This image is referred to as the tag, or label image. Non-label (control) images are similarly acquired without labeling. Since no labeling is performed, the image only contains a static tissue magnetization component. An ASL CBF image is produced by subtracting the label image from the control image. This subtraction image removes signal from background water spins; thus, the signal measured is associated with the labeled blood delivered to the capillaries.

To accurately model CBF from the ASL difference image, the ‘single-compartment’ model is commonly used [127]. In this model, labeled blood enters a tissue voxel via an artery, and is cleared via venous outflow or longitudinal relaxation. It is assumed that due to rapid exchange of water across the capillary walls, when the labeled blood leaves the voxel its magnetization equals the magnetization of the whole voxel, with a weight given by the equilibrium ratio of water in the brain in comparison with blood [127]. Two-compartment models account for restricted vessel wall permeability, where labeled water remains in the vessel for a period prior to entering the extravascular space [114, 127]. In mice, it has been demonstrated that the single- and two-compartment models produce CBF estimates that differ by less than 10 % [3].

Two methods for inverting the magnetization of the hydrogen spins are Pulsed ASL (PASL) and Continuous ASL (CASL). In PASL, magnetization is inverted in a thick slab adjacent to the slice of interest with a brief radio-frequency (RF) pulse. In CASL, inversion of the arterial blood occurs through application of a continuous RF pulse distant and upstream of the imaging volume. PASL deposits less power into tissue than CASL. This is advantageous for human studies. CASL is used more frequently in small animal research for higher SNR.

1.4 Ultrasound and Wave Reflection Theory

Microscopy techniques for visualization or quantification of microvascular structure are often not applicable to humans as they require sacrifice of the subject or invasive surgeries. Ultrasound imaging provides a quick and non-invasive method with the potential for detecting cerebrovascular abnormalities in TBI.

This section is divided into three parts: (1.4.1) *Detection of cerebrovascular abnormalities with Doppler ultrasound;* (1.4.2) *Ultrasound wave reflection theory;* (1.4.3) *Ultrasound in TBI research*. Part (A) describes use of Doppler ultrasound in detecting vascular dysfunction. Part (B) introduces a technique based on wave reflection theory through a combination of Doppler ultrasound with M-mode imaging. This technique detects changes to vascular architecture and resistance. It overcomes limitations in Doppler ultrasound, as is described below. Part (C) is a review of ultrasound studies in TBI.

1.4.1 Detection of cerebrovascular abnormalities with Doppler ultrasound

Doppler ultrasound calculates red blood cell (RBC) velocity within a vessel [128]. In Doppler ultrasound, a series of pulses (pulsed Doppler) or a wave (continuous wave Doppler) is emitted from the transducer (ultrasound probe). In stationary tissue, with no RBC movement, the frequency of the transmitted wave is identical to that of the wave reflected from the tissue. For reflection from moving RBCs for continuous wave Doppler, there is a shift in frequency of the received signal. This is termed the 'Doppler shift'. If the angle between the vessel and insonating beam is known, the RBC velocity can be calculated [129]. Despite its name, pulsed Doppler does not rely on the Doppler Effect. Rather, it estimates the velocity component in the direction of the beam from changes in the signal caused by movement of the scatterer between two transmitted pulses [130]. It can be demonstrated that for a transmitted pulse scattered by a single moving scatterer, the sampled received signal from the scatterer (assuming each received signal is sampled with the same delay from transmission) has a frequency scaled in proportion to its speed relative to the transmitted frequency [130]. In the case of numerous scatterers with a distribution of velocities, the received sampled signal will contain a distribution of frequencies. Thus, decomposing the received signal into its spectrum of frequency components will yield the distribution of velocities within the sample. Pulsed Doppler ultrasound achieves depth discrimination by adjusting the time window that is analyzed following the pulse. However, pulsed Doppler imaging is subject to aliasing, particularly at deeper depths with a larger pulse repetition interval. This limits the maximum detectable velocity. In contrast, continuous wave Doppler is not subject to aliasing, but lacks depth discrimination.

Typical parameters calculated from a Doppler scan are pulsatility index (PI), mean velocity over a cardiac cycle, and systolic and diastolic velocities. PI is defined as the difference between the maximum systolic velocity and minimum diastolic velocity, normalized over the mean velocity over the cardiac cycle. PI or arterial blood velocity and flow are used as indicators of abnormal/diseased tissue or vasculature. For example, Cahill et al. (2017) [125] found elevated common carotid flow in Sickle Cell mice relative to controls. This was interpreted as an adaptive response to tissue hypoxia in Sickle Cell disease [125]. Stenosis (narrowing of arteries) in humans may be detected by increased RBC velocity through the narrowed artery [131], with velocity sometimes greater by 30 % [132].

Doppler-derived PI is often interpreted as an indicator of downstream vascular resistance [133]. Low resistance vessel networks possess higher diastolic flow and rounded systolic peaks, yielding small PI values. Conversely, high resistance networks have a ‘peaked’ systolic velocity with lower diastolic velocity, yielding a larger PI [133].

PI as a potential indicator of vessel network resistance has been shown in multiple studies. In ultrasound imaging studies of umbilical arteries in humans, there is a strong negative relationship between PI and the number of small arterioles in tertiary stem villi [134]. This suggests that loss of downstream vessels contributes to increased resistance. In small vessel disease in humans, PI measured by Doppler in the middle cerebral artery (MCA) correlates with MRI manifestations of small vessel disease such as white matter hyperintensity and lacunar disease (atherosclerosis of penetrating vessels) [133].

Despite these results, PI is not always a reliable indicator of vascular resistance. Michel and Zernikow (1998) [135] theoretically demonstrated that PI depends on the ratio of the cerebrovascular impedance at zero frequency to that at the frequency of the heart rate. This ratio closely relates to the critical closing pressure (CCP), which is the arterial blood pressure at which CBF approaches 0 [136]. Since CCP depends on mean arterial blood pressure (increases with blood pressure due to increases in wall tension [136]), arterial partial pressure of CO_2 (decreases under hypercapnia due to vasodilation caused by CO_2) and heart rate (increases with heart rate [137]), PI depends on numerous factors beyond resistance [135].

The dependence of PI on multiple parameters has been shown experimentally. A study in rabbits by Czosnyka et al. (1996) [138] found an increased PI with diminished network resistance in transcranial Doppler imaging of the basilar artery during hemorrhagic hypotension [138]. The authors interpreted this phenomenon as hemorrhage reducing cerebral perfusion pressure (CPP). Reduced CPP causes vasodilation and decreased network resistance. Decreasing CPP also relaxes arterial smooth muscle cells and increases arterial compliance. This increase in compliance counteracts reduced resistance, causing an overall increase in PI [138].

1.4.2 Ultrasound wave reflection theory

As seen with the above experiment in rabbits, PI or blood velocity does not necessarily provide an accurate calculation of network resistance. This problem may be overcome through application of ‘wave reflection theory’, detailed below.

Wave reflection theory is described in Rahman (2016) [139] and Hartley et al. (2011) [140]. M-mode and Doppler data are acquired for measurement of artery diameter and blood flow velocity respectively. During systole, the heart generates pressure, contracts, and ejects blood. Cardiac contraction (systole) and relaxation (diastole) creates a pressure and flow pulse wave that propagates through the arterial system. This wave is termed the ‘forward traveling wave’ [140]. At bifurcations, arteries normally branch into smaller vessels. These smaller vessels may contain different wall thicknesses, compliance, amount of smooth muscle, etc. These differences in characteristic (local) impedances between a vessel and its smaller branches cause reflection of the forward wave back towards the heart, or the part of the vessel prior to the bifurcation. At any site within a vascular network, the measured pressure is the sum of the forward and reflected (backward) pressure waves; the measured flow is the sum of the forward and reflected (backward) flow waves (see Figure 1.4 below). Reflected waves may be produced as far downstream as the terminal capillary bed [141]. Consequently, the overall reflected wave measured in the input vessel (ie. the vessel imaged with M-mode/Doppler ultrasound) is the sum of all reflections from the downstream vasculature. Measurement of properties of this wave, such as magnitude, provide information on the impedance of the downstream vessel network.

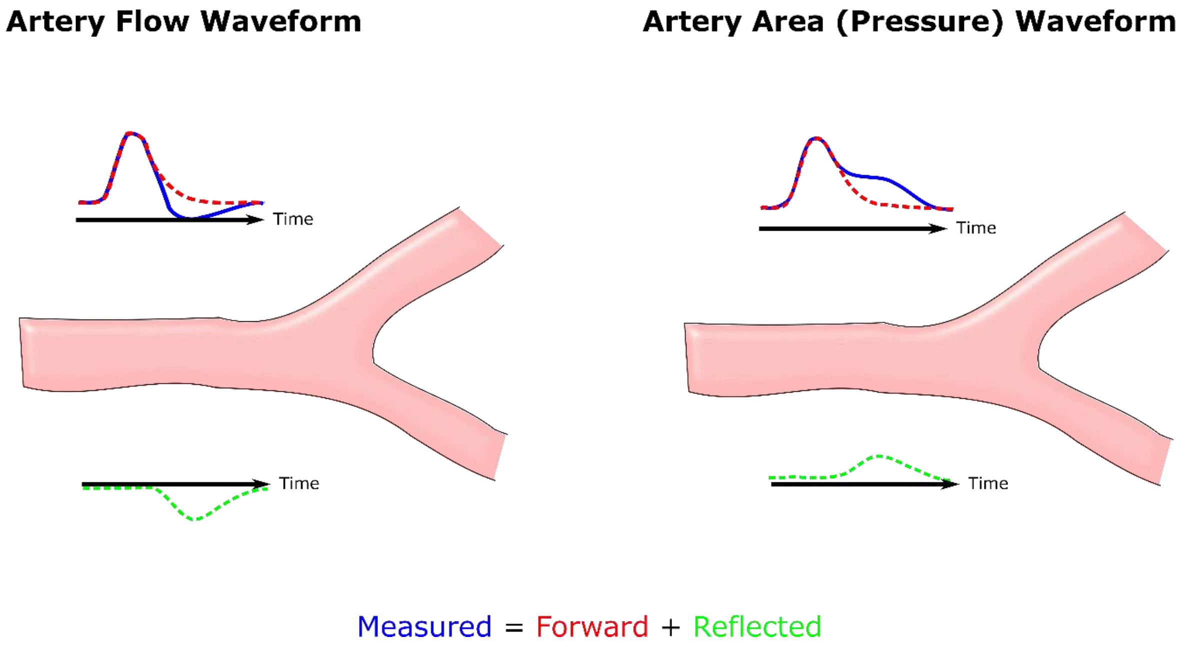

Figure 1.4. Reflected flow and pressure waveforms in an artery. The measured wave (blue, solid line) is a superposition of the forward (red, dotted line) and reflected (green, solid line) waves. Waves may be either area, which is proportional to pressure, or flow (velocity x area). If a vessel narrows (closed type termination), the reflected flow wave is inverted. This inversion is due to net flow required to be 0 at the boundary, since flow waves cannot pass through a closed boundary. Pressure (area), on the other hand, can vary at a closed boundary, thus the reflection may be upright. Consequently, the measured waveform is greater than the forward waveform where the reflected area wave is superimposed on the forward wave. The converse holds for superposition of forward and reflected flow waves.

The pressure or pulse wave travels along the imaged artery at a speed termed the pulse wave velocity (PWV). PWV depends on vessel stiffness, characterized by Young's modulus of elasticity [142]. Rather than measure elasticity directly, a flow-area curve over a cardiac cycle is calculated from the Doppler and M-mode waveforms. The ratio of the change in flow to change in area during early systole yields an estimate of PWV [139, 143]. Using this estimated PWV, and assuming the cross-sectional vessel area measured with M-mode is proportional to the pressure inside the vessel, it is possible to calculate the forward and reflected flow waveforms as described in Westerhof et al. (1972) [141]. This enables calculation of metrics such as the reflection coefficient, which is the ratio of the peak magnitude of the backward wave to that of the forward wave.

Higher reflection coefficients indicate larger downstream mismatches of vascular impedance and possibly abnormalities in the circulation. A recent ultrasound study by Cahill et al. (2019) [144] found that in a mouse model of fetal growth restriction, there was an increased (27 %) reflection coefficient in the umbilical artery at E17.5 compared to controls. This increase in reflection coefficient corresponded to a 36 % increase in the number of vessel segments as imaged by X-ray micro-CT. Since no difference in PI was detected, this suggests that the enhanced reflection provided information on vascular architecture not accessible with traditional ultrasound analysis.

The ultrasound technique used by Cahill et al. [144] above was originally developed by Macgowan et al. (2015) [4], who assessed wave reflection in the (left) common carotid artery of mice under rest and hypercapnic conditions. Mice in the hypercapnic state were found to have an increased reflection coefficient compared to those at rest, indicating the ability of the technique to detect changes in microvessel diameter in the brain. Using PWV, Macgowan et al. [4] also calculated input impedance modulus and phase. The decrease in phase under hypercapnia was interpreted as representing an increase in arterial compliance [145]. This finding illustrates the use of wave reflection analysis to assess multiple aspects of vascular structure [4].

Although Macgowan et al. [4] did not find PWV differences between rest and hypercapnia, PWV is a measure of arterial stiffness [146]. Carotid PWV increases with age (35 – 55) in humans [145], and correlates with the extent of atherosclerosis in hypertensive patients [147]. PWV is a potential marker of vascular disease or injury.

1.4.3 Ultrasound in TBI research

Most ultrasound imaging in human TBI is of the intracranial vasculature, such as the MCA [148, 149]. The MCA is interrogated since it is accessible with transcranial Doppler (TCD), and low flow within it is a risk factor for poor recovery [149].

Doppler ultrasound has highlighted vascular functional abnormalities in several clinical studies. Cerebrovascular reactivity to hypo- and hyper-capnia is reduced in sport-related concussion within 7-days from the initial injury [150, 151]. In severe head trauma, hyperemia (increased flow attributed to increased metabolism and circulating vasodilators) occurred on days 1 – 3, followed by reduced flow relative to the early days on days 4 – 8 attributed to vasospasm [152]. Both hyperemia and vasospasm are associated with a lower pulsatility index (PI) compared to the acute phase immediately following the injury [152], with vasospasm persisting up to 3 weeks post-injury [153]. Reduced PI may occur due to reduced downstream vessel resistance caused by vasodilation of small arterioles to compensate for large artery vasoconstriction [81].

While other studies contain similar findings of reduced PI in head trauma [154, 155], PI may also be increased, particularly in the acute phase [155, 156, 157]. This discrepancy is possibly attributed to the type of brain injury acquired. For example, vasospasm induced by subarachnoid hemorrhage will reduce pulsatility through compensatory vasodilation of small arterioles [81, 155], while increased intracranial pressure could increase pulsatility [157].

Ultrasound experiments in TBI animal models are limited. In a rotational TBI in 4-week-old piglets, common carotid artery diameter and flow were reduced 1-hour post-injury [148]. To our knowledge, few TBI studies in humans or animals other than the piglet model of injury [148] have been performed with ultrasound in the common carotid arteries. Carotid imaging is advantageous over MCA imaging since cerebrovascular changes observed in the MCA are not necessarily representative of global changes throughout the intracranial vasculature [148].

1.5 Structure and Organization of Thesis

Chapter 2, previously published in PLOS One [158], compares in vivo and ex vivo 2-photon fluorescence imaging of the cortical vasculature in mice. The analysis methodologies developed in Chapter 2, such as segmenting the vasculature in the presence of optical aberrations and anisotropic resolution, are relevant for Chapter 3.

Chapter 3 utilizes Serial Two-Photon Tomography [1], an ex vivo 2-photon fluorescence microscopy technique, for high-resolution microvascular imaging in a CCI mouse model. ASL MRI perfusion maps are acquired in the same mice, enabling correlation between 3D microvascular structure and function.

Chapter 4 applies ultrasound based on wave reflection theory to detect differences in wave reflection and vascular impedance in the mice from Chapter 3.

Chapter 5 summarizes and connects the previous chapters. The relevancy of the thesis for TBI is discussed. Future experiments and studies are proposed.

Chapter 2

3D Morphological Analysis of the Mouse Cerebral Vasculature: Comparison of In Vivo and Ex Vivo Methods

2.1 Foreword

This chapter was previously published in PLOS One [158]:

Steinman J, Koletar MM, Stefanovic B, Sled JG. 3D morphological analysis of the mouse cerebral vasculature: Comparison of in vivo and ex vivo methods. PLOS One 2017; 12(10): e0186676.

2.2 Introduction

The brain is highly sensitive to reductions in blood flow. Occlusions of arterioles cause microinfarcts, which may coalesce across the cortex if multiple arterioles are occluded [36]. Hypoperfusion in Alzheimer's disease is associated with white-matter lesion formation and microinfarcts [159]. Flow reductions co-localize with white matter vascular disease and correlate with cognitive function [160, 161]. Cerebrovascular architecture is one of the major determinants of cerebral blood flow (CBF), since the diameters and lengths of individual vessels, and their connections in 3D space, dictate vascular network resistance [162, 163]. Architectural changes, such as stiffening of cerebral arteries or increased vessel tortuosity, are seen in cognitive impairment, enlarged ventricles, and dementia [12, 164].

A variety of imaging techniques exist for visualizing the cerebral vasculature; however, few possess the resolution or tissue imaging depth to visualize arterioles, venules, and capillaries deep into cortex. Micro-computed tomography can image an entire mouse brain in 3D, but the resolution of bench top systems (20 µm) precludes capillary visualization [20]. In contrast, confocal microscopy possesses resolution on the order of 1 µm, but the depth of penetration into tissue is only 100–200 µm due to the high degree of scattering at the wavelengths utilized [116]. Two-photon fluorescence microscopy (2PFM), on the other hand, provides cellular resolution and greater depth penetration. In vivo 2PFM provides capillary-resolution images up to 800 µm below the cortical surface, a several-fold improvement over confocal microscopy [165]. It is valuable for imaging microvascular architecture since it possesses sufficient resolution for visualizing capillaries and allows imaging well below the brain surface. This paper contrasts in vivo 2PFM with an alternative 2-photon fluorescence imaging method based on ex vivo cleared tissue specimens.

Even though in vivo 2PFM provides improvement in resolution and/or imaging depth in comparison with other methods, it is unable to visualize the vasculature through the entire mouse cortex, as it exceeds 1.5 mm thickness in some cases [166]. To enhance depth penetration, ex vivo tissue clearing techniques may be combined with 2PFM. Optical clearing has been shown to enhance imaging of brain [167] and spinal cord tissue [168]. High refractive index materials similar to tissue membranes render tissue the most transparent and provide the deepest imaging. For example, SeeDB, a fructose-based clearing agent, enables an imaging depth up to 8 mm with 2PFM [169].

While optical clearing improves imaging depth, tissue dimensions may be changed by the clearing materials. This in turn may distort morphological measurements. If the refractive index of the clearing agent (and by extension the cleared tissue) differs from that of water (the typical immersion medium of the microscope objective), spherical aberrations will occur. These aberrations worsen with depth and are the most severe for the higher refractive index materials which result in optimal tissue clarity. To overcome these aberrations, oil-immersion objectives may be used, but these typically have a working distance less than 300 µm, defeating the purpose of optical clearing. Smaller vessels, whose dimensions are on the order of those of the Point Spread Function (PSF) of the imaging system, are proportionately more distorted relative to their diameters. This may result in an overestimation of their diameters and reduce the ability of computational algorithms to detect and segment these vessels.

The goal of this work is to contrast ex vivo and in vivo imaging, while highlighting the advantages and disadvantages of each. To achieve this goal, an ex vivo 2PFM methodology for mouse cortical vascular imaging is developed and presented. The methodology consists of the following components: (A) perfusing the vasculature with a fluorescent gel that solidifies inside the vasculature, rendering the vessels visible under a fluorescent microscope; (B) clearing the tissue via immersion in a high-concentration fructose solution; and (C) accurate calculation of vessel diameters via a novel segmentation algorithm that accounts for the spherically aberrated and spatially varying ex vivo PSF. This ex vivo technique is then used to contrast vascular networks imaged in vivo vs ex vivo. Mice are imaged with in vivo 2PFM; these imaged regions are then identified following tissue processing and imaged ex vivo. Identical vessels in both images are identified with advanced registration algorithms, enabling the comparison of the properties (signal, morphology) of corresponding vessels in vivo/ex vivo. This study assesses in vivo/ex vivo imaging beyond well-characterized metrics such as imaging depth, which is possible through the advanced registration and image analysis techniques utilized.

2.3 Materials and Methods

2.3.1 In vivo imaging

In vivo procedures were approved by the Animal Care Committee of the Sunnybrook Health Sciences Centre, under Animal Use Protocol 15–563. Four mice total (C57BL/6) were imaged on separate days, with both in vivo and ex vivo 2PFM. Mice were anaesthetized via isoflurane [5 % induction, 1.5 – 1.75 % maintenance in oxygen enriched medical air (30 % oxygen, balanced nitrogen)] as described in Dorr et al. [12]. The oxygen supplement was to compensate for the respiratory depression effect from general anesthesia. A stereotaxic frame with a bite bar and ear bars restrained the mice. Core body temperature was maintained at 37 ± 3^{o} C using a rectal probe and a feedback-controlled heating pad (TC-1000, CWE Inc.). Other physiological parameters were monitored by pulse oximetry (MouseOx Plus) for a target heart rate of approximately 500 beats per minute, respiration rate 60 – 80 breaths per minute, and oxygen saturation 98 ± 1 %. Since mice were not intubated (or maintained by mechanical ventilation), end expiratory carbon dioxide was not measured. Stereotaxic surgery was performed, the primary somatosensory cortex was demarcated, and a small (< 5 mm diameter) cranial window drilled in this area. This window was sealed with a 5 mm diameter coverslip (World Precision Instruments) glued to the skull.

2PFM was performed using a twin FV 1000 Multi Photon Excitation Microscope (Olympus Corp., Tokyo, Japan) with a 2 mm working distance water immersion microscope objective (25 x, 1.05 NA). An intraperitoneal (IP) injection of the fluorescent contrast agent SR101 (8 µL/g of body weight) dissolved in 0.1 M phosphate buffered saline (PBS) was administered [170]. Images were acquired at 0.994 µm lateral resolution and 1.5 µm axial step size. The excitation wavelength was 900 nm. The objective used for this high-resolution 3D imaging was replaced with a 5 x 0.1 NA objective to obtain a map of the pial vasculature on the cortical surface. This image possessed a 2.5 mm field of view, in comparison with the 0.5 mm field of view for the for the 1.05 NA objective and was obtained at 5 µm nominal lateral resolution with a 50 µm step size. This image was later used to identify the same imaging region ex vivo as in vivo.

Since the SR101 dye has a small molecular size, there is a possibility that it penetrates the glycocalyx, unlike the FITC albumin dye. If this were the case, in vivo diameters could be overestimated relative to ex vivo. To assess whether this had occurred, an additional mouse was imaged in vivo on the same 2PFM system. This mouse was simultaneously administered an IP SR101 injection as previously described, as well as a tail vein injection of a 2 MDa FITC dextran which is too large to pass into the glycocalyx. The signals from the red and green dyes were separated using 495 – 540 and 575 – 630 bandpass filters. Both dyes were excited at 900 nm, and imaging was performed with the 25 x objective, at 0.994 µm lateral resolution and 1.5 µm axial step size.

2.3.2 Ex vivo animal preparation and imaging

Following in vivo imaging, mice were removed from the stereotaxic frame, and anaesthetized a 2nd time with an IP injection of 100 µg ketamine per gram of body weight (Pfizer, Kirkland, QC, Canada) and 20 µg xylazine per gram of body weight (Bayer Inc., Toronto, ON, Canada). They were transferred to the fumehood, where an incision was made in the chest to allow for opening of the chest cavity, and a 24-gauge IV catheter (Becton Dickinson Infusion Therapy System Inc., UT, USA) was inserted into the left ventricle. A slit made in the right atrium permitted outflow of blood. Mice were perfused at a constant volume flow rate of 5 mL/min with 30 mL of heparinized (5U/mL) 0.1M PBS (Wisent Inc., St-Bruno, QC, Canada), 30 mL of 4 % paraformaldehyde (PFA) (Electron Microscopy Sciences, Hatfield, PA, USA), and 20 mL of a 2 % (w/v) gelatin solution (Sigma, St. Louis, MO, USA) combined with 1 % (w/v) FITC-conjugated albumin (FITC-albumin; Sigma) [6]. Prior to perfusion, the gelatin solution was filtered through 0.8 µm pore size syringe filter.

Following perfusion, mice were decapitated, and the skin remove from the skull. The brains (while inside the skull) were immersion-fixed for 24 hours in 20 mL of 4 % PFA. The coverslip was removed, and the tissue was cleared in graded solutions at 12 hours each of 20 %, 40 %, 60 %, 80 %, and then 100 % SeeDB (80.2 % wt/wt fructose in distilled water with 0.5 % α-thioglycerol) [169] while inside the skull. Brains were removed from the skull following clearing and were glued to the inside of a glass container. This container was filled with SeeDB and sealed with a No. 1 glass coverslip. A drop of water dripped onto the coverslip surface enabled the 1.05 NA water-immersion objective lens to be dipped into the water-drop. Images were obtained at 800 nm excitation and encompassed the identical region that was imaged in vivo.

Lateral pixel size was the same (0.994 µm) as that in vivo, while the apparent axial step size was 1.34 µm. However, an apparent step size of 1.34 µm corresponds to an actual step size of 1.5 µm (as per the in vivo image), since the refractive index mismatch between the clearing agent and water causes the apparent axial step to be scaled by a factor of 1.12 (scaling factor = n_{agent}/n_{water} = 1.49/1.33 = 1.12). Multiple images of overlapping volumes were acquired to maximize the likelihood that vessels imaged in vivo were captured ex vivo. Image stitching was performed using the algorithm described in Emmenlauer et al. [171] to produce a single large field-of-view image. Figures 2.1A and 2.1B are an example of a corresponding in vivo/ex vivo image pair.

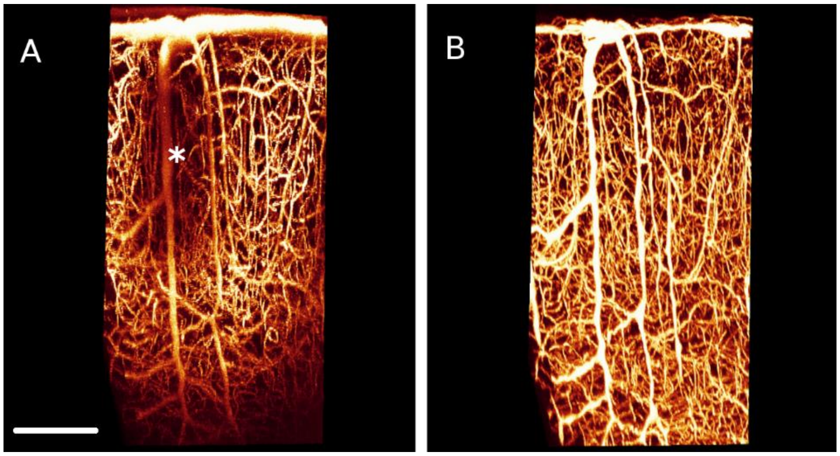

Figure 2.1. Maximum Intensity Projections (MIPs) of corresponding in vivo-ex vivo datasets from a single mouse. (A) In vivo MIP. (B) Ex vivo MIP. Both A and B display the vasculature with cortical depth. Unlike in the ex vivo image, where a relatively constant signal is maintained through the cortical depth, the signal in vivo is relatively weak at about 400 – 500 µm below the cortical surface. In addition, vessels in vivo beneath the pial vasculature (large diameter vessels at the cortical surface) are detected at a weaker signal compared to those that are not underneath these vessels (see the dark patch demarcated by the * in panel A). Scale bar = 0.2 mm.

2.3.3 Image analysis

In comparing vascular architecture in vivo and ex vivo, the vessels in both images were automatically segmented with an in-house developed vessel tracking software [115] (see Vessel tracking). No manual correction of the segmented data was required, and all post-processing was performed automatically. Registration and identification of common vessels in both images enabled a 1-to-1 correspondence to be made between in vivo/ex vivo vessels for the comparison analysis (elaborated upon in below).

Vessel tracking: Vessel tracking (the algorithm used here for segmenting the vasculature) differs from traditional binarization segmentation techniques since it traces the centerlines of vessels that are approximated as discrete medial atoms [172], as opposed to binarizing and iteratively thinning the binarized image. At discrete points along the vessel (vertices), the centerline is sampled through optimization of the radius and position in 3D space of an image operator. This operator is defined by 8 spokes extending from the vessel centre (ie. medial atom) to its boundary. This procedure enables identification of the centerline location, local tangent vector to the vessel, and the vessel radius. The metric that is optimized is the sum of the intensity gradients measured for each spoke. A low gradient calculated at the tip of a particular spoke indicates a potential branch point.

Each xy-plane in the in vivo/ex vivo images was convolved with a 2D Gaussian blurring kernel with a full-width-half-maximum (FWHM) of 1.5 µm. The image was resampled to an isotropic voxel size of 1.5 x 1.5 x 1.5 μm^3, after which a non-local means denoising filter was applied [173].

On the order of 400 000 seeds (digital markers)/mm^3 were automatically placed inside the vessels of an image to initiate tracking. Despite thousands of seeds being created, the tracking time was increased by a negligible amount since seeds in previously tracked vessels were ignored by the algorithm. It is necessary to include multiple seeds throughout an image (instead of initiating tracking with a single seed inside a single vessel) as this ensures all vessels are segmented, including those partially contained within the field of view that may appear disconnected from the rest of the network. Seed locations were determined separately for each image by manually selecting a signal threshold to separate vessels in the foreground (which possess a large signal) from the weak tissue background. Voxels that were a local signal intensity maximum with respect to their six nearest neighbours were chosen as seed locations. Because the centerline of a vessel often corresponds to a local maximum in signal intensity, this algorithm ensures that a marker is placed close to the center of the vessel.

The anisotropic PSF of the 2PFM data was approximated as a 3D Gaussian distribution, with different FWHM values within the xy-plane and through the z-axis. In tracing vessels, the marginal distribution of the PSF in the plane perpendicular to the vessel axis was computed. This was convolved with the proposed circular cross-section of the vessel, approximated as a 2D Gaussian distribution. These convolved distributions (marginal distribution of the PSF and circular cross section) defined an ellipse in the given plane. The procedure outlined above for the circular image operator described in Rennie et al. [115], involving the computation of the gradient at the 8-spoke tips, was repeated to calculate the vessel radius, tangent vector, and centerline. As shown in Figure 2.2, the refractive index mismatch between fructose and water causes the axial width of the PSF to increase linearly with tissue depth ex vivo. The PSF dimensions were assumed to be constant when tracking the in vivo data. As per the straight line fit in Figure 2.2, the axial PSF was specified in vessel tracking to increase in a linear manner from 3.4 µm at the surface of the tissue to 7.5 µm at 1 mm depth. The axial FWHM for the in vivo image was maintained constant through the cortical depth at 3.4 µm. The FWHM along the x- and y-axes perpendicular to the optical axis was assumed to be unchanged with depth for both image types (in vivo and ex vivo).

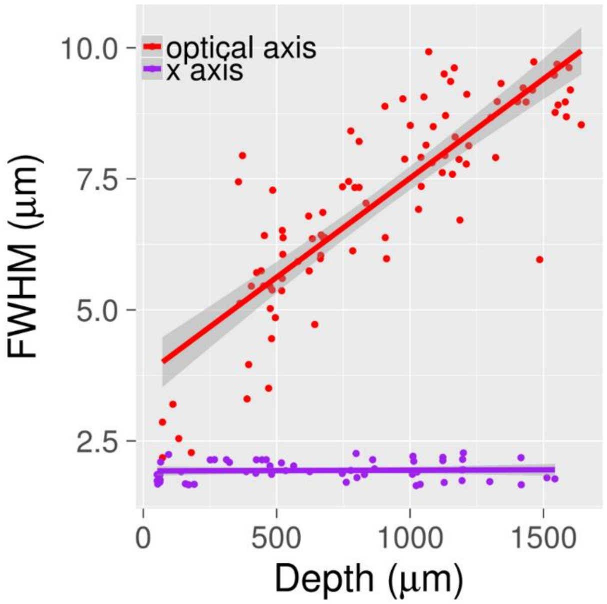

Figure 2.2. FWHM of signal along optical axis and x-axis versus depth for beads embedded in agar. The beads were 0.5 µm diameter yellow-green fluorescent beads (excitation peak 505 nm; emission peak 515 nm) and were embedded in fructose-cleared 1 % low melting point agar. Imaging was performed using 2PFM at an excitation wavelength of 800 nm. The FWHM was calculated by fitting a Gaussian to the signal profile along either the optical or x-axis for these beads. Prior to fitting the Gaussian, the image of the beads was blurred by a Gaussian with FWHM 1.5 µm, as per the vascular images on which vessel tracking was performed. Since the slope of the x-axis was not statistically different from 0 ($p = 0.8136$), only the PSF along the optical axis was assumed to change with depth when performing vessel tracking. The ribbons surrounding the straight lines represent the 95 % confidence interval.

During tracking, fluctuating voxel intensities caused by noise on the vessel surface may be transformed into short free-ends ('hairs') emanating from the centerlines of actual vessels. A hair was defined as a free-end vessel segment with length not exceeding the radius of the vessel to which it is connected by more than an empirically selected amount of 8 µm. All such vessels were removed.

Image registration: Identification of common landmarks corresponding to pairs of identical vessels, such as vascular branch points, enabled in vivo-ex vivo images to be registered to one another via a thin plate splines algorithm (TPS) [174]. This same transformation was applied to the ex vivo trees generated via tracking the ex vivo data. This aligned the ex vivo trees with the in vivo data in in vivo image space, and the vessel diameters of these trees were recalculated in in vivo space as described in the section Vessel tracking. The diameter calculation was performed using the same algorithm described above. Since the calculations were in in vivo space, the PSF width was assumed to be constant with depth. This procedure enabled each vertex in the original ex vivo tracing to be correlated with the same vertex in in vivo space, thereby allowing a direct comparison between properties of the same vessel in vivo-ex vivo. To compare the diameters/signal of corresponding vessels it is also possible to apply the inverse of the transformation just described to the in vivo tree and recalculate the diameters in ex vivo space. The option was chosen to recalculate diameters in in vivo space (ie. apply the transformation to the ex vivo tree) due to the strong signal maintained through the cortical depth in the ex viv*o* images, and the lack of shadowing artifacts ex vivo (discussed in further detail in the Results and Discussion sections).

To evaluate the success of the gelatin perfusion on a vessel-by-vessel basis, the above transformation applied to the ex vivo tree was inverted and applied to the original tracing of the in vivo tree in in vivo space. This resulted in the in vivo centrelines being aligned to the ex vivo image. Manual selection of a background threshold for the ex vivo image was performed, and the contrast-to-noise ratio (CNR) at each vertex was calculated by subtracting the mean background signal from the vertex signal and dividing this result by the standard deviation of all background voxel signals. A vessel was categorized as unperfused if more than 50 % of the CNR values for all vertices in the vessel approached zero.

2.3.4 Extracting quantitative parameters for comparisons between in vivo/ex vivo networks

The capillary bed possesses a net-like architecture, while the arteriolar and venular structure is tree-like [175]. Analyses of vascular architecture often separate larger from smaller diameter vessels [175]. A capillary for this study was defined as a vessel segment with a diameter less than 8 μm that was not defined as a penetrating vessel (see below). A threshold of 8 μm was selected based on the inflection point in the histogram of diameter distributions as proposed in Risser et al. [176]. A segment was defined as the part of a network between either of two bifurcations, or between a bifurcation and non-connected segment end, or between two non-connected segment ends.

Penetrating vessels were extracted from the vascular tree by visually examining the tree and placing a marker inside the part of a penetrating vessel determined to be closest to the cortical surface. This vessel was traced downwards starting from the marker. At each bifurcation, the tracing algorithm followed the vessel segment making the smallest angle with the normal to the cortical surface. Tracing of a penetrating vessel ceased upon the marker reaching the end of a vessel segment not connected to any vessel below it. Penetrating arterioles were identified as those vessels having relatively few branches across the cortical depth, a relatively constant diameter, and are surrounded by a capillary-free space. Penetrating venules, in contrast, were identified as those with more branches, a smaller capillary-free space, and an increasing diameter moving towards the cortical surface [177, 178].

The radius at each vertex of the centerline network was computed. To calculate the radius of a vessel segment, the radii of all vertices comprising the segment were averaged. The vessel signal was defined as the mean of all voxel signals within that segment.

2.4 Results

Accounting for the spatially varying PSF in the ex vivo data had the greatest effect for smaller vessels less than 5 µm in diameter. This resulted in an error in diameter calculation of up to slightly greater than 7 % for these vessels (see Figure 2.3). The effect of incorporating the spatial variance of the PSF was very small (error reduction less than 2 %) for the vessels with diameters larger than the PSF z-extent (about 5 µm) (see Figure 2.3).

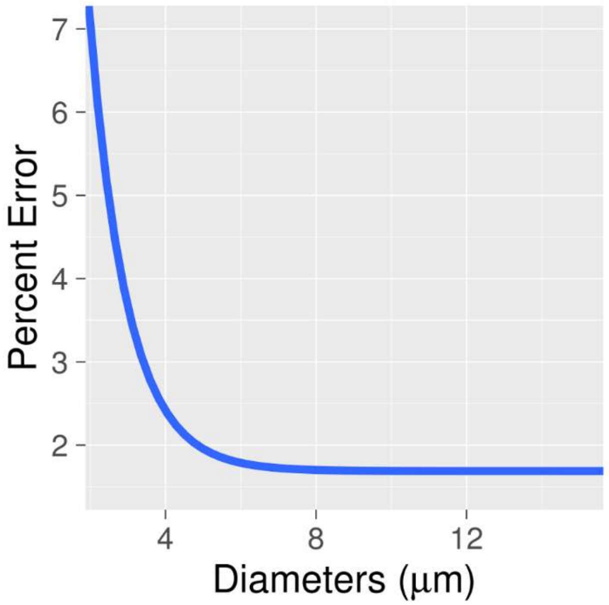

Figure 2.3. Percent error in diameter estimation as a function of vessel diameter. For this figure, an ex vivo image was tracked assuming a spatially varying PSF, using values from the straight-line fits in Figure 2.2. Diameters were then recalculated for each tracked vertex assuming an unchanging PSF-width with image depth. The percent difference on this plot is the percent difference between the diameter calculated while accounting for a changing PSF, and that calculated without accounting for this spatial variance. The x-axis is the diameter calculated assuming a changing PSF (ie. the diameter initially calculated). The line displayed is an exponential fit to the data. For the small vessel diameters, where the size of the PSF is close to that of the vessel, the percent difference is appreciable. For vessels with diameters above 5 µm, this effect is much smaller (< 2 %).

The vessel signal as a function of diameter and depth is plotted in Figures 2.4A and 2.4B respectively. Signal increases as a function of vessel diameter (Figure 2.4 A). The normalized signal is greater in vivo compared to ex vivo for vessels with diameters below 6 µm. Microvascular signal decreases with depth at a faster rate in vivo compared to the ex vivo data, with a relatively rapid drop-off beginning at about 400 µm below the cortical surface (Figure 2.4B). The characteristic attenuation length in vivo was 171 ± 15 µm across the four mice. This was calculated following the method of Kobat et al. [179], who measured the attenuation length to be 131 µm at 775 nm excitation, and 285 µm at 1280 nm. Axial slices at different depths are shown in Supplemental Figure 2.1 for one of the in vivo/ex vivo data sets.

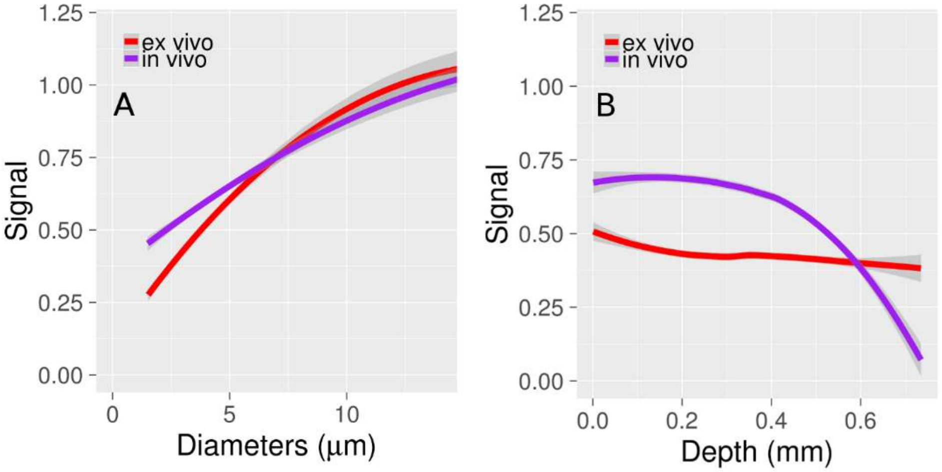

Figure 2.4. Vessel signal as a function of diameter and cortical depth. (A) Vessel signal as a function of diameter. Signal is normalized for the ex and in vivo data by calculating the mean signal of all vessels above 10 µm diameter in each of the 4 images. The signal for each vessel is calculated separately for each image. The mean signal for vessels above 10 µm diameter is given an arbitrary value of 1, and the signal for all vessels is calculated relative to this normalized value. Smaller vessels have a weaker signal ex vivo compared to in vivo, likely due to the larger PSF ex vivo. (B) Capillary signal as a function of cortical depth. The in vivo signal is constant for the first several hundred microns, before decreasing quickly with depth (characteristic attenuation length of 171 ± 15 µm). In contrast, the ex vivo signal maintains its strength through the cortical thickness. The lines in Figs A and B are fits to the data, and the ribbons surrounding the lines are the 95 % confidence intervals.

Hemoglobin absorbs and scatters light, and its presence in large numbers in large diameter pial surface vessels cause regions of an image beneath them to appear dark. This is termed a shadowing artifact, and often renders small structures beneath the cortical surface invisible under fluorescent microscopy [180]. Regarding visualizing the microvasculature, shadowing either blocks signals from capillaries or diminishes them entirely and contributes to reduced imaging depth. Figure 2.5A plots the signal from shadowed and unshadowed microvessels, where shadowed vessels are defined as those located directly beneath a surface pial vessel.

Although the signal from shadowed and unshadowed vessels in vivo is equally weak at depths greater than 0.6 mm, at shallower depths the difference is significant. The shadowing artifact is absent ex vivo (Figure 2.5B). The plots in Figs 2.4 and 2.5 were obtained by amalgamating the data from all vessels in the four pairs of images. Fitting was performed in R using Loess regression [181].

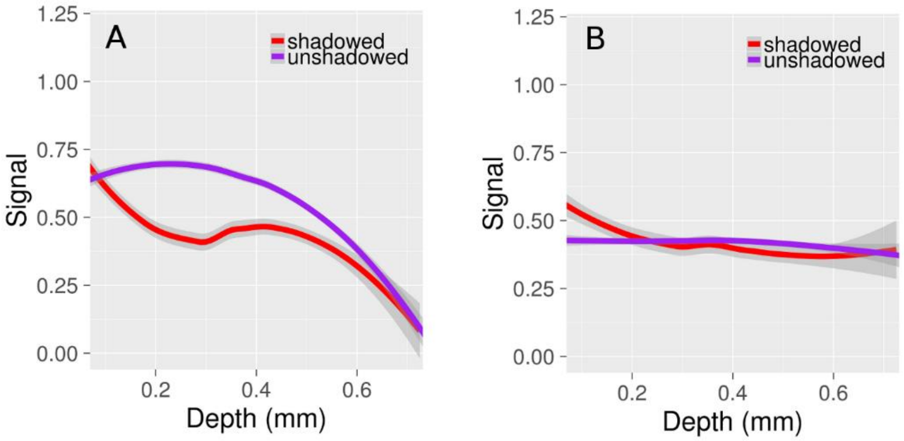

Figure 2.5. The impact of vessel shadowing on capillary signal. (A) In vivo. (B) Ex vivo. The shadowing artifact is noticeable absent ex vivo (no difference in signal between shadowed/unshadowed vessels), but significant in vivo for depths below 0.6 mm.

98.6 ± 0.7% (mean ± sem) of capillaries were successfully perfused by the fluorescent gel (average calculated over all four specimens). Unperfused capillaries possessed smaller diameters (3.74 ± 0.09 µm) compared to those that were perfused (4.12 ± 0.01 µm) ($p = 0.0001$; Student's t-Test; data pooled from all mice).

Figure 2.6 demonstrates the extent of diameter shrinkage as a function of in vivo vessel diameter. Ex vivo capillary diameters throughout the cortex were slightly smaller than those measured in vivo (3.6 ± 0.5 µm vs. 4.2 ± 0.4 µm), but this difference was not statistically significant (p = 0.06; Student's t-Test) and varied between specimens (0 % to 26 %). In a one-to-one comparison of in vivo to ex vivo capillaries, 76 % of capillaries were larger in vivo compared to ex vivo (p = 0.047). At the level of the penetrating vessels, the mean shrinkage was 34 % over all mice. In vivo, the mean artery diameter (6 arteries) was 11.4 ± 0.7 µm, while the mean venule diameter (19 venules) was 8.9 ± 0.8 µm (p = 0.02). The ratio of ex vivo to in vivo penetrating vessel diameters did not differ significantly between arteries and veins across the 4 mice (0.69 ± 0.08 arteries; 0.63 ± 0.06 veins; p = 0.6). Supplemental Figure 2.2 shows the vessel shrinkage ex vivo as a function of vessel diameter for each of the individual capillaries, arteries, and veins. Even though mean shrinkage is 31 % for arteries and 37 % for veins, this shrinkage is variable. Some veins, for example, undergo almost no shrinkage, while others undergo more than 50 %. These diameter differences cannot be attributed to penetration of the glycocalyx by SR101, since vessel diameters in vivo measured with SR101 were indistinguishable at the resolution of the imaging system from those measured with FITC dextran (see Supplemental Figure 2.3).

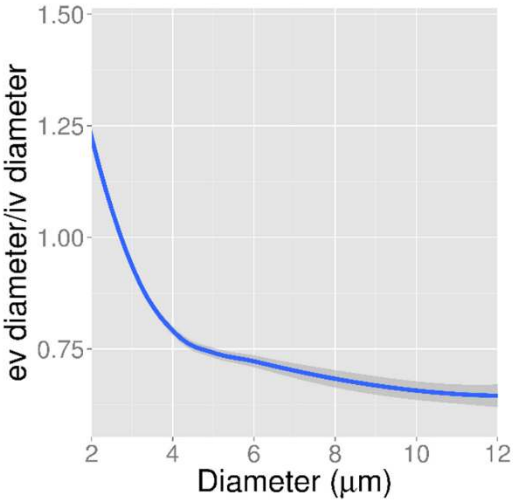

Figure 2.6. Ratio of ex vivo: in vivo vessel diameters as a function of in vivo vessel diameter. For each vessel, the ratio of its diameter ex vivo (after correction for refractive index mismatch) to that in vivo was computed. In this figure are the ratios computed for all vessels pooled together from the four mice.

2.5 Discussion

This paper presents a methodology for ex vivo imaging and calculation of vessel diameter in the presence of spherical aberrations. It presents a unique method for comparing in vivo to ex vivo images through precise analysis of corresponding vessels in the two types of data. Novel ex vivo techniques are being continuously developed, and the methodologies demonstrated here can be applied to any variety of clearing materials or imaging modalities. Tsai et al. [6] previously compared vessel diameters between in vivo and ex vivo 2PFM. In their study, average diameters were compared in different mice, whereas in the present study, corresponding vessels from the same mice were compared. Their comparison with in vivo vessels was limited to vessels less than 100 μm below the cortical surface. In our study, the impact of pial vessels on capillary signal deep in the cortex was examined, together with the change in the microvascular signal as a function of depth and diameter. To accurately compare inner vessel diameters in vivo/ex vivo, the contrast agents used (either SR101 or the gel) must fill the lumen entirely without penetrating the glycocalyx or endothelial cell layers. FITC albumin is sufficiently large such that it does not penetrate the glycocalyx and only fills the lumen. Previous studies have demonstrated that SR101, a smaller molecule, is contained within the lumen and provides a reliable measurement of inner vascular diameter. For example, Sekiguchi et al. [182] estimated a difference of approximately 1 µm for pial artery diameters measured based on GFP-fluorescent endothelial cells versus those with plasma labelled with SR101. Further, Choi et al. [183] overlaid in vivo 2-photon vascular images of plasma-labelled SR101 and 2 MDa FITC dextran, demonstrating similarities in vessel diameters. Our own experiments indicate that there are no detectable diameter differences, at the resolution of our imaging system, between vessels labelled with either SR101 or FITC (see Supplemental Figure 2.3).

Past studies of brain microcirculation have used corrosion casting and/or histology. Due to the high resolution of electron microscopy and the 2D rendering of 3D surfaces, corrosion casting allows for a qualitative analysis of microvascular structure. Quantitative metrics, however, such as vessel length, rely on the angle at which the cast is viewed and are inconsistent between specimens if not accounted for [184]. In addition, because the tissue support is dissolved, finer vessels may break off the cast during corrosion, while imaging depth is limited unless the cast is dissected. In contrast, 2PFM with optical clearing enables visualization deep into tissue, without the need for dissection. As demonstrated here, the gelatin perfusate consistently fills more than 98 % of the vasculature, whereas perfusion materials for corrosion casting are often more viscous. Since the tissue is not dissected, the brain is preserved for histological analysis at later time points. This may enable cellular-level tissue information to be correlated with vascular changes. Although the perfusion materials described here (2 % gelatin with FITC-albumin) have been previously utilized, the authors Tsai et al. [6] combined this perfusion with clearing in 60 % sucrose, resulting in an average imaging depth of 700 µm. Fructose, in contrast, may yield imaging depths up to 8 mm [169]. Ex vivo imaging depth in this study was only limited by the technical specifications of the microscope (2mm, the objective working distance) although we chose to image no deeper than the cortical depth, often a little over 1 mm. The mean in vivo imaging depth was 650 ± 45 µm, with a significant drop in contrast and signal at depths below 0.4 mm.

Ex vivo images may be significantly distorted when the refractive index of the clearing agent differs significantly from that of the immersion medium, typically water for long working distance microscope objectives. Multiphoton processes are strongly influenced by aberrations since absorption probability depends non-linearly on the focal intensity. These aberrations can be eliminated through specialized lenses which use the clearing agent as an immersion medium [165, 169]. This route is costly, however, unlike the methodology presented in this paper.

Our methodology for accurately calculating vessel diameter has potential for application to other 3D microscope-based imaging techniques. Light sheet microscopy utilizes a thin sheet of light focused with a cylindrical lens to excite fluorescence within a sample, which is collected by a detection objective lens [185]. The PSF in light-sheet methods is obtained by combining the detection and illumination PSFs. This produces a system PSF with different FWHMs in the lateral and axial dimensions, similar to 2-photon [186]. Light sheet microscopy may be combined with optical clearing methods to image large samples, such as entire rat brains at micron-level resolution [187]. Due to the combination of excitation light-sheet generation with widefield detection, imaging of an entire mouse brain may be accomplished in under one week at µm-scale resolution [188]. Imaging of a similar volume of tissue with 2-photon would require months.

Capillary diameters were smaller on average by 13 % ex vivo compared to in vivo ($p = 0.06$), although this shrinkage was non-significant, while 76 % of capillaries were smaller ex vivo. One possible explanation is differences in pressure during perfusion at constant flow rates ex vivo in comparison with those in a live animal. An advantage of constant flow rate (as opposed to constant pressure) is that a flow rate sufficiently high may be selected to maximize the percent of vessels perfused. Craniotomies and tissue fixation may induce changes in tissue dimensions, such as swelling, leading to vascular compression. Despite these possibilities, mean capillary diameter differences between the two techniques is only 0.6 µm, while other techniques yield capillaries with comparable diameters to our reported values. As an example, India Ink perfusion techniques (India Ink dissolved in gelatin) yielded mean capillary diameters of 3.48 µm, with diameters ranging from 1.708 µm to 9.626 µm [189], while Tsai et al. [6] have reported an average diameter of mouse microvessels of 3.5–4.0 µm. These compare favourably with our mean capillary diameter of 3.6 µm. Although Tsai et al. [6] found vessel diameters ex vivo to match those in vivo, the in vivo measurements were performed on awake mice, whose diameters were not dilated by isoflurane. Their perfused mice were anaesthetized with pentobarbital (Nembutal), not ketamine/xylazine as in this study. The vasodilatory effects of barbiturates such as pentobarbital are well-known [190].

Shrinkage dependence on diameter was also demonstrated. This was possible due to the correspondence between in vivo-ex vivo vessels. To overcome the effects of shrinkage on vessel network quantification, diameters are often multiplied by a scaling factor [176]. Our findings suggest this may not be the optimal approach. Large diameter vessels may experience the most shrinkage, while the smallest capillaries may be larger ex vivo compared to in vivo. This finding may serve to caution researchers that ex vivo images should be calibrated at the outset to permit accurate diameter estimation.

Some of this shrinkage is attributable to the isoflurane anaesthesia in vivo. Isoflurane is a potent dilator of microvessels and induces breakdown of the blood-brain-barrier [191], whereas ketamine (the anaesthetic under which the mouse was perfused) has been shown to constrict arterioles in rat skeletal muscle by as much as 30 % [192]. Under 1 % isoflurane, capillary diameters relative to those exposed to ketamine/xylazine in cortex dilate by a factor 1.24, while under 3 % isoflurane they dilate by a factor 1.85 [191]. Gao et al. [193] showed that 2 % isoflurane dilates surface and intracortical arterioles by approximately 40 %. The magnitude of these differences is comparable to our findings.

Factors beyond anaesthesia may influence in vivo/ex vivo diameter measurements. Arterial pCO_2 affects vascular tone and can rise if an animal hypoventilates under anaesthesia. In addition, Navari et al. [194] have demonstrated that atmospheric exposure of the brain during craniotomy may reduce tissue CO_2, resulting in arteriole constriction. Edema, which can be caused by craniotomy, may result in tissue swelling and increased intracranial pressure [71], leading to a compression of vessel diameters. Given these factors which bias estimates of vessel diameter under in vivo and ex vivo conditions, it is important that studies of disease or abnormal physiological states makes use of appropriate control conditions so that the differential effect of the intervention on vessel dimensions can be assessed. In general, estimation of vascular resistance from microvascular dimensions should be approached cautiously because small errors in vessel diameter are amplified when the corresponding vascular resistance is computed [162].

Despite a mean shrinkage of capillaries by 13 %, this number is still sufficiently small such that the technique could be used to assess changes in vessel diameters in various disease states. For example, following 1 hour of reperfusion after global cerebral ischemia in gerbils (15-minute bilateral carotid artery occlusion), capillary and precapillary arteriole diameters are reduced by 30 % and 24 % respectively [195]. 24 hours following a fluid-percussion Traumatic Brain Injury, vessel diameters are reduced by 13 % in injured cortex compared to non-injured cortex [21]. Although this is at the detectability limit of our in vivo-ex vivo comparison (mean shrinkage of capillaries of 13 % according to our data), our use of isoflurane in vivo likely exacerbated the difference between ex vivo and in vivo diameters; use of a different anaesthetic in vivo would likely enable subtler detection of diameter changes.

Larger vessels exhibited a stronger signal both in vivo and ex vivo (Figure 2.4A). This is probably due to the volume of excitation being entirely encompassed within the vessel, resulting in an increased number of fluorescent particles detected. The relative signal is greater for capillaries in vivo compared to ex vivo, which we attribute to the increased PSF size ex vivo. Depending on the imaging depth, this size could be on the order of a capillary. Signal steadily decreases with cortical depth in vivo (Figure 2.4B), with a sharp drop-off at depths greater than

0.4 mm. In contrast, the signal remains relatively constant ex vivo. A constant signal with cortical depth is an advantage of ex vivo imaging.

In vivo data displayed a shadowing artifact which was absent ex vivo (Figure 2.5). This artifact is likely due to the higher amounts of hemoglobin in the large vessels. At a hematocrit of 45% and wavelength of 633 nm, the scattering coefficient of blood is about 80 /mm, while its absorption coefficient is about 0.8 /mm [196]. When the hemoglobin has been flushed from the vasculature during perfusion and is replaced with a transparent gel, the shadowing artifact disappears ex vivo. In vivo imaging is limited in the field of view chosen as regions covered by large pial vessels will be challenging to image; however, ex vivo has no constraints in imaging location. Haiss et al. [180] solved this dilemma in vivo by replacing the blood with a perfluorocarbon emulsion. This method, however, would constrain the contrast agents used for visualizing the vasculature as they must now be miscible with the emulsion. We found with our specimens little difference in the signal between shadowed and unshadowed vessels beyond 500 µm depth. It is still difficult to confirm from our work that pial vessels do not limit imaging depth, as none of the fields of view chosen contained a large cluster of pial vessels. Imaging depth would likely be different in such a region compared to one devoid of pial vessels. For example, Haiss et al. [180] found that replacing blood with perfluorocarbon dramatically increases imaging depth below pial vessels and increases fluorescence intensity by almost a factor of 9. This suggests that in a region with a high pial vessel density, imaging depth is decreased by hemoglobin. While signal intensity varied across vessels in our study, all vessels present ex vivo were visible in vivo, regardless of location.

For all mice imaged, the perfusion success exceeded 98 %, in agreement with Tsai et al. [6] who quoted a high success rate with the same perfusion protocol (close to 100 %). The larger diameter of the perfused vessels compared to those unperfused suggest that perfused vessels had a lower resistance to fluid flow and were more easily filled by the gel. This agrees with the Hagen-Poiseuille equation, where the resistance scales with the inverse of diameter to the 4th power [162]. Thus, even a slight shrinkage in diameter may significantly impact the probability of a vessel being perfused.

2.6 Conclusions

Differences between vascular morphology and signal in in vivo and ex vivo 2PFM are quantified in this study. Through development of a protocol that enabled analysis of the corresponding vessels in both image types, previously unexamined features of 2PFM, such as shadowing, were precisely quantified. Most studies do not image corresponding regions with separate imaging techniques, which limits the scope of their analysis. This study employed specific perfusion and clearing techniques; however, much of the data and analysis methods is applicable to a range of clearing materials and situations. The vessel tracking algorithm which accounts for spherical aberrations is applicable to any data set and combination of microscope objective and clearing materials, merely requiring acquisition of PSF data. The ability to accurately segment and quantify vessel properties is critical since for small capillaries the signal is weaker ex vivo compared to in vivo.

In conclusion, we have presented a novel imaging and analysis methodology for visualizing and analyzing the vasculature. This methodology outlined features of in vivo and ex vivo 2PFM, such as the influence of PSF on vascular signal, the impact of shadowing on microvascular signal, and the changes in vessel diameter. Overall, ex vivo imaging was found to be valuable for studying deep cortical vasculature.

2.7 Acknowledgements

A preliminary version of this work was published as a Conference Proceedings, SPIE Photonics West 2016 [197].

2.8 Supplemental Material

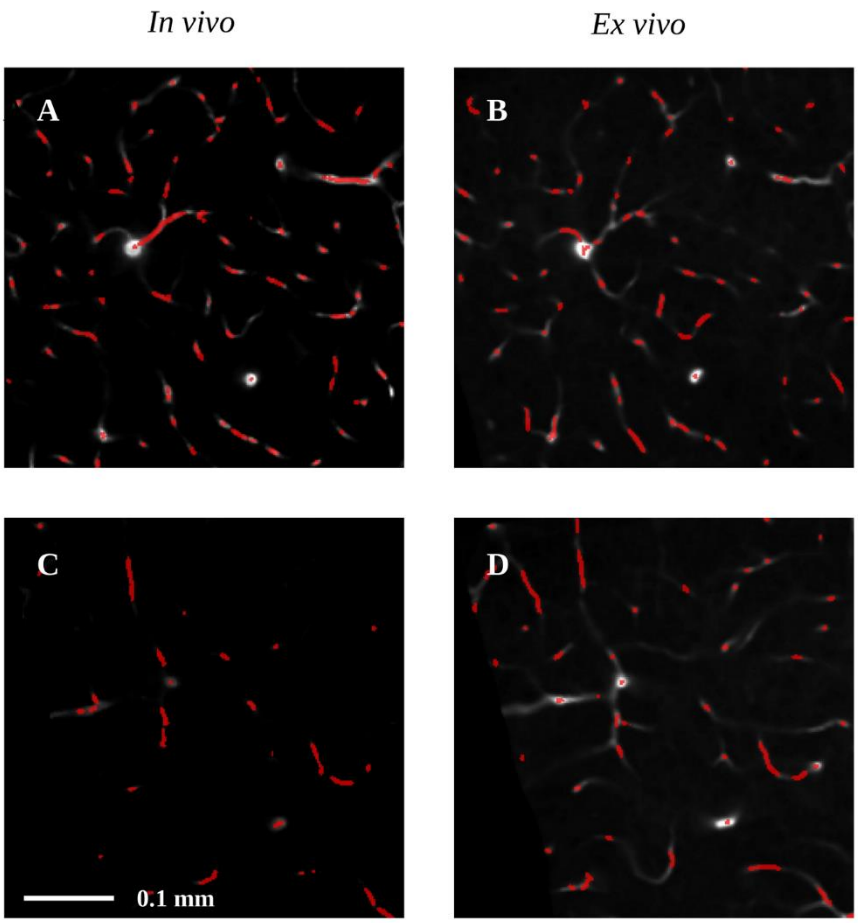

Supplemental Figure 2.1. Slices at different depths through a specimen imaged with 2-photon. Left column is in vivo, right column ex vivo. Centerlines of vessels are shown in red. A and B are 450 µm below the cortical surface, while C and D are 650 µm below the cortical surface. Although the signal between in vivo- ex vivo is comparable at 450 µm, the contrast to noise ratio ex vivo is noticeably greater at 650 µm.

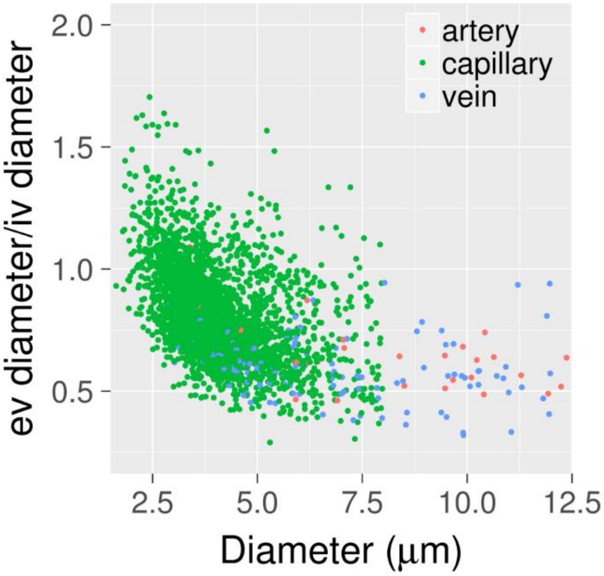

Supplemental Figure 2.2. Shrinkage of arteries, capillaries, and veins as a function of diameter. Each scatter point (which represents a vessel segment) is labeled as an artery (red), capillary (green), or vein (blue).

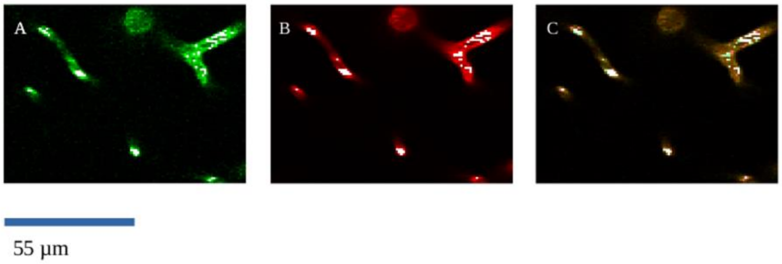

Supplemental Figure 2.3. Comparison of in vivo vessel diameters measured with SR101 and FITC dextran perfusion. (A) Image acquired on the FITC channel (B) Image acquired on the red (SR101) channel (C) Images A and B merged. The merging of the red and green channels produces a brown shading indicative of overlap between red and green signal. Because all vessels are entirely painted brown in C, it is concluded that vessel diameters *in vivo* measured with SR101 are indistinguishable at this resolution from those measured with FITC dextran. This suggests that any possible leakage of SR101 into the glycocalyx does not impact measurement of vessel diameter at the resolution of the imaging system.

Chapter 3

Acute and Chronic Stage Adaptations of Vascular Architecture and Cerebral Blood Flow in a Mouse Model of TBI

3.1 Foreword

A version of this chapter was posted as a pre-print on bioRxiv [198]:

Steinman J, Cahill LS, Koletar MM, Stefanovic B, and Sled JG. Acute and chronic stage adaptations of vascular architecture and cerebral blood flow in a mouse model of TBI. bioRxiv 2018.

The work for this chapter was accepted by NeuroImage [199]:

Steinman J, Cahill LS, Koletar MM, Stefanovic B, and Sled JG. Acute and chronic stage adaptations of vascular architecture and cerebral blood flow in a mouse model of TBI. NeuroImage 2019, doi: https://doi.org/10.1016/j.neuroimage.2019.116101.

3.2 Introduction

The 3D organization of vessels is an important factor in determining cerebral blood flow (CBF), with the vessel connections, shape, length, and diameter determining overall network resistance [162]. While regions of higher metabolic activity often show increased vessel density [113], substantial increases in density may not elevate flow by an equivalent amount [18]. This suggests that to understand the relationship between CBF and vascular structure, quantitative metrics beyond 2D measures of vessel density are needed. This vascular structure-blood flow relationship is thought to be important in a number of brain pathologies, including traumatic brain injury (TBI), where the vasculature undergoes significant damage, vessel loss, and regrowth [21, 22, 31, 86, 102].

Past studies have correlated CBF changes or functional outcome with vascular structural changes in TBI [22, 200], focusing on histological measures of density and diameter. Such 2D metrics of vascular morphology do not always correlate with blood flow. For example, vessel density in a hippocampal region correlated with CBF early post-injury in a lateral fluid percussion injury in rats [22]. At 8 months later in the same model, there was increased vessel density in perilesional cortex and reduced flow, with bilateral decreases in hippocampal CBF occurring without changes in vessel number [30].

Quantification of blood flow and vascular architecture is limited by the lack of availability of high-resolution 3D imaging techniques that may be combined with in vivo functional imaging. While optical clearing may be used to enhance light penetration, solvents often distort tissue and cause optical aberrations. A methodology with the ability to image the microvasculature in 3D over a large volume of tissue without optical clearing would overcome these deficiencies.

Automated techniques have been developed which image large regions of the murine brain without optical clearing [201]. One such technique, Serial 2-Photon Tomography (STPT), incorporates a 2-photon fluorescence microscope and vibratome [1]. The vibratome slices through tissue, enabling deep tissue imaging. To date, most STPT studies have acquired images at cellular-resolution in-plane with low through-plane resolution, typically with 75 – 100 µm spacing between coronal sections. This method enables whole-brain imaging in under 12 hours [29], but reduced through-plane resolution is not amenable to 3D vascular analysis.

In the present study, we used a combination of 2D Arterial Spin Labeling (ASL) MRI and STPT to measure changes in cerebrovascular function and to characterize the 3D vascular architecture in adult mice post-TBI. The standard STPT protocol was modified to obtain images at an isotropic voxel resolution of 2 µm, enabling 3D visualization and quantification of the geometry and branching patterns of the vascular network. Registration of the ASL data to the STPT images allowed us to correlate the differences in vascular structure with functional measures of flow under rest and hypercapnia. This paper highlights unique features of vascular architecture and blood flow, providing improved understanding of the role of the microvasculature in TBI recovery.

3.3 Materials and Methods

3.3.1 Animals

A total of 40 mice (19 male, 21 female, 12 - 13 weeks old, mean weight 24.2 g (CI: 23.1 – 25.3)), Cre x tdTomato (B6.Cg-Tg(Tek-cre)1Ywa/JxB6; 129S6-Gt(ROSA)26Sortm14(CAG-tdTomato)Hze/J), bred in-house, were used [202]. See Supplemental Table 3.1 for a detailed description of animal allocation within the study. The mice express a variant of red fluorescent protein in endothelial cells, under the direction of the Tie2 promoter [203]. Mice received either a controlled cortical impact (CCI) or craniotomy without impact (sham). They were permitted to recover 24 hours or 4 weeks post-injury. Mice were randomly assigned into one of four groups: TBI-1-Day, TBI-4-Weeks, Sham-1-Day, and Sham-4-Weeks. All animal experiments were approved by the Animal Care Committee at the Toronto Centre for Phenogenomics. Animal experiments were conducted in accordance with the Canadian Council on Animal Care's Guide to the Care and Use of Experimental Animals and complied with the ARRIVE guidelines.

3.3.2 Controlled cortical impact

Mice were anaesthetized with isoflurane (5 % induction, 1.5 - 2 % maintenance) in 100 % O_2. They were administered 5 mg/kg Baytril (Rompun, Bayer Inc., Toronto, Canada) and 1.2 mg/kg slow release buprenorphine (Chiron Compounding Pharmacy Inc., Guelph, Canada) subcutaneously, in addition to 1.5 mL of subcutaneous sterile saline (0.9 % NaCl). Mice were stabilized in a stereotaxic frame. Body temperature was maintained via a heating pad set to 37 ^{o} C. Immediately prior to scalp incision, mice were administered 0.2 mL of 1 % lidocaine (AstraZeneca, Mississauga, Canada) subcutaneously over the skull. The scalp was shaved, then cleaned with alcohol and betadine solutions. A craniotomy approximately 2.2 mm in diameter was performed and centred at 1.5 mm posterior to bregma and 1.7 mm lateral to the midline on the left hemisphere. A TBI (1.5 mm diameter tip, 1 mm depth, 2 m/s speed, 200 ms dwell time) was delivered with an electromagnetically driven piston [72]. The craniotomy was sealed with a 5 mm diameter glass coverslip (World Precision Instruments, Sarasota, Florida, USA). The scalp was sutured; betadine and polysporine were applied to the incision. Each mouse was individually housed in a sterile cage with DietGel (76 A, PharmaServ, Framingham, MA, USA) and food pellets placed at the bottom of the cage. Mice had ad libitum access to food and water in a pathogen-free environment on a 12-hour light: dark cycle. Identical procedures were performed for shams, with the exception of the impact.

3.3.3 Measurement of CBF with continuous Arterial Spin Labeling (CASL)

Prior to CASL imaging, in vivo ultrasound imaging under isoflurane was performed as described previously [125]. The ultrasound data is beyond the scope of the current study and will be the subject of future investigations.

The ASL procedure followed that described in Cahill et al. [125] and is summarized below.

Imaging preparation and hypercapnia protocol: Immediately following ultrasound, mice were endotracheally intubated and mechanically ventilated under 1 % isoflurane in 100 % O_2. 0.1 mg/kg pancuronium bromide (Sigma-Aldrich, St. Louis, USA) was injected intraperitoneally for muscle relaxation and optimal breathing control during imaging. Partial pressure of carbon dioxide, respiration rate, and temperature were monitored. Each mouse underwent a CO_2 challenge, composed of an inhaled gas mixture alternating between rest (30 % O_2 : 70 % N_2) and hypercapnia (5 % CO_2 : 30 % O_2 : 65 % N_2). In total, there were 5 – 6 scans per mouse, with two of the scans under hypercapnia. Following hypercapnia, there was a 6-minute break between measurements to allow for return to normal physiological state.

ASL: 2D CASL measurements were performed with a 7T 40 cm horizontal bore magnet produced by Agilent with 16 transmitters and 16 receivers. A custom-built dual-saddle volume coil with inner diameter 2.5 cm and axial field view 3 cm was used for CASL measurements. A 2 mm-thick coronal slice intercepted the centre of the TBI site and the labeling plane was positioned posterior to the imaging slice by approximately 0.8 cm. Each repetition included a 3-s 9-µT RF labelling pulse and a 500 ms post-label delay. The control label condition consisted of a labeling plane 0.8 cm anterior to the imaging slice. The CASL images were acquired using a 2D fast spin-echo sequence with TR = 6000 ms, TE_{eff} = 15 ms, echo train length = 16, slice thickness = 2 mm, matrix size 200 x 384, in-plane resolution of 250 µm. CBF was calculated with a single-compartment biophysical model with correction for the magnetization transfer enhancement of T_1 relaxation [3, 125]. As TBI may cause edema [204] and influence tissue T_1, affecting CBF measurements [3], T_1 was mapped in the same 2 mm-thick coronal section using an inversion recovery fast spin-echo sequence (TR = 5000 ms, TE = 11ms, inversion times = 50, 100, 200, 400, 800, 1600, 3200 ms).

Our group has previously [125] measured the inversion efficiency in six adult C57BL/6J mice using a 2D flow compensated spoiled gradient echo sequence with inversion and imaging planes positioned on the carotids and separated by 5 mm. The measured inversion efficiency of 0.80 ± 0.03 was consistent with estimates based on simulations reported previously for the mouse carotid [3].

3.3.4 T_2-weighted whole brain in vivo anatomical imaging

T_2-weighted whole brain images were acquired using a 3D fast spin-echo sequence with the following parameters: TR = 1800 ms, TE_{eff} = 40 ms, echo train length = 12, matrix size 120 x 144 x 72, isotropic image resolution = 292 µm. The acquired image was used as an intermediary in a registration pipeline to align the STPT images to ASL data (see below).

3.3.5 Brain sample preparation

The perfusion protocol have been described elsewhere [6, 26, 158] and is briefly summarized here. Immediately following in vivo MRI, mice were anaesthetized with an IP injection of 100 µg/g ketamine and 20 µg/g xylazine. The following solutions were perfused through the left ventricle, with 2 mM ProHance (Bracco Diagnostics Inc., Monroe Plains, New Jersey, USA) added to each solution for MR contrast: 30 mL of 0.1 M PBS (Wisent Inc., Quebec, Canada) containing 1 µL/mL heparin (1000 USP units/mL); 20 mL of 4% paraformaldehyde (PFA) (Electron Microscopy Sciences, Hatfield, Pennsylvania, USA); and 20 mL of a 2 % gelatin solution (Sigma, St. Louis, USA) containing 0.5 % (w/v) FITC-conjugated albumin (Sigma) [6]. Mice were decapitated and the brains within the skull were fixed overnight at 4^o C in 4 % PFA with 2 mM ProHance. Brains were transferred to PBS containing 2 mM ProHance and 0.02 % sodium azide for at least one week [205].

3.3.6 Ex vivo whole-brain MRI

The same MRI scanner was used for ex vivo imaging as that for in vivo imaging. Brains were scanned in a 16-coil solenoid array [206] using a T_2-weighted 3D fast spin-echo sequence with a cylindrical *k*-space acquisition [207]**.** Sequence parameters were 4 averages, TR = 350 ms, TE_{eff} = 30 ms, echo train length = 6, matrix size 504 x 504 x 630, isotropic image resolution = 40 µm.

3.3.7 3D Serial Two-Photon Tomography

STPT was imaged on two channels as previously described [29]. Light emitted from the specimen was split using a 516 nm single-edge dichroic beamsplitter (Semrock FF516-di01-25 x 36). Due to the greater signal strength, only the data from the channel with light greater than 516 nm wavelength were analyzed: this channel provided signal from both the tomato fluorescent protein and the gelatin: FITC-conjugate.

2-photon fluorescence imaging commenced 50 µm below the cut surface and involved collecting a mosaic of overlapping tiles. Each field-of-view (FOV) was sampled with 832 voxels along x and y for a 1.37 µm in-plane imaging resolution and acquired through a tissue depth of 100 µm, with 2 µm separation between tiles. Following acquisition of all 3D images within the xy-plane, the tissue was sliced 30 µm by a vibratome integrated with the translation stage and the sample moved towards the objective. STPT imaging began approximately 1 mm in front of the TBI site, extending 3 + mm into the tissue. A typical imaging session involved 150 vibratome sections, corresponding to a tissue volume of 4 mm (*x*) x 4 mm (*y*) x 4.5 mm (*z*) and an imaging time of approximately 33 hours. Scanning was performed coronally (ie. the imaging depth referred to by the z-direction is through a coronal plane). STPT data was not acquired for the contralateral hemisphere.

3.3.8 STPT data processing and reconstruction

Each 3D image was corrected for uneven illumination using an agar phantom loaded with FITC. The 3D images were blurred in the xy-plane by a Gaussian with full-width-half-maximum (FWHM) of 2 µm and resampled to an isotropic voxel size of 2 x 2 x 2 μm^3. Image stitching was performed with a Fiji/ImageJ plug-in based on the algorithm of Preibisch et al. (https://imagej.net/Image_Stitching) [208], with overlapping 3D images merged via a linear blending algorithm.

3.3.9 Image registration pipeline

Registration of the ASL data to the STPT images was performed using in vivo and ex vivo whole-brain structural MR images as intermediate targets for registration as illustrated in Figure 3.1. Each image in the registration chain was registered to its subsequent image via a rigid body transformation.

Common landmarks were manually labelled between the T_2-weighted control ASL image (Figure 3.1A) and the T_2-weighted whole-brain in vivo structural MRI image (Figure 3.1B). The landmarks were used to calculate a rigid-body transformation from the ASL imaging space to the T_2-weighted whole-brain in vivo imaging space. The same process was repeated to calculate a rigid body transformation from T_2-weighted whole-brain in vivo to T_2-weighted whole-brain ex vivo (Figure 3.1C) imaging space, and from T_2-weighted whole-brain ex vivo to STPT (Figure 3.1D) imaging space. The transformations are concatenated to produce an overall transformation from ASL space to STPT space.

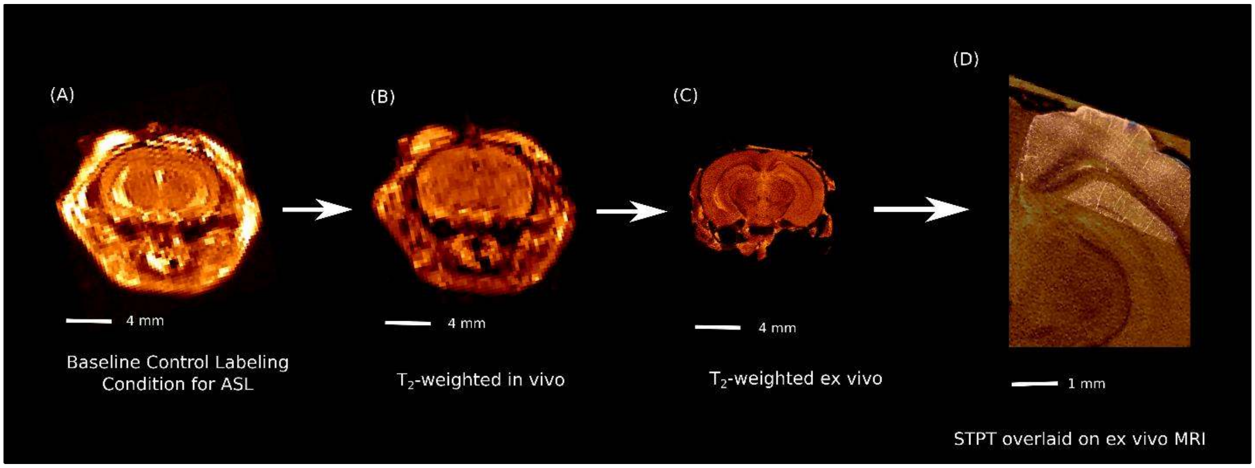

Figure 3.1. Registration of ASL to STPT through intermediate images. (A) Representative T_2-weighted anatomical image from the ASL acquisition (B) Single-slice from in vivo T_2-weighted whole-brain image (C) Single-slice from ex vivo T_2-weighted whole-brain with the skin and overlying tissue from the skull removed (D) Single-slice STPT, showing the ipsilateral cortex and part of the hippocampus overlaid on the ex vivo MR . To register the CBF maps to the stitched STPT images, the in vivo and ex vivo whole-brain structural MR images were used as intermediates in a registration pipeline based on manual identification of common landmarks between the respective images.

3.3.10 Vessel tracking

The vessel tracking segmentation algorithm has been described elsewhere [115, 158]. Tracking was initiated through automated placement of multiple seeds inside each putative vessel [158, 202]. Prior to tracking, cortical voxels in the ASL data were manually labelled by overlaying the control ASL image onto the STPT data in the same imaging space following the registration procedure. Since the ASL data is relatively low resolution (250 µm in-plane), it can be challenging with the ASL data alone to determine which voxels precisely correspond to the injury core. By overlaying ASL with high resolution (2 µm) STPT, it was easy to determine which ASL cortical voxels were located within the core. Cortical voxels were subdivided into two groups: (A) those within the craniotomy region (TBI site) projected through the cortical depth. This was termed the 'ipsilateral' injury zone, or 'core'. (B) Those outside the TBI site, termed the 'perilesional' region. The perilesional region contained the ASL cortical voxels outside the core.

These voxels intersected the STPT data, thus vascular structural information was still available for them. Ipsilateral voxels that corresponded to the centerline of the injury were further labelled ‘centerline’. The centerline voxels were later used to calculate the distance of the cortical voxels from the injury center (see below). Each voxel in the STPT image was assigned a label of ipsilateral or perilesional, based on the cortical ASL voxel type to which it corresponded. Only these voxels were tracked.

The datasets were pruned during post-processing to remove short, false vessels (‘hairs’) which are either disconnected from the vessel network or connected at only a single end to a parent vessel. These vessels are produced either by noise at a vessel boundary that is interpreted as a separate vessel or by the anisotropy (reduced resolution along the z-dimension compared to xy, causing vessels to have an elliptic shape) of the 2-photon fluorescence data causing short vessels to be traced parallel to the optical axis.

3.3.11 Data analysis

Quantification of vessel network properties: Vessel diameters calculated were the outer diameter, which is the sum of the lumen (inner) diameter and the vessel wall thickness. Vessels with diameters less than 8 µm were labelled capillaries, since capillary cut-offs in the literature typically range from 6 µm to 10 µm [6, 202]. All vessels traced emitted fluorescence greater than 516 nm and were either tomato-fluorescent and gel-perfused, or only tomato-fluorescent in the event that a given vessel was not perfused.

‘Centerline voxels’ in the ASL data (defined in *Vessel tracking*) were defined as 0 mm from the injury centre. The distance of all other cortical ASL voxels was defined by the Euclidean distance to the nearest centerline voxel. Each vessel segment in the SPTP data was assigned a nearest ASL voxel and distance from injury centre based on the position of the vessel segment’s midpoint. The vessel length density at each voxel was the sum of the lengths of all vessels within an ASL voxel divided by the voxel volume.

Quantification of radial vascular architecture: The vascular network at 4 weeks post-TBI (the TBI-4-Weeks group) possessed a different patterning relative to the other groups (TBI-1-Day, Sham-1-Day, Sham-4-Weeks). From the center of the injury at the cortical surface, vessels emanated outwards in a radial pattern. To quantify this feature, a marker was placed at the centre of the craniotomy on the cortical surface. Each segmented vessel was simplified as a straight line. Another line was defined connecting the vessel midpoint (average position between the two endpoints of the straight-line vessel) and marker. The angle between these two lines was calculated for all vessels, averaged, and compared between mice and groups. This metric is termed *radialness.* Vessel networks that display a radial pattern would be expected to possess a smaller mean angle. If all vessels emanated precisely from the marker, the angle for each vessel would be 0^{o}. See Supplemental Figure 3.1 for a diagram explaining calculation of radialness.

Statistical analysis: Data are reported as mean ± 95 % confidence interval (CI). Data analysis was conducted in Python and R. To compare mean differences between groups, the dependent variable was modelled as a linear function of group, and an ANOVA was performed on the linear model with $p < 0.05$ interpreted as significant. If $p < 0.05$, a Tukey Honestly Significant

Differences post-hoc test was conducted to assess between-group differences. See Supplemental Table 3.2 for summary statistics for each variable.

To assess if TBI influenced CBF, an ANOVA was performed on a linear mixed effects model where CBF was modeled as a three-way interaction between CO_2 state (rest vs. hypercapnia), time (1 day vs. 4 weeks), and treatment (TBI vs. Sham), with specimen as the random factor to account for repeated measures. For analysis of CBF as a function of distance from the injury centre, CBF vs. distance plots for each group were fit with a cubic spline with 3 degrees of freedom. An ANOVA was performed on a linear mixed effects model where CBF was modeled as a four-way interaction between distance (which was fit with a cubic spline), state (rest vs. hypercapnia), time (1 day vs. 4 weeks), and treatment (TBI vs. Sham), with specimen as the random factor. Coefficient of variation (COV) was defined as the ratio between the standard deviation of CBF in ASL cortical voxels divided by their mean value, times 100 %. An ANOVA was performed on a linear mixed effects model where COV was modeled as a four-way interaction between distance, CO_2 state, time, and treatment, with specimen as the random factor. For analysis of mean vessel length density, microvascular volume, extravascular distance, capillary diameter, and radialness within the TBI site, an ANOVA was performed on a linear model where these variables were modeled as a two-way interaction between time and treatment. To assess how density, volume, and extravascular distance changed as a function of distance from the injury centre, an ANOVA was performed on a linear mixed effects model where these variables were modeled as a three-way interaction between distance, time, and treatment.

3.4 Results

3.4.1 STPT images of the microvasculature demonstrate abnormal morphology following TBI

TBI-1-Day mice showed loss of vessels and altered vessel morphology (Figure 3.2). Panel 3.2A is a maximum intensity projection (MIP) of a coronal section of the cerebral cortex in a mouse that did not undergo craniotomy. Note the uniform vessel density and regular pattern of the vessel network. This contrasts with Panel 3.2C (MIP of a TBI-1-Day mouse), where fewer vessels are detected inside the injury core. Outside the core, many penetrating vessels are highly tortuous (Panel 3.2B).

Of the 10 TBI-1-Day mice, all displayed hyperintensity at the TBI site in the ex vivo T_2-weighted images, consistent with edema. 6/10 possessed a significant amount of edema extending through the entire cortical depth (approximately 800 µm below the cortical surface). In addition to edema, there was evidence of hemorrhage at the TBI site, indicated by dark regions in the T_2-weighted image. Light edema (up to 50 – 100 µm slight hyperintensity below the cortical surface) was present in only 2/9 Sham-4-Weeks mice. Only 4/10 TBI-4-Weeks mice displayed signs of edema. 6/8 Sham-1-Day mice showed evidence of edema extending from 50 – 250 µm below the cortical surface depending on the specimen. Hemorrhage was absent in the Sham-1-Day group.

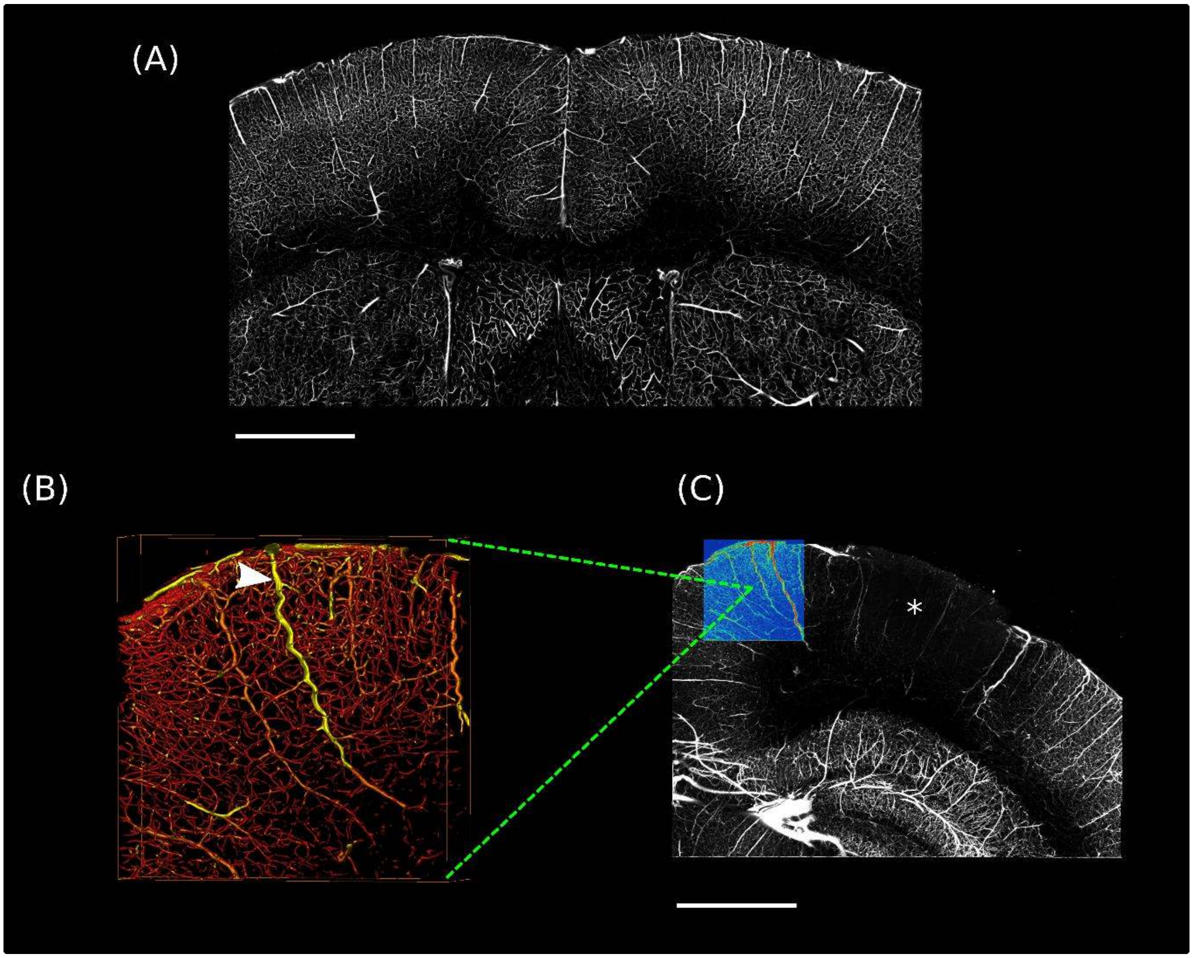

Figure 3.2. Images of the microvasculature obtained with STPT. (A) Maximum Intensity Projection (MIP) through 100 µm of tissue, acquired from a mouse that did not undergo craniotomy. Scale bar = 1 mm (B) and (C) Data acquired from a TBI-1-Day mouse. B is an isosurface rendering of 200 µm tissue thickness corresponding to the colored region in C. C is a MIP through 400 µm of tissue. Note the presence of tortuous (twisted) vessels in regions surrounding the impact core (arrowhead in B) and the reduction in vessel density within the core (asterisk in C). Scale bar = 1 mm. All data acquired with STPT.

3.4.2 Hypoperfusion in TBI persist up to 4 weeks

Figures 3.3A and 3.3B plot the mean CBF in the ipsilateral cortex (craniotomy region) under rest and hypercapnia. CBF depended significantly on CO_2 state ($F = 88.8$, $p = 7.0 \times 10^{-11}$) and treatment ($F = 14.8$, $p = 0.00052$ respectively), but not on time ($F = 0.5$, $p = 0.47$). There was a significant interaction between state and time ($F = 6.2$, $p = 0.018$). See Supplemental Figure 3.2 for representative CBF maps.

To investigate CBF outside the injured core, Figures 3.3C and 3.3D plot the CBF over the entire injured cortex as a function of distance from the injury centre under rest and hypercapnia respectively. There was a significant dependence on distance ($F = 31.5$, $p < 2.2 \times 10^{-16}$) and state ($F = 469.3$, $p < 2.2 \times 10^{-16}$), but not on treatment ($F = 2.8$, $p = 0.10$) or time ($F = 0.33$, $p = 0.57$). There was a significant interaction between distance and state ($F = 4.4$, $p = 0.0045$), state and time ($F = 6.4$, $p = 0.012$), and distance and treatment ($F = 3.7$, $p = 0.013$).

Figures 3.3E and 3.3F plot the COV for rest and hypercapnic CBF as a function of distance from the injury centre. COV depended significantly on CO_2 state ($F = 24.1$, $p = 1.5 \times 10^{-6}$) and treatment ($F = 7.1$, $p = 0.012$), but not on distance ($F = 1.4$, $p = 0.22$) or time ($F = 0.25$, $p = 0.62$). There was a significant interaction between state and treatment ($F = 11.9$, $p = 0.00064$).

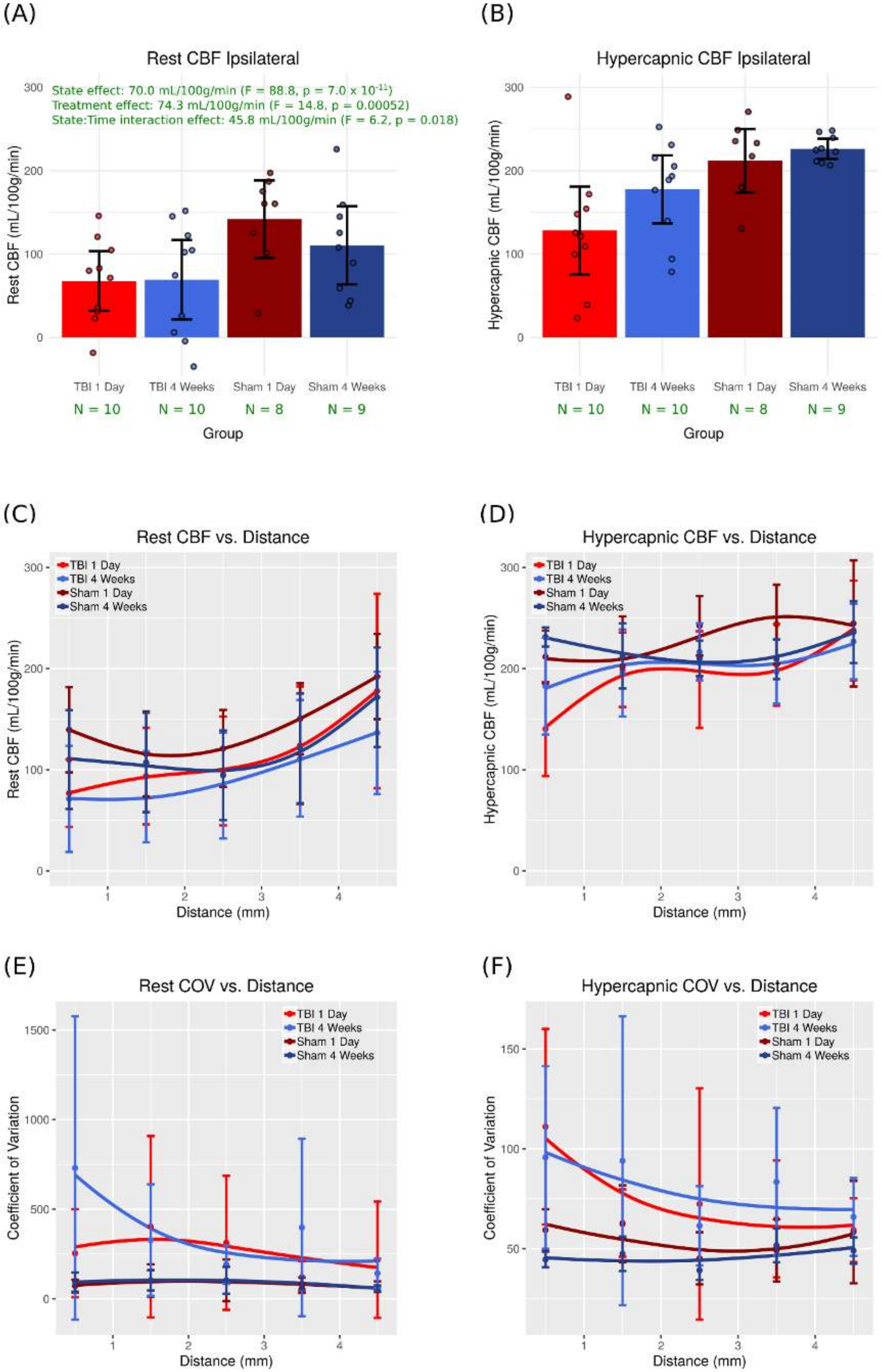
(A)
Rest CBF Ipsilateral
State effect: 70.0 mL/100g/min (F = 88.8, p = 7.0 x 10^-11)
Treatment effect: 74.3 mL/100g/min (F = 14.8, p = 0.00052)
State:Time interaction effect: 45.8 mL/100g/min (F = 6.2, p = 0.018)
Rest CBF (mL/100g/min)
0
100
200
300
TBI 1 Day
TBI 4 Weeks
Sham 1 Day
Sham 4 Weeks
N = 10
N = 10
N = 8
N = 9
Group
(B)
Hypercapnic CBF Ipsilateral
Hypercapnic CBF (mL/100g/min)
0
100
200
300
TBI 1 Day
TBI 4 Weeks
Sham 1 Day
Sham 4 Weeks
N = 10
N = 10
N = 8
N = 9
Group
(C)
Rest CBF vs. Distance
TBI 1 Day
TBI 4 Weeks
Sham 1 Day
Sham 4 Weeks
Rest CBF (mL/100g/min)
0
100
200
300
1
2
3
4
Distance (mm)
(D)
Hypercapnic CBF vs. Distance
TBI 1 Day
TBI 4 Weeks
Sham 1 Day
Sham 4 Weeks
Hypercapnic CBF (mL/100g/min)
0
100
200
300
1
2
3
4
Distance (mm)
(E)
Rest COV vs. Distance
TBI 1 Day
TBI 4 Weeks
Sham 1 Day
Sham 4 Weeks
Coefficient of Variation
0
500
1000
1500
1
2
3
4
Distance (mm)
(F)
Hypercapnic COV vs. Distance
TBI 1 Day
TBI 4 Weeks
Sham 1 Day
Sham 4 Weeks
Coefficient of Variation
50
100
150
1
2
3
4
Distance (mm)

Figure 3.3. **Mean CBF calculated with ASL MRI in the ipsilateral cortex under rest and hypercapnia**. The ipsilateral cortex refers to the craniotomy site determined following registration of ASL to STPT. CBF as a function of distance from the injury centre on the injured side under (C) rest and (D) hypercapnia. Coefficient of Variation as a function of distance from the injury centre under (E) rest and (F) hypercapnia. Data points are the mean ± 95 % CI, and fitting was performed with Loess regression. N refers to the number of mice.

3.4.3 Vessel density is reduced at 1-day post-TBI and recovers by 4-weeks

Figures 3.4A and 3.4B plot the mean vessel length density less than 1 mm from the injury centre, and the vessel density as a function of distance from the injury centre. In Figure 3.4A, vessel density depended significantly on time ($F = 15.4$, $p = 0.00048$) and treatment ($F = 28.2$, $p = 9.6 \times 10^{-6}$), with a significant interaction between time and treatment ($F = 9.1$, $p = 0.0052$). Post-hoc group comparisons indicated that vessel density at 1-day post-TBI (410 mm/mm^3 (CI: 260 – 560)) was reduced relative to Sham-1-Day (828 mm/mm^3 (CI: 703 – 953), $p = 1.1 \times 10^{-5}$) and 4 weeks post-TBI (742 mm/mm^3 (CI: 635 – 849), $p = 0.00032$). No significant reduction in density was present at 4 weeks post-TBI relative to Sham-4-Weeks (742 mm/mm^3 (CI: 635 – 849) vs. 858 mm/mm^3 (CI: 788 – 928) respectively, $p = 0.38$).

In Figure 3.4B, vessel density significantly depended on distance ($F = 36.1$, $p < 2.2 \times 10^{-16}$), time ($F = 12.8$, $p = 0.0012$), and treatment ($F = 25.1$, $p = 2.3 \times 10^{-5}$). There was a significant interaction between distance and time ($F = 3.2$, $p = 0.016$), distance and treatment ($F = 3.6$, $p = 0.0087$), and time and treatment ($F = 10.6$, $p = 0.0029$).

Figures 3.4C and 3.4D plot the rest and hypercapnic CBF vs. vessel density over all mice. There was a stronger correlation between hypercapnic CBF and density ($R^2 = 0.30$, $p = 0.00072$) compared to rest CBF and density ($R^2 = 0.10$, $p = 0.068$). There was no correlation between rest or hypercapnic CBF and capillary diameter ($R^2 = 0.071$, p = 0.13 and $R^2 = 0.0077$, p = 0.62 respectively).

Mean capillary diameter over all groups was 4.47 µm (CI: 4.37 – 4.57). Mean diameter did not display a time-dependence (F = 2.4, p = 0.13), but did depend on treatment (F = 11.9, p = 0.0017), with the diameter significantly elevated in the TBI condition relative to shams (4.62 µm TBI (CI: 4.54 – 4.70) vs. 4.33 µm Shams (CI: 4.17 – 4.49)). There was no significant interaction between time and treatment (F = 0.7, p = 0.41).

Microvascular volume and extravascular distance to the nearest microvessel followed a similar pattern to vessel density (Supplemental Figure 3.3). Microvascular volume depended significantly on time (F = 21.3, p = 7.0×10^{-5}) and treatment (F = 9.7, p = 0.0041), with a significant interaction between time and treatment (F = 7.2, p = 0.012). Volume for the TBI-1-Day group (0.74 (CI: 0.48 – 1.00)) was reduced relative to Sham-1-Day (1.29 (CI: 1.11 – 1.47), p = 0.0016) and TBI-4-Weeks (1.41 (CI: 1.19 – 1.63), p = 0.00012). There was no statistical difference between TBI-4-Weeks and Sham-4-Weeks (1.41 (CI: 1.19 – 1.63) vs. 1.45 (1.25 – 1.65), p = 0.99). In a plot of volume versus distance (Supplemental Figure 3.3B), there was a significant dependence on distance (F = 93.2, $p < 2.2 \times 10^{-16}$), time (F = 20.0, p = 0.00010), and treatment (F = 6.4, p = 0.017). There was a significant interaction between distance and time (F = 8.1, p = 0.0052), distance and treatment (F = 17.3, p = 5.6×10^{-5}), and time and treatment (F = 7.6, p = 0.0099).

The mean extravascular depended significantly on time and treatment (F = 5.2, p = 0.031; F = 18.0, p = 0.00020 respectively), with a significant interaction between time and treatment (F =

7.2, p = 0.012). Extravascular distance at TBI-1-Day (47 µm (CI: 35 – 59)) was elevated relative to Sham-1-Day (26 µm (CI: 22 – 30), p = 0.00018) and TBI-4-Weeks (33 µm (CI: 30 – 36), p = 0.012). There was no significant difference between TBI-4-Weeks and Sham-4-Weeks (33 µm (CI: 30 – 36) vs. 28 µm (CI: 23 – 33) respectively, p = 0.69). Extravascular distance depended on distance (F = 16.8, p = 6.4 x 10^{-11}), time (F = 6.4, p = 0.017), and treatment (F = 19.2, p = 0.00013) (Supplemental Figure 3.3D). There was a significant interaction between distance and treatment (F = 5.7, p = 0.00034), time and treatment (F = 7.8, p = 0.0088), and distance : time : treatment (F = 2.6, p = 0.039).

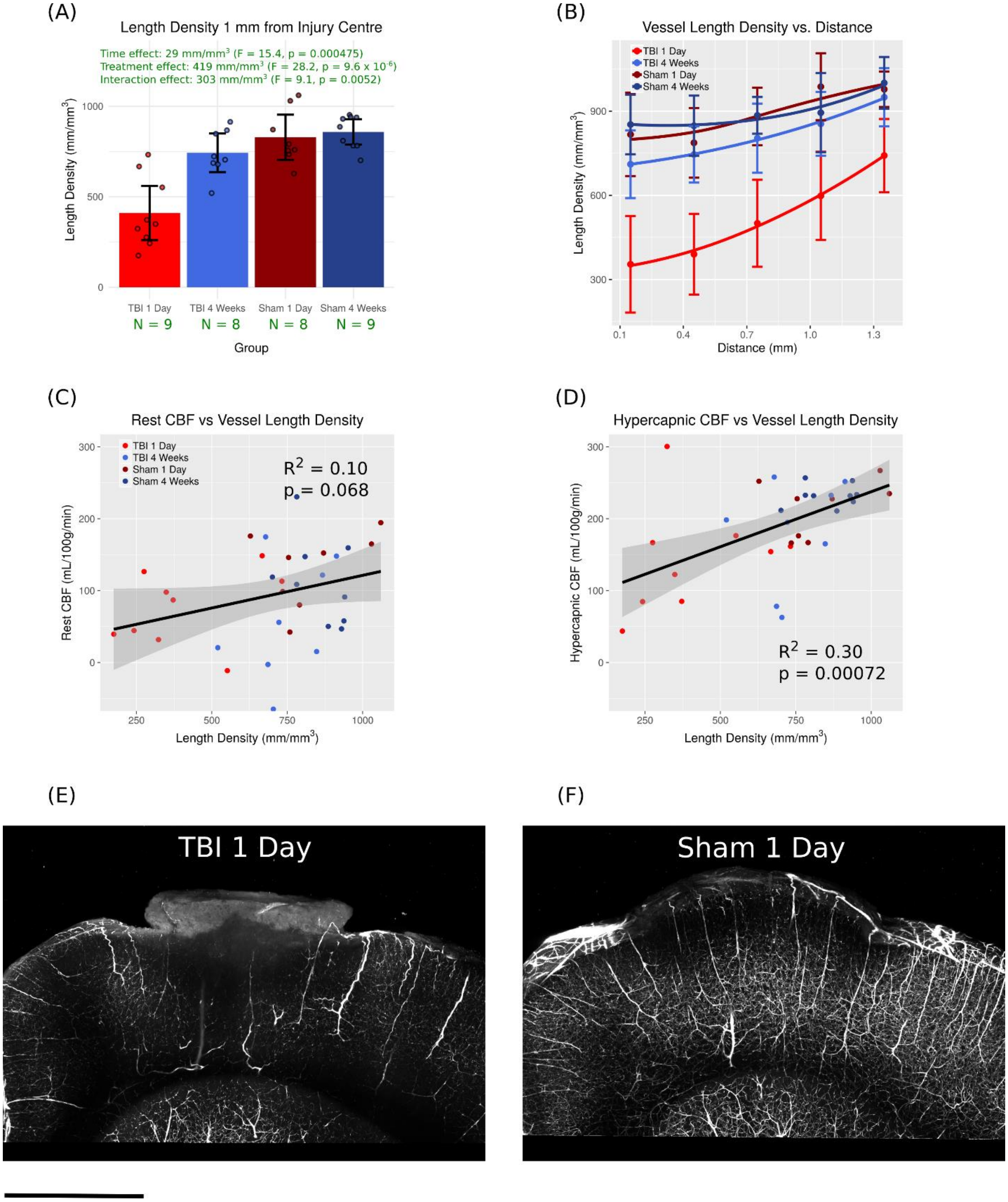

Figure 3.4. Analysis of vessel density and its relation to CBF. (A) Mean vessel density (B) Vessel density as a function of distance from the injury centre (C) Rest CBF vs. vessel density (D) Hypercapnic CBF vs. vessel density (E) and (F) MIPs through 400 µm of tissue in a TBI-1-Day and Sham-1-Day mouse respectively. Scale bar = 1 mm. Data points in A and B are the mean ± 95 % CI and N refers to the number of mice. Grey bands in C and D represent the 95 % confidence interval.

3.4.4 Correlation of Murray's Law with blood flow

In Murray's Law for vessel bifurcations, the cube of the parent vessel radius equals the sum of the cubed radii of the daughters [209, 210, 211]. It assumes vessel networks evolve to minimize the biological work required to transport blood. Many arterial trees closely follow Murray's Law [212, 213], and deviations from it may potentially indicate abnormal vasculature. Figure 3.5A is a log-log plot of the average number of vessels greater than or equal to a given diameter, normalized for density, for all vessels within 1 mm of the injury centre. This is termed a cumulative distribution curve. An optimally efficient network with symmetric bifurcations should produce a straight line with a negative slope for each group with a diameter scaling coefficient (absolute value of slope) of 3. For each mouse, a straight line was fit to its log-log plot of vessel diameter distributions, for diameters greater than or equal to 4 µm. 4 µm was selected as the minimum diameter since the average cumulative distributions become horizontal at smaller diameters. The mean diameter scaling coefficients for TBI-1-Day, Sham-1-Day, TBI-4-Weeks, and Sham-4-Weeks were 3.2 (CI: 3.0 – 3.4), 3.4 (CI: 3.0 – 3.8), 3.0 (CI: 2.7 – 3.3), and 3.1 (CI: 2.9 – 3.3) respectively. When scaling coefficient was modeled as a two-way interaction between time and treatment, there was a trend towards significance for time (F = 3.9, p = 0.058) but no dependence on treatment (F = 1.3, p = 0.27). There was no significant interaction between time and treatment (F = 1.1, p = 0.31). The mean cumulative distribution curve for TBI-1-Day was shifted lower than that of the other groups, indicating a decrease in vessel density (see Figure 3.5A). Both curves for TBI-1-Day and TBI-4-Weeks showed a 'dip' at approximately 8 µm.

Figures 3.5B and C plot the rest and hypercapnic CBF vs. scaling coefficient for vessels with diameters ranging from 4 – 50 µm. There is a much stronger correlation to the rest compared to hypercapnic CBF (R^2 = 0.19, p = 0.0097 vs. R^2 = 0.069 vs. p = 0.13 respectively).

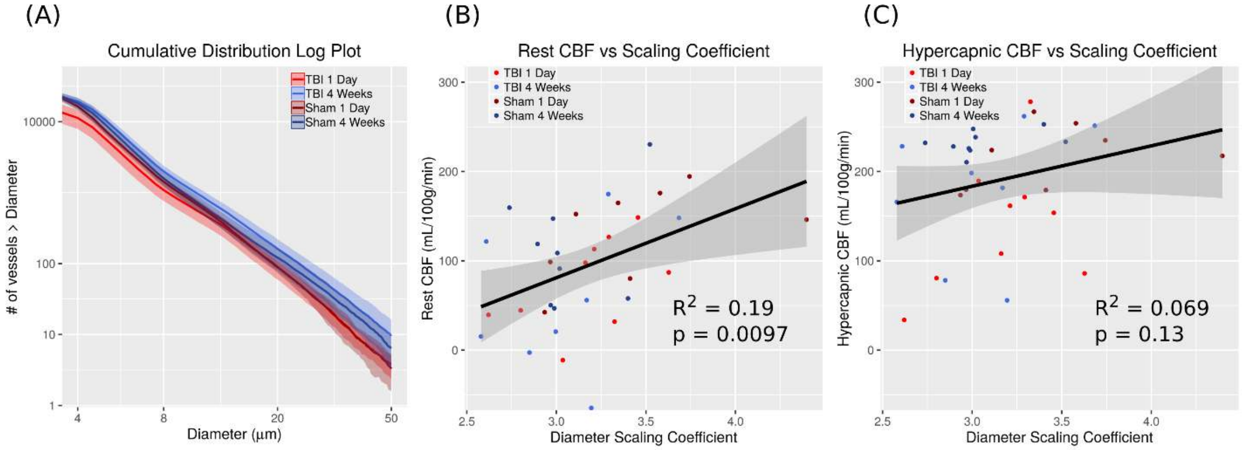

Figure 3.5. Application of Murray's Law to imaged vascular networks (A) Average log-log plots of the cumulative distribution of vessel diameters (B) Rest CBF vs. diameter scaling coefficient. (C) Hypercapnic CBF vs. diameter scaling coefficient. Each data point in B and C represents a single mouse. Grey bands in each panel represent the 95 % confidence interval.

3.4.5 The vascular architecture possesses a radial pattern at 4-weeks post-TBI

Figure 3.6A plots the percentage of vessels as a function of angle (see Methods) within the craniotomy region. There was an emphasis on smaller angles at TBI-4-Weeks relative to the other groups. This is visualized in Figure 3.6D, with vessels extending radially outwards from the injury centre at the cortical surface in a representative TBI-4-Week mouse, relative to Figure 3.6C, where there is a more random orientation of vessels in a representative Sham-4-Week mouse. *Radialness* (mean angle) depended significantly on time (F = 23.9, p = 3.2 x 10^{-5}) and treatment (F = 33.0, p = 2.9 x 10^{-6}), with a significant interaction between time and treatment (F = 18.5, p = 0.00017). There was a dependence of mean angle on group (F = 25.1, p = 2.5 x 10^{-8})

(Figure 3.6B). The mean angle at TBI-4-Weeks (49.4 (CI: 47.5 – 51.3)) was reduced relative to TBI-1-Day (55.4 (CI: 53.6 – 57.2), $p = 1.1 \times 10^{-6}$) and Sham-4-Weeks (55.8 (CI: 54.8 – 56.8), $p = 4 \times 10^{-7}$).

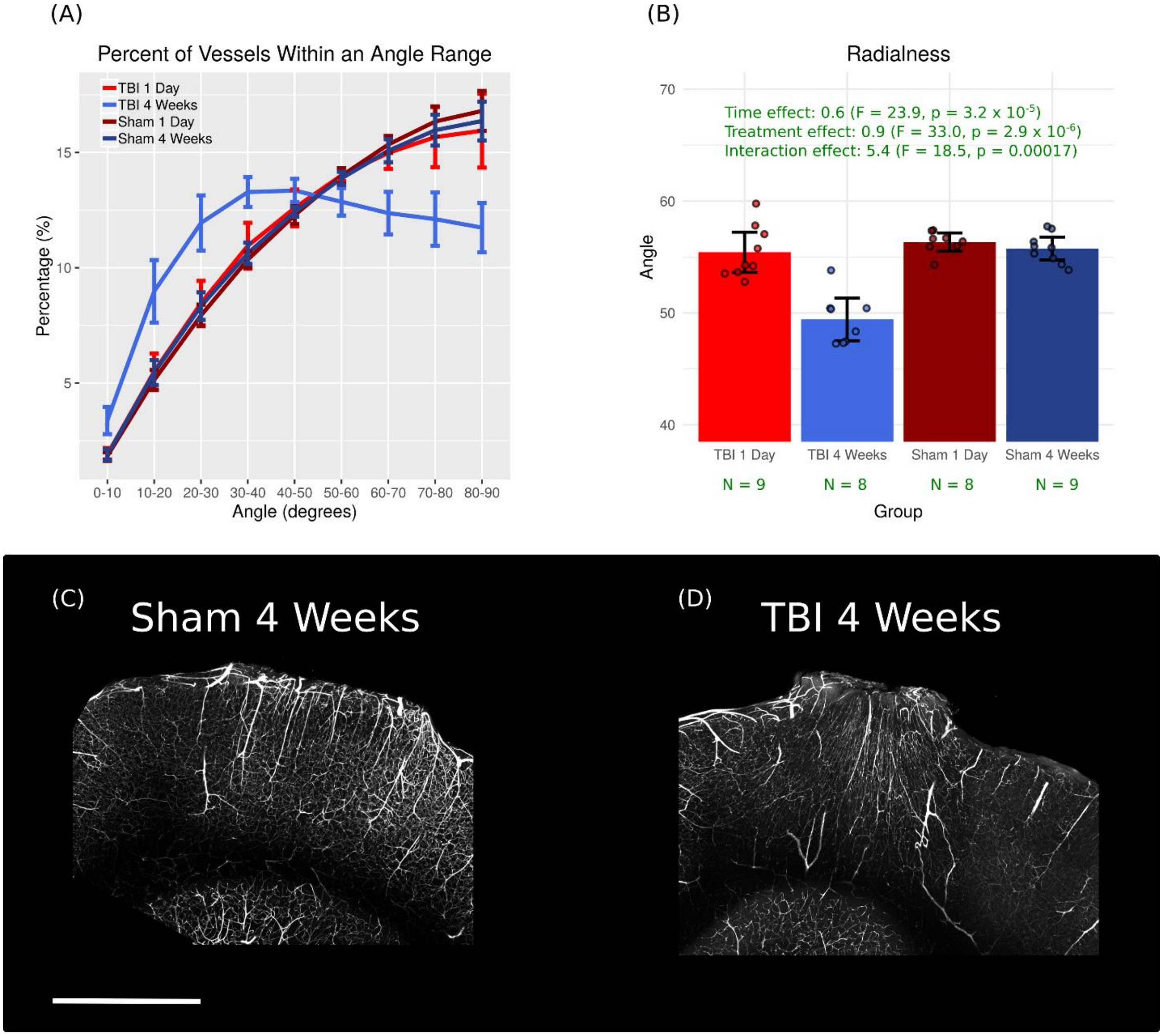

Figure 3.6. Quantification of the radial vascular architecture. (A) Mean percentage of vessels as a function of angle (B) Mean angle of vessels in injured cortex as a function of group (C) MIP through 200 µm of tissue in a Sham-4-Week mouse (D) MIP through 200 µm of tissue in TBI-4-Week mouse. Scale bar = 1 mm. Data points in A and B are the mean ± 95 % CI and N refers to the number of mice.

3.5 Discussion

3.5.1 Biological implications of results

We present a study of vascular architecture and function in a mouse TBI model via a novel methodology for integrating measurements of CBF and microvascular structure. Previous studies of fluid percussion injury in rats described vascular regrowth without concurrent blood flow recovery [22, 30]. Our study is consistent with this result and examines the vasculature in 3D to provide possible explanations for such findings. Through registration of ASL perfusion maps to STPT data, precise correlations between blood flow and vessel structure are obtained.

While vessel density recovered from TBI by 4 weeks, the vessel network possessed an abnormal radial pattern. It was interesting to note that these vessels, which are likely formed rapidly in the days following injury [87], retained many of the geometric and network properties, such as Murray's law scaling, that are observed in mature, uninjured vascular networks. Previous studies have also reported that the size of the injury core reduces with time in CCI [69], which could be due to this radial invasion of new vessels to deliver nutrients to the injured region. The association between this radial pattern and reduced blood flow suggests that this radial patterned network performs more poorly than those found in uninjured animals.

Rapid vessel loss at the 1-day time point has previously been reported in CCI [86] and fluid percussion injury [21]. CCI leads to loss of smaller branching vessels, with large vessels remaining [86]. We attribute vessel loss to endothelial cell death, and not just lack of FITC-gel perfusion, as vessel density in this study is determined by the number of endothelial fluorescent vessels. Similar to our study, others report loss of endothelial cells and increased endothelial apoptosis early post-TBI (1 – 3 days) [21, 88].

Although our data indicates that the most significant loss of vessels occurs in the TBI-1-Day group, Figure 3.4F suggests that the Sham-1-Day mice may also experience loss of vasculature, perhaps associated with edema. It has previously been reported that a sham surgery creates a lesion volume requiring about two weeks to subside in rats [214]. If present, there was no evidence in the present study that vessel loss associated with sham surgery was recovered at the 4-week timepoint. Future investigation of the vascular architecture in animals that have not undergone sham surgery could clarify this question.

There was an increase in vessel tortuosity 1-day post-injury, similar to Sangiorgi et al. [71] in the acute stage post-CCI. Tortuosity may be attributable to collapsed lumens or alterations in flow pressure [76], possibly caused by increased swelling and edema. Tortuosity increases overall resistance of the vascular network and could contribute to the reduced blood flow and impaired cerebrovascular reserve observed at 1-day post-injury. Radial patterns of newly formed vessels have been reported in a focal stroke model 6-weeks post-injury [111] and in a mouse CCI model at 7 days [87]. Brown et al. [111] noted that the formation of these vessels correlated temporally with the formation of scar tissue and a ’dimple’ in the cortex, suggesting that mechanical forces are involved in the production of a radial vascular network. Tissue deformation caused by impact produces a ‘gradient of angiogenic microenvironments’ [215], with VEGF concentration highest in the region of greatest deformation. Proliferation of cells in the direction of the gradient could cause formation of the radial pattern. This adaptation enables blood and oxygen to be delivered specifically to the injured region, as opposed to more evenly throughout the tissue which occurs with the more random vascular orientation observed in shams.

Factors beyond vascular architecture could also influence CBF. Hayward et al. [22] proposed that TBI damages endothelial cells, rendering them incapable of responding to situations requiring hyperemia. TBI also reduces α-SMA (alpha smooth muscle actin, the actin isoform most commonly expressed in vascular smooth-muscle cells) in cerebral arteries, which wrap around vessels and contribute to vasomotion and regional CBF flux [216, 217]. α-SMA loss may therefore be a potential cause of CBF reductions in trauma. Damaged endothelial cells may poorly conduct blood. In many of the TBI-1-Day mice, there were vessels that expressed the endothelial cell fluorescent marker but that the injected FITC gel did not reach (see Supplemental Figure 3.4). This suggests that these vessels may not be perfused in vivo. While this could be an effect of the perfusion methodology, as the gel viscosity does not match blood, a more likely explanation is that mechanical damage, increased cranial pressure, or vasoconstriction of proximal vessels has made these vessels ischemic. Angiogenesis could also lead to the formation of unperfused vessels; however, the time scale (1-day) and morphology observed was not consistent with newly formed vessel sprouts.

In addition to the potential arterial loss of smooth muscle cells, capillaries that lack pericytes often display leakage, dilation, hemorrhage, and reduced flow [106, 107, 108]. In TBI, pericytes migrate away from the vessel wall [109] and are often detached from vessels at least 5 days post-CCI injury [110]. It is possible that a number of these pericytes will remain detached from vessels several weeks later. This would contribute to low blood flow and impaired reactivity.

The positive correlation between rest CBF and diameter scaling coefficient demonstrate that successive branching diameters that decrease more slowly result in a larger CBF, since a larger magnitude coefficient is indicative of diameters decreasing more slowly with successive branching [213]. The poor correlation of scaling coefficient with hypercapnic CBF is possibly due to the fluorescent gel perfusions performed under anaesthetic in the resting state. Although ketamine (anaesthetic used for perfusion) and isoflurane (anaesthetic used for CBF measurements) are both vasodilators [218], hypercapnia under isoflurane exposes mice to an additional vasodilator, CO_2. In addition to dilating the vasculature, hypercapnia causes a more uniform distribution of vessel diameters and flow [219]. Since the ratio of diameters at a bifurcation drives the scaling coefficient, hypercapnia will affect this ratio, possibly explaining the low correlation. Alterations to 3D vascular structure are further seen in the cumulative distribution plots of Figure 3.5A, where both TBI groups show an inflection in the cumulative distribution at 8 µm, approximately at the diameter threshold below which vessels are predominantly capillaries.

Although 3D vascular structure contributes to CBF, vessel density still plays a role. There was a stronger correlation between CBF and vessel density under hypercapnia. This finding could be explained by vessel recruitment whereby the number of capillaries perfused by blood cells increases with stimuli such as increasing metabolic demand or in response to large increases in CBF such as with hypercapnia [220, 221]. Since more vessels are perfused under hypercapnia due to vasodilation, a greater proportion of the vessels imaged with STPT could contribute to CBF in this state and explain the stronger relationship between CBF and vessel density. Previous studies by Hayward et al. [22, 30] correlated only rest CBF with vessel density. At the acute time-point, they found a correlation between density and hippocampal CBF. However, despite an increase of vessel density at 2 weeks, there was a reduction in CBF. This acute correlation is likely due to loss of vessels, while newly formed vessels at later time points may remain un-perfused under resting conditions.

Vascular dysfunction and disruption likely explain the elevated COV, or blood flow variability, measured in TBI. COV increased in TBI close to the injury centre and diminished with distance (Figure 3.3E, F). Forbes et al. [222] also found increased flow variability at 24 hours in rat CCI. Edema, hemorrhage, and elevated intracranial pressure may compress some vessels, causing redistribution of capillary flows and increased flow heterogeneity [223]. Subarachnoid hemorrhage, a feature of CCI, may cause large vessel vasospasm and concurrent microvessel dilation [81]. We found a 7 % increase in capillary diameter in TBI vs. shams. A combination of redistributed flow, some shrinking vessels, enlarged capillaries, and low flow in regions of directly damaged vasculature and hemorrhage may contribute to the CBF heterogeneity observed.

Despite vessel loss at 1 day, our findings imply that tissue remains partially viable post-injury. Park et al. [21] showed that if an injury is sufficiently severe, the vasculature will not regrow weeks after TBI. The extravascular distance to the nearest microvessel was elevated 1-day post-TBI relative to other groups in our experiments. The mean extravascular distance in our study at 1 day was 47 µm, while normal synaptic structure is maintained if a dendrite is within 80 µm of a microvessel [7]. Many dendrites would be able to receive oxygen and nutrients from the vascular network since they are within the 80 µm limit. This would enable the tissue to regrow and repair to some extent, which was found in the TBI-4-Week mice. Tissue recovery will also partially depend on flow through the network, which remains reduced at 4-weeks post-TBI. Further experiments are needed to determine the status of dendrite and neuron function. However, recovery of vessel density and the absence of a necrotic cavity as per more severe CCI models [224] suggests the presence of at least partially viable tissue.

3.5.2 Technical notes

As the methodology used for vessel density measurements is novel, it is interesting to compare these observations with literature reports. Mean vessel length density at Sham-4-Weeks (858 mm^3) reported here is comparable to that obtained in Tsai et al. [6] from sucrose-cleared tissue slabs (880 mm/mm^3), Boero et al. [34] from thin sections (700 – 1200 mm/mm^3), and Lugo-Hernandez et al. [26] from whole brain microvascular reconstructions (922 mm/mm^3). Tsai et al. [6] report smaller capillary diameters at 3.5 – 4.0 µm, compared to a mean of 4.5 µm, despite usage of identical perfusion materials. This could be due to their quantifying the lumen diameter whereas the diameter measurement reported here include the vessel wall. These diameter differences likely explain the greater microvascular volume (1.45 % at Sham-4-Weeks vs. 1 % in Tsai et al [6]).

There are drawbacks to STPT. As an ex vivo technique, it necessitates design of a cross-sectional study. Unlike optical clearing where the tissue may be sectioned for histology following imaging, subsequent histological analysis is not possible with STPT. This prevents examination of relevant molecular and cellular-level processes beyond vasculature structure, such as presence of pericytes or smooth muscle cells, which may impact blood flow.

Ex vivo specimen preparation can also shrink whole brain volumes by up to 10 % [225]. Despite this shrinkage, it is likely similar across specimens and groups. Since good alignment was obtained via rigid body registration (see Figure 3.1), we do not view ex vivo shrinkage as a factor which impacts interpretation of results. Additionally, shrinkage varies across structures, with the brain stem and olfactory bulbs particularly vulnerable [225]. The cortex is relatively unaffected by perfusion fixation [225].

One factor which could impact interpretation of results is intracranial pressure (ICP). The protrusion of tissue through the craniotomy suggests that ICP is elevated following cortical impact, possibly affecting both tissue and microvessels. Elevated ICP can compress vessels, reduce flow, and distort vessel shapes. The observed protrusion of tissue through the craniotomy is consistent with elevated ICP following injury and likely contributes to the severity of vascular injury that is observed. In the context of the present study, this pronounced injury pattern is an advantage for examining the relationship between higher-level properties of vascular networks and cerebral perfusion. While the severity and timing of ICP changes have been reported to vary across different injury models [226], it is interesting to note that radial patterning similar to that reported here has previously been reported in both CCI [87] and focal stroke models [111].

High oxygen (100 %) and isoflurane (> 1 %) concentrations were used during surgery to induce TBI. Vasoparalysis (inability of vessels to constrict) potentially plays an important role in TBI progression. In patients with cerebral swelling, it may contribute to the rise in ICP and subsequent CBF impairment [227]. It is expected that vasoparalysis due to CCI and administration of vasoactive materials such as isoflurane or oxygen will affect the response to

TBI, even if these materials were only administered in higher concentrations during the TBI surgery. Nonetheless, since the same surgical procedures were performed on shams, it is expected that our findings vis-a-vis vascular changes and blood flow are still relevant.

Finally, while this study was conducted on both male and female mice, it was underpowered to examine sex differences. It was recently reported in a mouse CCI model that vessel network complexity and vessel numbers differed by sex post-injury [31]. No sex dependence was found in the present study: there was no statistical dependence of CBF on sex; both sexes demonstrated vascular loss at 1 day, followed by recovery to sham levels; and both sexes exhibited a radial vascular pattern at 4 weeks (data not shown).

3.6 Conclusions

Traumatic brain injury leads to widespread changes in the cerebral vascular system, whose functional and structural characteristics evolve over the days and weeks following injury. In the present study, by examining the functional characteristics of the cerebral circulation using non-invasive MRI measurements of cerebral blood flow and ex vivo measurements of the 3D structure of the blood vessels networks proximal to the injury, we found that these two aspects of the circulation were related in more complex ways than can be summarized as a simple magnitude of injury. Remodeled vessel networks following injury demonstrated a regular hierarchical structure that is characteristic of healthy vessel networks but did not recover the level of vascular function seen in sham treated animals. By other morphological measures, however, these remodeled networks were abnormal and possessed a characteristic radial network pattern. In developing future therapies to promote recovery of vascular function following injury, enhancing vessel growth may not be sufficient as the 3D architecture is an important factor in the overall performance of the remodeled network.

3.7 Supplemental Material

	TBI-1-Day	**TBI-4-Weeks**	**Sham-1-Day**	**Sham-4-Weeks**
Total surgeries	11	10	9	10
Ultrasound	10	9	9	9 (LCCA), 8 (RCCA)
ASL MRI	10	10	8	9
STPT	9	8	8	9
Attrition	1 mouse excluded because of operator error during surgery 1 mouse removed from STPT analysis due to low contrast-to-noise ratio and consequently poor image stitching	2 mice removed from STPT analysis due to operator error during sample preparation 1 mouse was not imaged using ultrasound	1 mouse died during preparation for MR imaging	1 mouse died during preparation for MR imaging 1 mouse was not imaged using ultrasound

Supplemental Table 3.1. **Allocation of mice.** Number of mice assigned to each group (TBI-1-Day, TBI-4-Weeks, Sham-1-Day, Sham-4-Weeks), along with numbers lost to attrition. A total of 40 mice were used for the study. LCCA represents the left common carotid artery, RCCA represents the right common carotid artery.

	CO_2 state (rest vs. hypercapnia)	**Time (1-day vs. 4-weeks)**	**Treatment (TBI vs. Sham)**	**Significant Interactions**
Cerebral Blood Flow	F = 88.8 P = 7.0×10^{-11} *	F = 0.5 p = 0.47	F = 14.8 p = 0.00052 *	State: Time F = 6.2 p = 0.018 *
Vessel Density	NA	F = 15.4 p = 0.00048 *	F = 28.2 p = 9.6×10^{-6} *	Time: Treatment F = 9.1 p = 0.0052 *
Capillary Diameter	NA	F = 2.4 p = 0.13	F = 11.9 p = 0.0017 *	Time: Treatment F = 0.7 p = 0.41
Microvascular Volume	NA	F = 21.3 p = 7.0×10^{-5} *	F = 9.7 p = 0.0041 *	Time: Treatment F = 7.2 p = 0.012 *
Extravascular Distance	NA	F = 5.2 p = 0.031 *	F = 18.0 p = 0.00020 *	Time: Treatment F = 7.2 p = 0.012 *
Scaling Coefficient	NA	F = 3.9 p = 0.058	F = 1.3 p = 0.27	Time: Treatment F = 1.1 p = 0.31
Radialness	NA	F = 23.9 p = 3.2×10^{-5} *	F = 33.0 p = 2.9×10^{-6} *	Time: Treatment F = 18.5 p = 0.00017 *

Supplemental Table 3.2. Summary statistics. * $p < 0.05$.

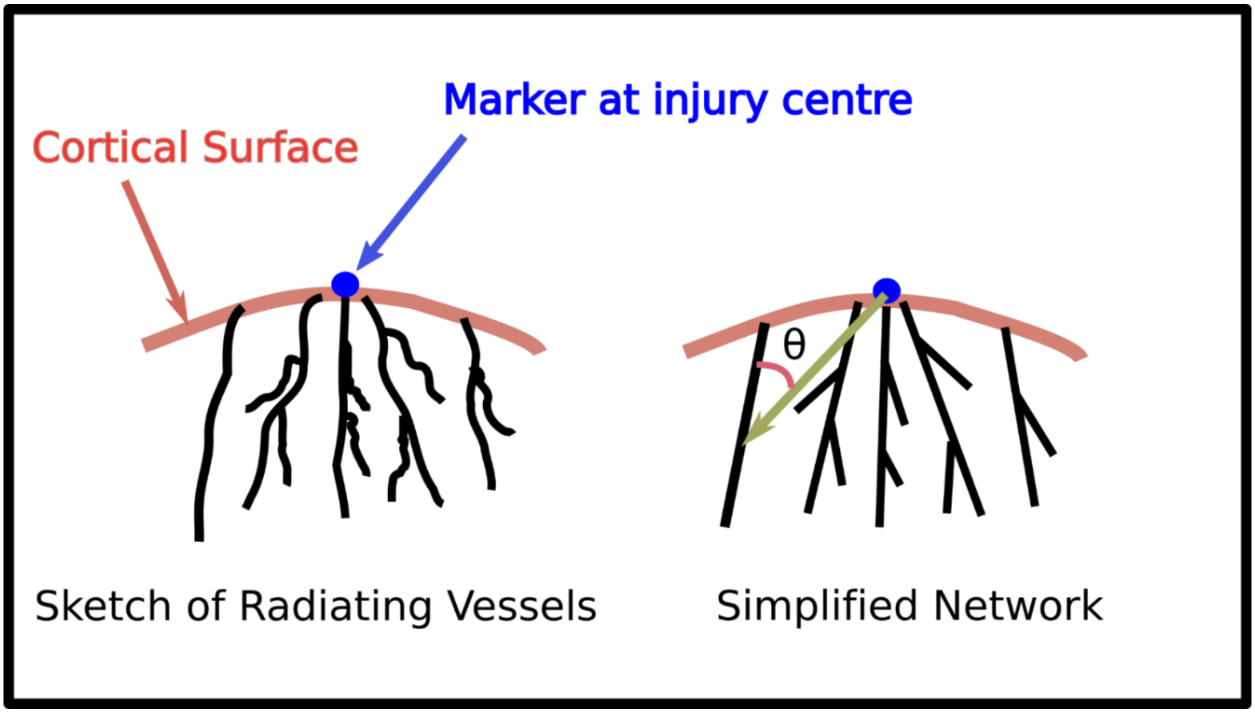

Supplemental Figure 3.1. Diagram explaining calculation of ‘radialness’. A (digital) marker was placed at the centre of the injury on the cortical surface, in the middle of the craniotomy site. Vessels (shown in black on the left) were approximated as straight lines in a simplified network (right figure). For each vessel within the injury core, a line (gold, right) was drawn from the marker to the centre of the vessel, approximated as the midpoint of the line. The angle between the straight vessel and the gold line was calculed (θ in the diagram). The average angle was obtained by averaging the θ calculated for each vessel. This mean θ is the metric ‘radialness’.

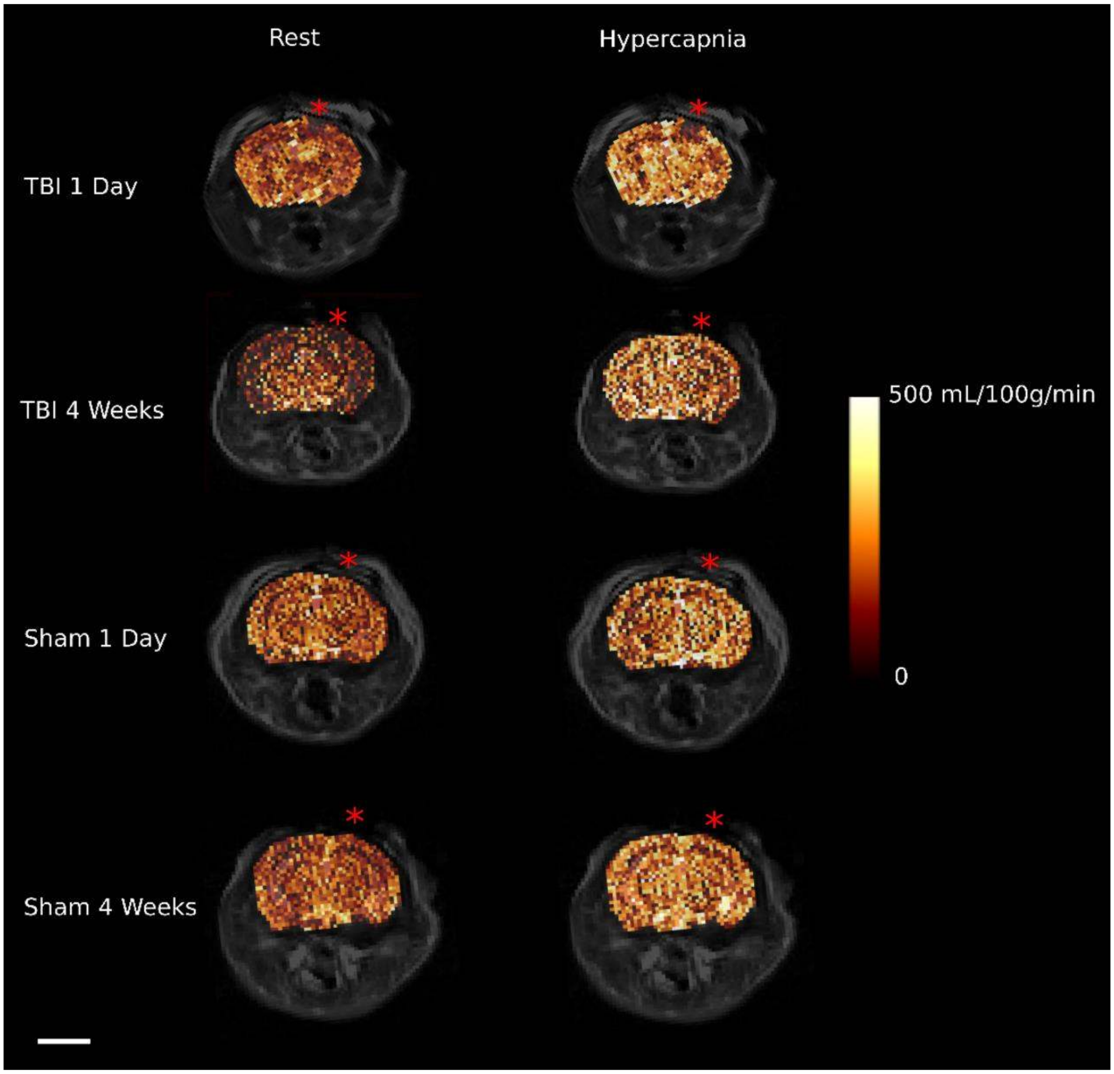

Supplemental Figure 3.2. **Representative CBF maps from each group.** Representative rest and hypercapnic CBF maps, overlaid on the control (T_2-weighted) baseline ASL image. Images are obtained by averaging multiple scans. Red stars indicate the ipsilateral cortex. Scale bar (lower left) = 4 mm.

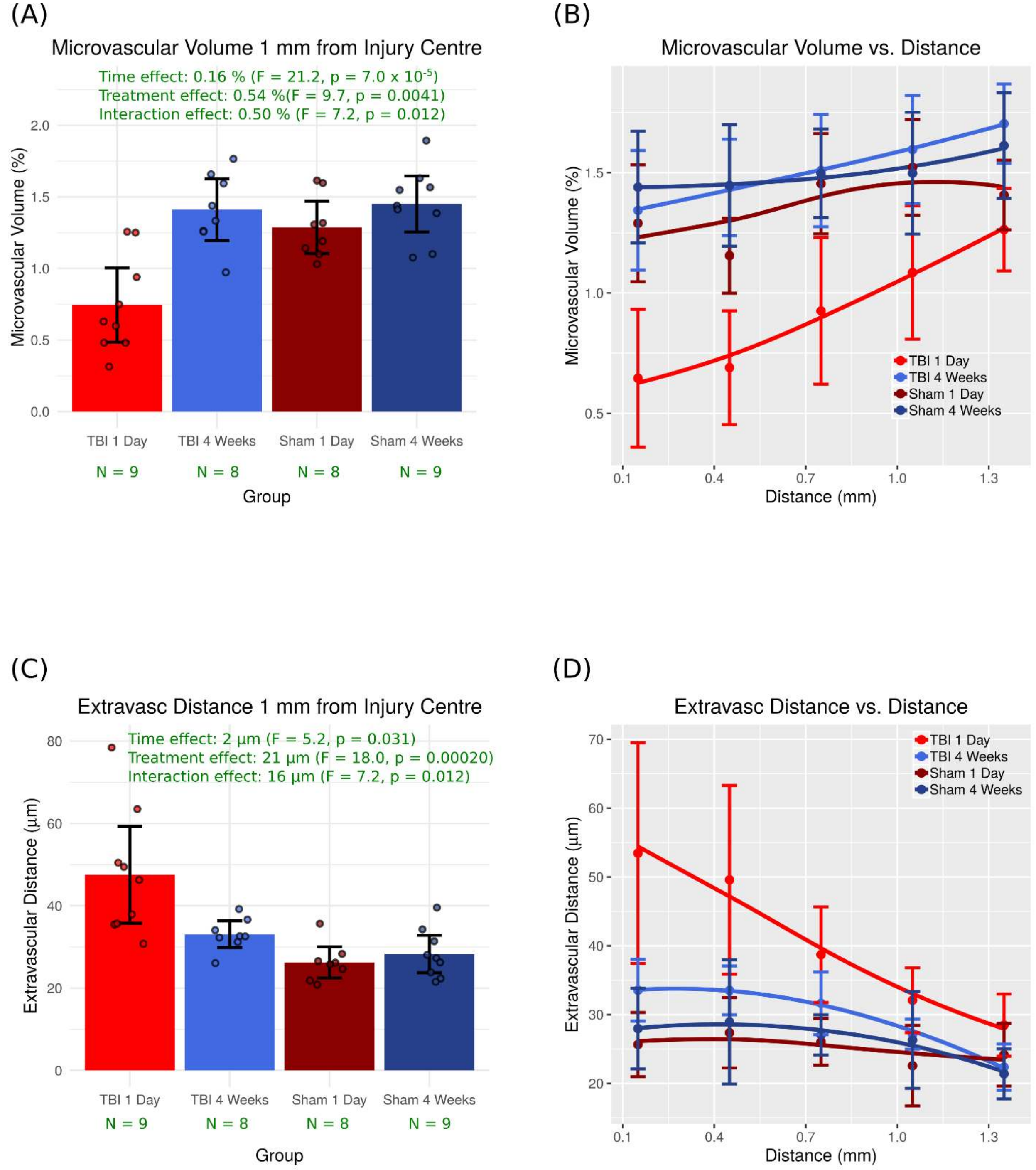

Supplemental Figure 3.3. Analysis of vascular volume and extravascular distance to the nearest vessel. (A) Mean vascular volume (B) Vascular volume as a function of distance from the injury centre (C) Mean extravascular distance to the nearest microvessel (D) Extravascular distance to the nearest microvessel as a function of distance from the injury centre. Data points are the mean ± 95 % CI, N refers to the number of mice, and data in B and D was fit using Loess regression.

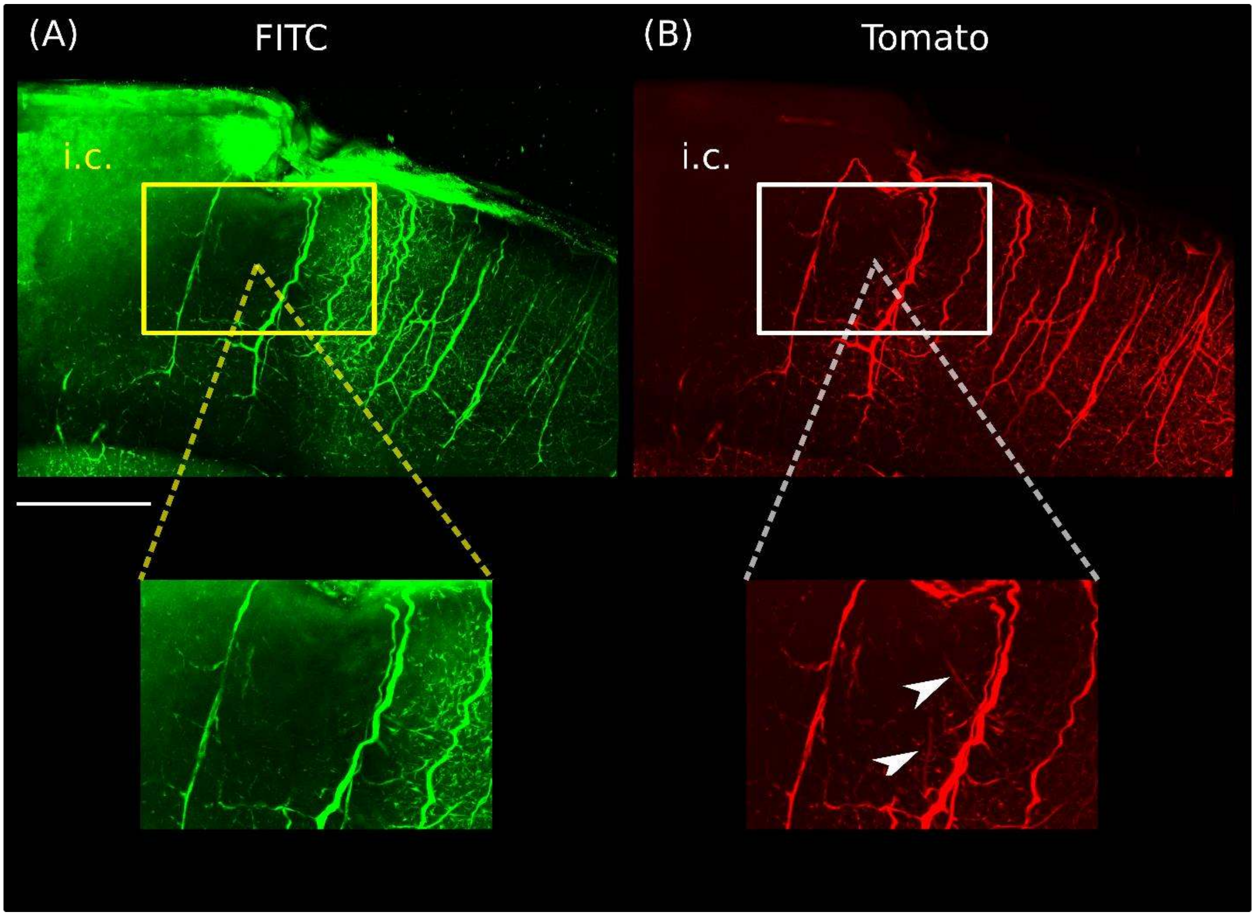

Supplemental Figure 3.4. Some endothelial fluorescent vessels remain unperfused by the FITC-gel 1-day post-TBI. (A) MIP (700 µm tissue thickness) through STPT data for a TBI-1-Day mouse showing the FITC fluorescence from the perfused gelatin detected following spectral demixing. (B) MIP of the same tissue region as A demonstrating tomato fluorescence. i.c. represents the injury core region. The boxes in A and B show the vasculature in the penumbra region surrounding the core. While a number of tomato-fluorescent vessels are perfused within the penumbra, others are not successfully perfused (see white arrows in inset from tomato image). Scale bar = 0.5 mm.

Chapter 4

Non-invasive Ultrasound Detection of Cerebrovascular Changes in a Mouse Model of TBI

4.1 Foreword

At the time of completion of this thesis, the work in this chapter was not published in a peer-reviewed journal.

4.2 Introduction

Ultrasound studies of traumatic brain injury (TBI) in humans have highlighted abnormalities in cerebral blood flow and vascular function. These abnormalities include impaired cerebrovascular reactivity [150, 151, 228], hypo- or hyper-perfusion [152], and alterations in pulsatility index (PI) of the middle cerebral artery [154, 155, 156, 157]. PI is often interpreted as an indicator of vascular resistance; however, it is not highly specific to changes in vascular architecture, since it is influenced by physiological parameters such as heart rate and perfusion pressure [157].

Our group has recently evaluated cerebrovascular impedance and wave reflection in the left common carotid artery of the adult mouse using high-frequency ultrasound [4]. By demonstrating changes in reflection in mice exposed to CO_2, a vasodilator, we established that wave reflection analysis could detect alterations in cerebral microvascular tone [4]. This non-invasive ultrasound methodology has the potential to aid the assessment of vascular pathology in TBI populations, where the vasculature undergoes significant damage and regrowth in trauma [21, 199].

In the present study, we used high-frequency ultrasound to measure the vessel area and Doppler blood flow waveforms to calculate input impedance and reflection in the common carotid arteries of mice exposed to TBI. We demonstrate that wave reflection metrics are sensitive to cerebrovascular changes induced by TBI. In addition, we show that input impedance modulus and phase may be used to distinguish mice as having received a TBI or sham surgery.

4.3 Materials and Methods

4.3.1 Animals and surgery

A total of 40 (21 male, 19 female, mean weight 24.6 g (CI: 23.4 – 25.8) Cre x tdTomato mice, C57BL/6 background) were used and randomly assigned to one of four groups: TBI-1-Day (TBI mice evaluated 1-day post-injury), TBI-4-Weeks (TBI mice evaluated 4-weeks post-injury), Sham-1-Day (Sham mice evaluated 1-day post-surgery), and Sham-4-Weeks (Sham mice evaluated 4-weeks post-surgery). TBI mice received a controlled cortical impact (CCI), while shams underwent craniotomy without impact. Mice were allowed to recover 24 hours or 4 weeks post-injury. The mice express a variant of red fluorescent protein on endothelial cells under the control of the Tie2 promoter [203] and 36 of the mice were included in a previous study [199]. The ultrasound imaging was performed prior to the other experimental assays (Arterial Spin Labeling MRI, Serial Two-Photon Tomography) detailed in [199]. Four mice were only imaged using ultrasound (three Sham-4-Weeks and one Sham-1-Day). One TBI-1-Day mouse was excluded from the entire study because of operator error during surgery and one RCCA data set from a Sham-4-Week mouse was excluded due to low SNR and inability to trace the M-mode data.

The surgery was previously described in detail [199]. Briefly, mice were anaesthetized in isoflurane (5 % induction, 1.5 – 2 % maintenance) and stabilized in a stereotaxic frame. A craniotomy of approximately 2.2 mm diameter was drilled over the left hemisphere, centred at 1.5 mm posterior to bregma and 1.7 mm lateral to the midline. A CCI was delivered with a 1.5 mm diameter tip, 1 mm depth, 2 m/s speed, and 200 ms dwell time. The craniotomy was sealed with a glass coverslip and the skin sutured. Identical procedures were performed for shams, without the impact. Animal experiments were approved by the Animal Care Committee at The Centre for Phenogenomics. They were conducted in accordance with the Canadian Council on Animal Care's guide to the Care and Use of Experimental Animals and complied with the ARRIVE guidelines.

4.3.2 Ultrasound imaging

Mice were anaesthetized in isoflurane (4 – 5 % induction, 2 % maintenance) in 21 % O_2 (Medical Air). They were placed on a temperature-controlled platform to maintain body temperature at 36 – 37 ^{o}C. Hair from the throat and chest were removed with Nair prior to contact with the ultrasound transducer. Heart rate and respiration rate were recorded throughout the imaging session. In vivo ultrasound imaging was performed on the left and right common carotid arteries (LCCA and RCCA respectively) (~ 3 mm proximal to bifurcation) with a 30 MHz transducer on a high-frequency ultrasound imaging system (Vevo 2100, VisualSonics, Toronto, Canada). M-mode recordings for carotid diameter measurements were made with the ultrasound beam perpendicular to the vessel. For pulsed Doppler velocity spectra, all measurements were acquired at an angle between the beam direction and vessel axis less than 60^o.

4.3.3 Image processing and data analysis

The data processing procedure was previously described in Macgowan et al. (2015) [4]. M-mode and Doppler data were analyzed offline with Python. The near and far walls were automatically traced in the M-mode images based on peak wall intensity. The start of each waveform in the cardiac cycle was manually labeled at the start of systole. An average diameter waveform for each mouse was calculated by averaging the traced waveforms over all cardiac cycles (Figure 4.1A). Individual waveforms that were poorly traced were manually labeled and removed. Diameter was converted to area by assuming the carotid artery comprised a circular cross section.

A similar procedure was repeated for the Doppler velocity spectra (Figure 4.1B). The maximum envelope was traced following specification of an upper and lower velocity bound. The final velocity spectra were obtained by dividing the values at each point on the traced envelope by two to approximate the centroid, assuming parabolic flow. An average flow waveform was obtained through multiplying the mean area by velocity waveform. Mean flow was calculated as the area under the curve of the resultant waveform. Pulsatility index (PI) was calculated as the difference between the maximum and minimum velocities, divided by the mean velocity of the average traced Doppler spectrum over the cardiac cycle.

Pulse wave velocity (PWV) was calculated from a plot of the relative change in flow versus area (QA plot) (Figure 4.1C). As per Rahman et al. [229], a line was fit using total least squares to 20 – 80 % of the maximum systolic flow region of the QA loop, assumed to be reflection-free [143]. The slope of this line approximates the PWV. The measured flow waveforms were decomposed into forward and reflected wave components as described in Macgowan et al. [4]. Reflection was defined in the frequency domain as the complex value ratio between the frequency spectra of the reflected to forward waves. Reflection was summarized at each harmonic as the magnitude of the reflection coefficient at the given frequency.

The input impedance, $Z_{in}(\omega)$, was defined according to the formula [4]:

$$Z_{in}(\omega > 0) = \frac{\rho . PWV^2}{\bar{a}} \frac{A_m(\omega)}{Q_m(\omega)}$$

where ω is the frequency in units of harmonics of the fundamental frequency, ρ is blood density (1.06 g/mL) [4], $\bar{a}$ is the average vessel area over the cardiac cycle, $A_m(\omega)$ is the measured area waveform, and $Q_m(\omega)$ is the measured flow waveform.

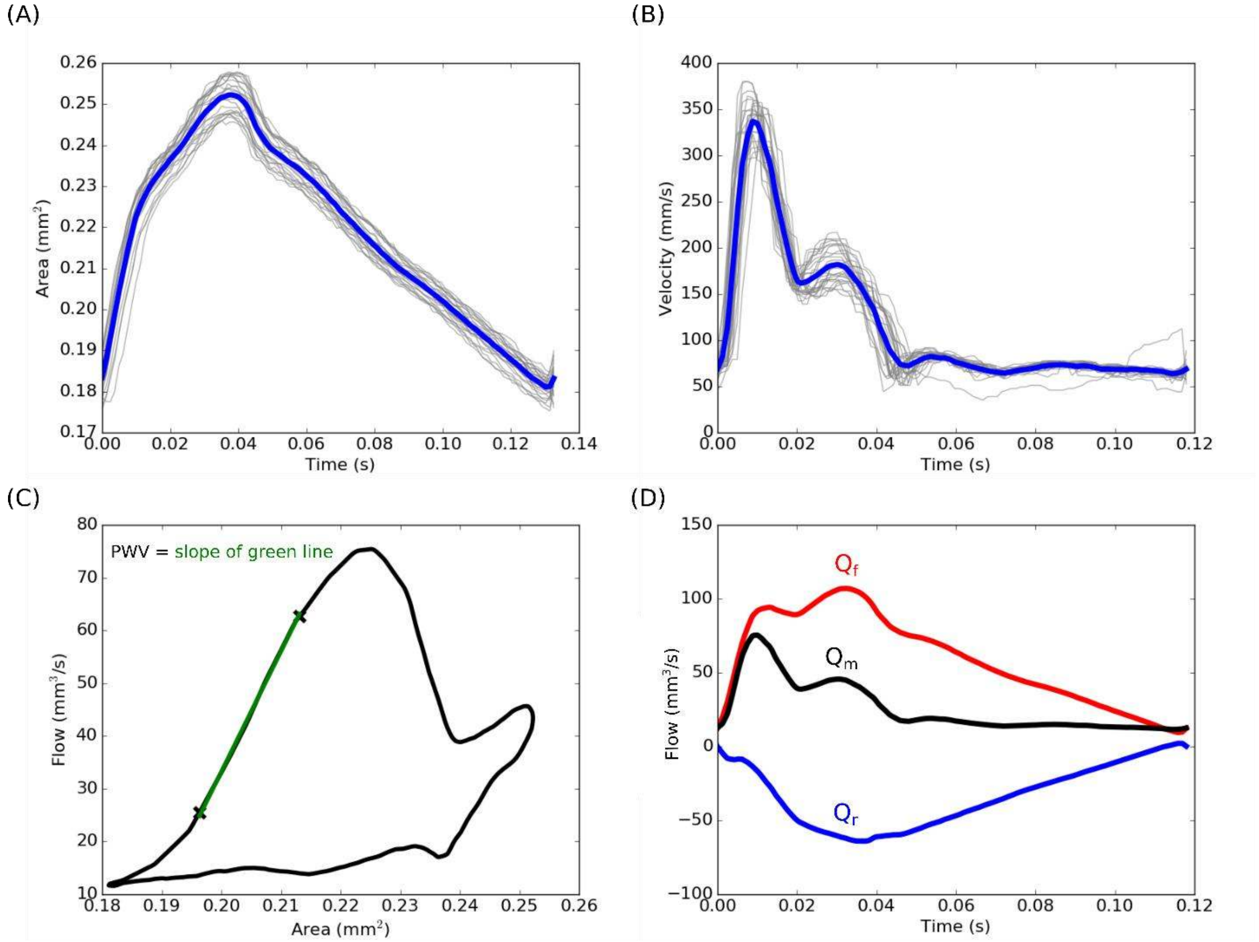

Figure 4.1. Representative data from the left common carotid artery (A) M-mode data over a cardiac cycle converted to area from the measured diameter; and (B) Doppler velocity data. In (A) and (B), waveforms from each cardiac cycle (*grey*) are aligned and averaged to produce a single waveform (*blue*). The flow vs area trace in (C) is used to calculate the pulse wave velocity. Using the pulse wave velocity, the measured flow waveform (Q_m, black) in (D) is decomposed into a forward waveform (Q_f, red) and reflected waveform (Q_r, blue).

4.3.4 Statistical analysis

Statistical analysis was performed in R (http://www.r-project.org/). Data was summarized as mean ± 95 % confidence intervals. To determine the effect of time (1-day vs. 4-weeks), side (LCCA vs. RCCA), and treatment (TBI vs. Sham) on a variable of interest (ie. PI or input impedance modulus/phase), a three-way ANOVA was performed on a linear mixed-effects model with mouse ID as the random effect. Statistical significance was defined as $p < 0.05$. To assess the correlation between variables, such as impedance and PI, linear regression was performed separately in the LCCA and RCCA, following merging of data from all groups. R^2 and p-value were used to assess the strength and significance of correlations respectively.

To determine whether hemodynamic parameters, such as impedance, could identify whether a mouse received a sham surgery or TBI, linear discriminant analysis (LDA) was performed [230]. LDA classifiers were constructed with impedance modulus and phase as predictors, and PI and artery diameter as predictors. Artery diameter was chosen in combination with PI because it parallels impedance phase as a predictor, since phase has been demonstrated to be related to diameter [231]. A receiver operating characteristics (ROC) curve was calculated for each classifier separately in the LCCA and RCCA for data from all mice, as well as the area under the curve (AUC). Confidence intervals for the AUC values and p-values for comparing mean AUC values were calculated with the pROC package in R [232]. The error rate of the classifier was estimated with k-fold cross-validation, with $k = 3$ [230]. Each fold/group (three total) contained an equal number of sham and TBI mice. Data was trained on 2/3 folds, and the error rate calculated on the test (hold-out) fold. Each fold was used once as a hold out, with the other two as the training data. The error rate was calculated as an average of the error rate from the three folds. To obtain a confidence interval on this estimated error rate, this procedure was repeated 50 times with random re-sampling of the order of the data (repeated k-fold cross-validation), resulting in a different training and test set each time. The results were averaged to obtain an overall mean error rate. A similar procedure was performed to obtain a mean estimate and confidence interval for area under the receiver operating characteristics (ROC) curve. For each hold-out fold, a ROC curve and a corresponding area under the curve (AUC) was calculated using the other two folds as training data. For each re-sampling (50 total re-samplings), a mean AUC from the three folds was calculated. The overall mean AUC is the mean AUC from each re-sampling.

4.4 Results

4.4.1 Pulse wave velocity is reduced in TBI and does not recover by 4 weeks post-surgery

Blood velocity, flow, and pulse wave velocity in the carotid artery on the ipsilateral (LCCA) and contralateral (RCCA) sides are shown in Figure 4.2. We summarize the most significant comparisons among these variables in the text below and provide a complete summary of this analysis in Table 4.1. Mean blood velocity was elevated at 1-day following injury as compared to the 4-week timepoint (F = 11.5, p = 0.0017) whereas mean blood flow, which incorporates measurements of velocity and diameter, was greater on the contralateral (right) side (F = 8.3, p = 0.0068) and showed a similar time dependence (F = 20.0, p = 7.9 x 10^{-5}). In contrast, pulse wave velocity was decreased in TBI relative to shams (F = 7.3, p = 0.011) and did not recover at the 4-week timepoint nor differ significantly between sides. Modeling heart rate with respect to time and treatment, there was a trend to decreased heart rate in TBI animals (459 (CI: 428 – 490) bpm vs. 501 (CI: 471 – 531) bpm) (F = 3.6, p = 0.067).

Figure 4.3 shows the decomposition of the flow waveforms into their forward and reflected components for each mouse. The overall shape of the curves was similar between groups. In addition to the increased carotid artery blood flow at 1-day, in the LCCA (ipsilateral side) there was a higher variation in the forward and reflected waveforms at this time point relative to the other groups, particularly for the TBI-1-Day animals.

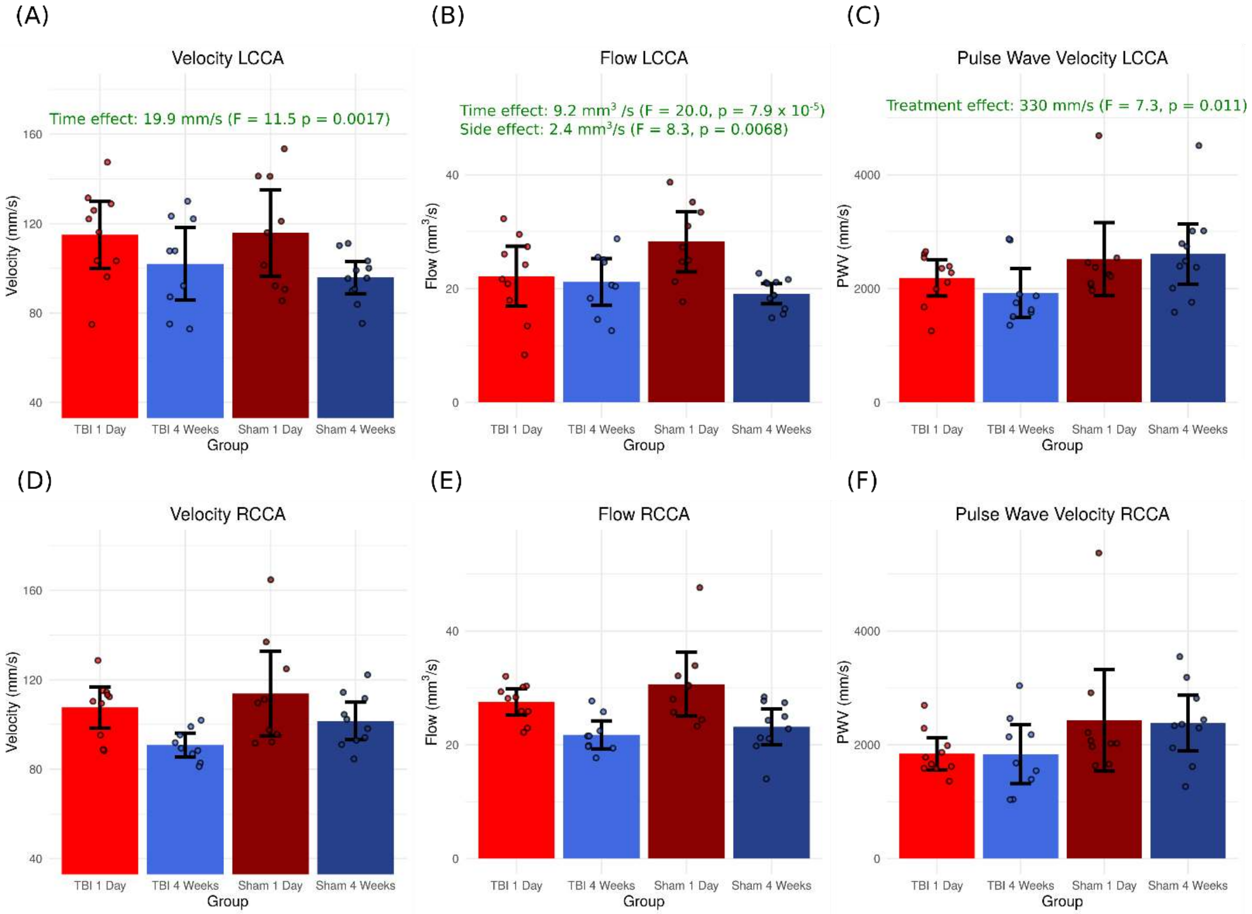

Figure 4.2. Hemodynamic parameters. (A) and (D) Carotid artery blood velocity (LCCA (ipsilateral) and RCCA (contralateral) respectively); (B) and (E) Blood flow (LCCA and RCCA respectively); (C) and (F) Pulse wave velocity (LCCA and RCCA respectively). Data points are mean ± 95 % confidence interval. Number of mice (LCCA/RCCA) = 10/10 TBI-1-Day, 9/9 TBI-4-Weeks, 9/9 Sham-1-Day, 11/10 Sham-4-Weeks.

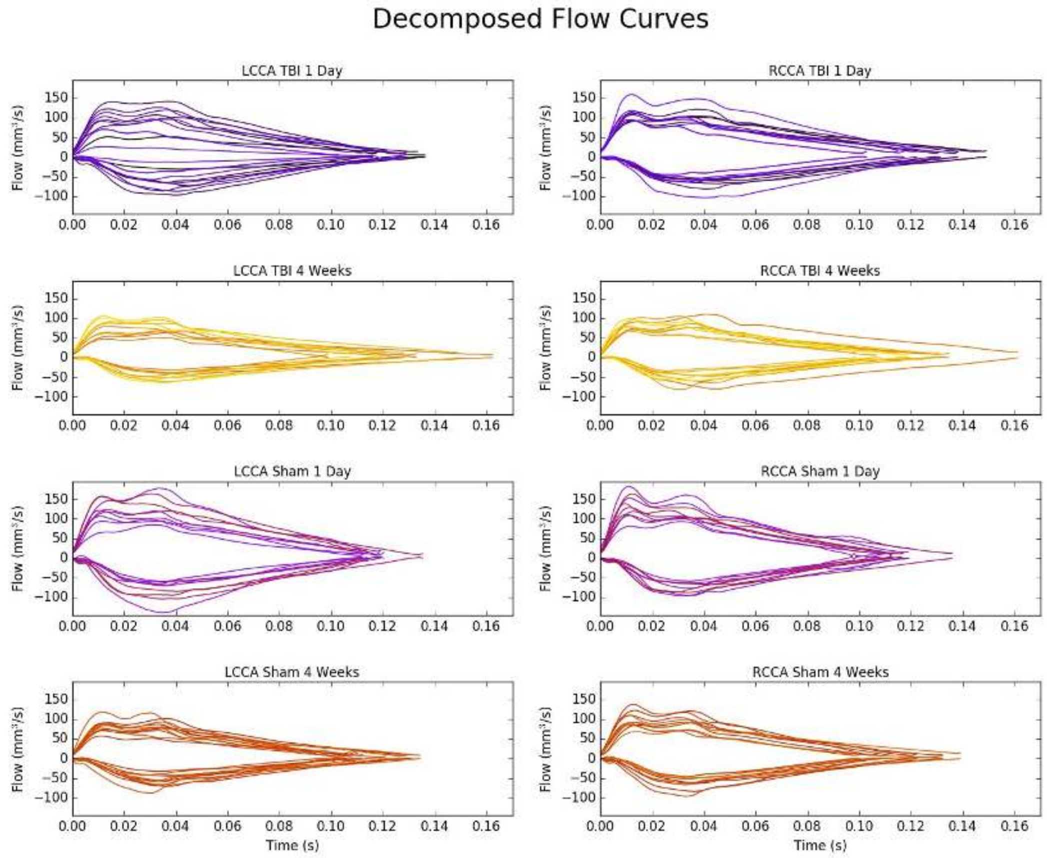

Figure 4.3. Decomposition of measured flow into forward and reflected flow waves. Curves are colored according to mouse ID. Note the greater variation in the flow waveforms on the left side (LCCA), ipsilateral to the injury, 1-day post impact.

	Time	**Side**	**Treatment**	**Significant Interactions**
Diameter	$p = 0.063$	Effect size: 0.026 mm CI: - 0.011 – 0.063 mm $p = 1.9 \times 10^{-5}$ Diameter reduced in LCCA.	$p = 0.24$	*Time: Treatment* Effect size: 0.072 mm CI: 0.013 – 0.131 mm $p = 0.0498$ Diameter reduced in TBI-1-Day relative to Sham-1-Day
Velocity	Effect size: 19.9 mm/s CI: 4.2 – 35.6 mm/s $p = 0.0017$ Velocity increased at 1-day.	$p = 0.32$	$p = 0.54$	NA
Flow	Effect size: 9.2 mm^3/s CI: 4.5 – 13.9 mm^3/s $p = 7.9 \times 10^{-5}$ Flow increased at 1-day relative to 4-weeks.	Effect size: 2.4 mm^3/s CI: -2.1 – 6.9 mm^3/s $p = 0.0068$ Flow decreased in LCCA.	$p = 0.11$	NA
Pulse Wave Velocity	$p = 0.97$	$p = 0.13$	Effect size: 330 mm/s CI: -330 – 990 mm/s $p = 0.011$ PWV reduced in TBI.	NA
Pulsatility Index	$p = 0.93$	Effect size: 0.28 CI: 0.03 – 0.53 $p = 0.0026$ PI reduced in LCCA.	Effect size: 0.08 CI: -0.25 – 0.41 $p = 0.0084$ PI reduced in TBI.	NA
Reflection Coefficient	$p = 0.83$	$p = 0.43$	$p = 0.065$	*Side: Treatment* Effect size: 0.10 CI: -0.25 – 0.45 $p = 0.039$ Reflection coefficient reduced in TBI in LCCA.
Z_{in} Modulus	$p = 0.65$	Effect size: 1.8 $[g/(s \times cm^4)].10^5$ CI: 0.2 – 3.4 $[g/(s \times cm^4)].10^5$ $p = 0.0012$ Impedance modulus increased in LCCA.	$p = 0.091$	NA
Z_{in} Phase	$p = 0.84$	$p = 0.22$	$p = 0.072$	*Side: Treatment* Effect size: 0.10 CI: 0.03 – 0.17 $p = 0.0032$ Impedance phase increased in the TBI in LCCA.
Wall Thickness	$p = 0.31$	$p = 0.85$	$p = 0.39$	NA

Table 4.1. **Summary statistics.** Statistics are calculated via ANOVA for main effects for variables modeled as a three-way interaction between time, side, and treatment. Mouse ID is the random effect. Effect sizes are shown for the significant terms ($p < 0.05$), along with their confidence intervals.

4.4.2 Impedance phase differs from shams on the ipsilateral (left) side

Several metrics of vascular resistance are plotted in Figure 4.4. Pulsatility index (PI) was decreased in TBI relative to shams (F = 7.8, p = 0.0084) and more so for both groups on the ipsilateral side (F = 10.6, p = 0.0026). In contrast, the magnitude of the 1st harmonic of the input impedance (Z_{in}) was increase on the ipsilateral side (F = 12.6, p = 0.0012). Examining the phase of the impedance, phase was increased (less negative) in TBI animals on the ipsilateral side and did not recover at the 4-week time point (F = 10.1, p = 0.0032).

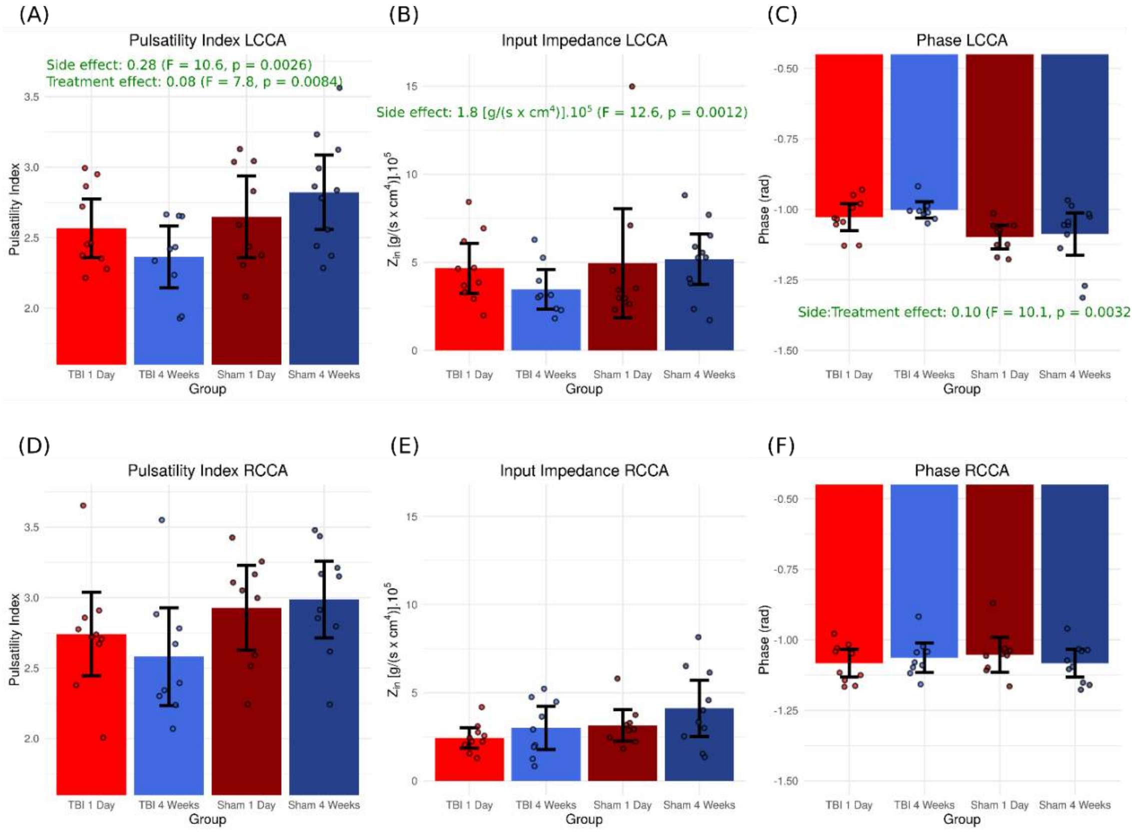

Figure 4.4. Ultrasound metrics of vascular resistance. (A) and (D) Pulsatility index (LCCA and RCCA respectively). (B) and (E) Input impedance modulus 1st harmonic (LCCA and RCCA respectively). (C) and (F) Input impedance phase 1st harmonic. Bar plots are mean ± 95 % confidence interval. Number of mice (LCCA/RCCA): 10/10 TBI-1-Day, 9/9 TBI-4-Weeks, 9/9 Sham-1-Day, 11/10 Sham-4-Weeks.

Figure 4.5 plots the correlation between $|Z_{in}|$ and PI ipsilaterally (LCCA) and contralaterally (RCCA). Although $|Z_{in}|$ and PI were positively correlated in the RCCA ($R^2 = 0.19$, $p = 0.0064$), there was no correlation in the LCCA (ipsilateral side) ($R^2 = 0.0021$, $p = 0.78$).

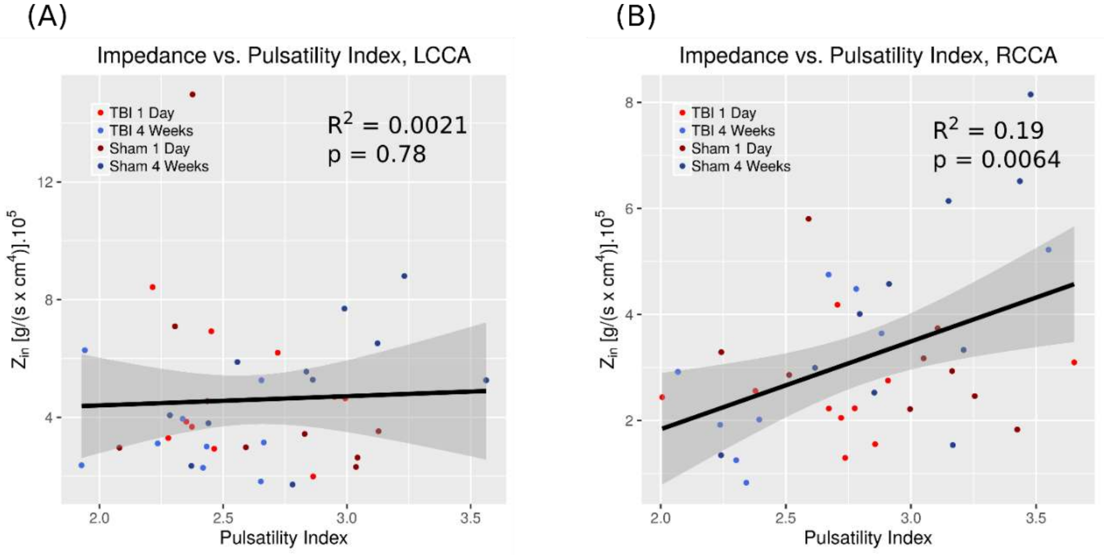

Figure 4.5. Correlating input impedance 1st harmonic with pulsatility index. (A) LCCA and (B) RCCA. Each data point represents an individual mouse. Grey bands are the 95 % confidence interval.

4.4.3 Input impedance modulus and phase discriminate between TBI and sham animals

Figure 4.6 plots the results from the linear discriminant analysis (LDA). Figures 4.6A (LCCA) and 4.6C (RCCA) show the data classified as sham or TBI using LDA with impedance and phase as predictors. On the ipsilateral side, LDA correctly classifies shams for 14/20 data points (30 % false positive rate), and correctly classifies TBI for 15/19 data points (79 % true positive rate). To assess discrimination quality, an area under the curve (AUC) for the receiver operating characteristic (ROC) curve was calculated for impedance/phase as predictors and compared to the AUC with PI/diameter as predictors. In the LCCA, the AUC was 0.792 (CI: 0.648 – 0.936) for the impedance modulus/phase data and 0.716 (CI: 0.553 – 0.879) for the PI/diameter data. There was no statistical difference between the LCCA AUCs (p = 0.43). In the RCCA, shams are correctly classified on 10/19 instances (47 % false positive rate), while TBI animals are correctly classified on 14/19 instances (74 % true positive rate). The AUC for the ROC curve was 0.662 (CI: 0.485 – 0.839) for the impedance modulus/phase data and 0.704 (CI: 0.526 – 0.882) for the PI/diameter data. There was no statistical difference between the AUCs (p = 0.71).

For repeated k-fold cross validation (k = 3, N = 50) on the LCCA data, with impedance/phase as predictors, there is an average error rate for the LCCA of 0.303 (CI: 0.289 – 0.317), and a mean AUC of 0.758 (CI: 0.747 – 0.769). The error rate with PI and diameter as predictors is 0.389 (CI: 0.379 – 0.0.399) and mean AUC is 0.685 (CI: 0.676 – 0.694).

For the RCCA data, the error rate with impedance/phase as predictors is 0.463 (CI: 0.444 – 0.483); the mean AUC is 0.580 (CI: 0.560 – 0.600). With PI/diameter as predictors, the error rate is 0.384 (CI: 0.0.368 – 0.400) and the mean AUC is 0.636 (CI: 0.617 – 0.655).

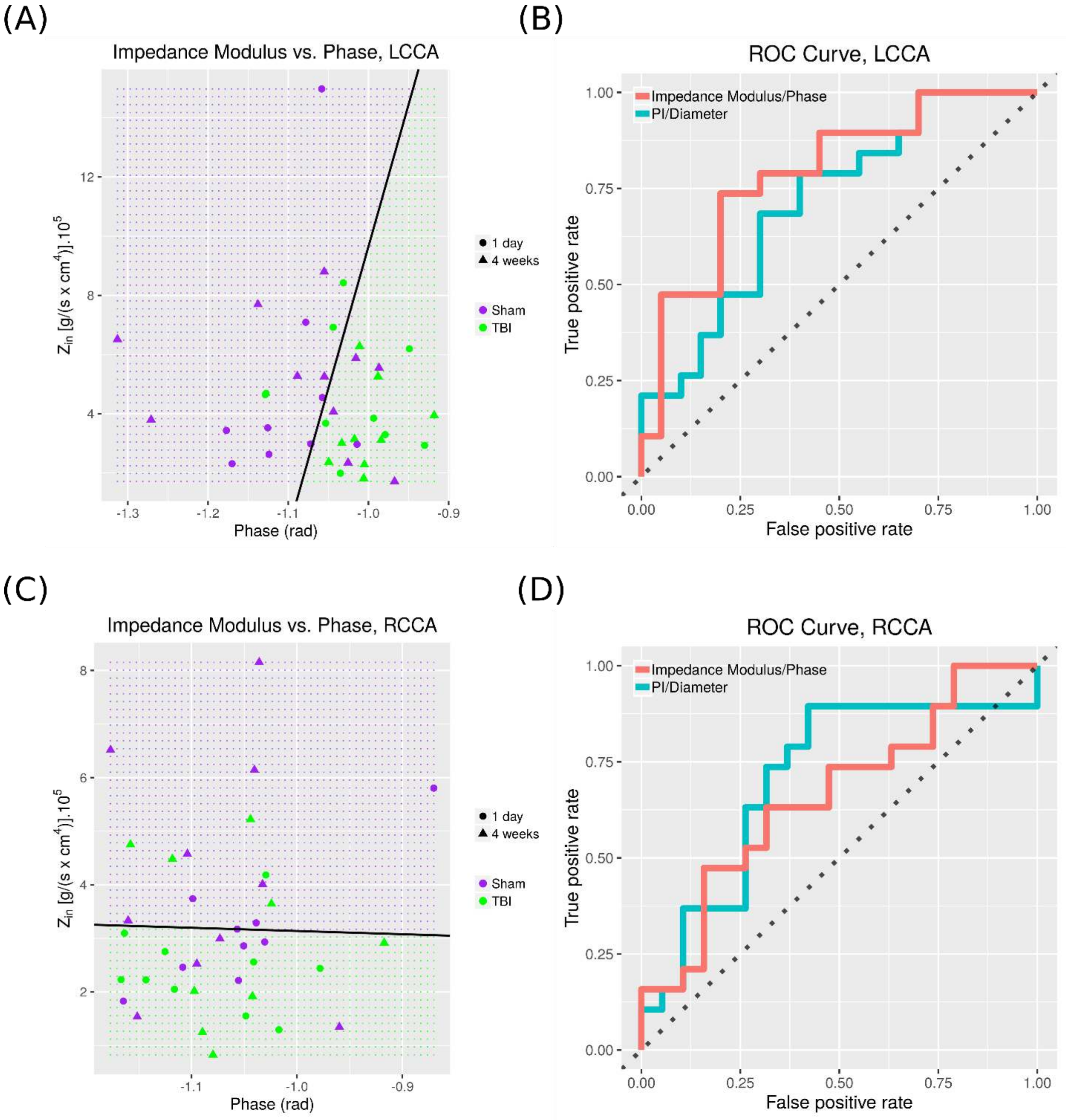

Figure 4.6. Linear discriminant analysis for classification of TBI/sham mice with impedance modulus and phase as predictors. (A) and (C) Each data point represents an individual mouse in the LCCA and RCCA respectively. (B) and (D) Receiver operating characteristic (ROC) curves for discriminating between TBI and Sham, with either impedance/phase as predictors, or PI/diameter as predictors.

4.5 Discussion

4.5.1 Biological interpretation of results

Ultrasound was used to non-invasively evaluate impedance and wave reflection in mice exposed to TBI. These revealed a range of hemodynamics changes induced by TBI including reduction of the PI and PWV bilaterally and less negative impedance phase ipsilaterally without contralateral changes. As these changes have potential to be used as biomarkers of vascular injury, we sought to compare these different metrics.

Whereas PI has the advantage of being more easily measured, input impedance is proposed to be more specific to remodeling of the downstream vascular bed as it depends on features such as viscoelastic properties of the vessel walls, vessel compliance, and variation in cross-sectional area at the bifurcations [233]. Although PI increases with cerebrovascular resistance and arterial compliance, it also increases with heart rate and the arterial blood pressure pulse amplitude, and is inversely proportional to the cerebral perfusion pressure [157]. Due to the dependence of PI on multiple factors, this could possibly explain the correlation between PI and impedance modulus contralaterally but not ipsilaterally. For example, decreased cerebral perfusion pressure may counteract a reduction in PI caused by vasodilation and consequent reduced resistance.

Arterial blood pressure is reduced acutely post-CCI [234, 235], and possibly contributes to the bilateral reductions in PI. Arterial compliance is also likely diminished, as suggested by the impaired hypercapnic response observed by our group using arterial spin labelling MRI [199] and reduced compliance measured using dynamic electrocardiography-gated computed tomography angiography following TBI in humans [236]. Changes to vascular structure are greater ipsilaterally where the cortex is directly impacted, with a greater loss of vessels and alterations in vessel diameter [86, 200], consistent with the greater reduction in PI recorded ipsilaterally vs. contralaterally. While PI has been demonstrated using a two-element Windkessel model to increase with heart rate [157], we do not believe that heart rate significantly impacted PI in our study since there was no correlation between PI and heart rate either ipsilaterally or contralaterally. Nevertheless, heart rate had a trend towards a reduction in TBI. It is possible that given the dependence of PI on multiple factors, such as arterial pressure and cerebral perfusion pressure, that changes in these variables mask the effects of heart rate.

Contrary to our expectation, $|Z_{in}|$ did not differ between TBI and shams. We have previously reported using serial two-photon tomography that mice exhibit microvessel dilation following TBI [199], which would be expected to reduce overall impedance. Vasodilation is also consistent with the increased impedance phase (i.e. less negative) observed here. Given that $|Z_{in}|$ increases with decreasing compliance [237], the opposing effects of vasodilation and decreased compliance may explain why changes in impedance modulus were not detected in the TBI condition.

As with PI, PWV was reduced bilaterally in the TBI condition. PWV is a measure of wall stiffness and is proportional to (the square root of) Young's modulus of elasticity [238]. Since Young's modulus has been observed to increase with arterial pressure [239], a reduction in arterial blood pressure could explain the observed reduction in PWV following TBI. There were no changes in arterial wall thickness observed on ultrasound making a change in the mechanical properties of the vessel wall an unlikely explanation.

While it is surprising that there are no blood velocity or flow differences between TBI-1-Day and Sham-1-Day, it is important to note that a sham surgery is a mild form of TBI [214]. CBF is often increased in the early stages following TBI in humans and animal models [22, 152], and this is reflected in our data. Further evidence of the sham group as a mild TBI is seen in the increased flow variability for Sham-1-Day compared to Sham-4-Weeks and TBI-4-Weeks (Figure 4.3).

It is interesting to consider the clinical implications of the ultrasound findings reported here. TBI disrupts microvasculature, inducing changes in structure and function [240]. Thus, techniques which can directly detect microvascular alterations could potentially aid in detecting or grading the severity of TBI. Many studies using ultrasound in TBI [154, 156, 157] have been conducted using transcranial Doppler of the middle cerebral artery. However, transcranial Doppler imaging has been reported to have failure rates of 25 % in adults, with the mature skull impeding ultrasound wave access to large vessels [4, 241]. In contrast, the common carotids, as imaged in our study, are easily accessible. Many TBI studies that perform transcranial Doppler assess features such as flow velocity and PI [242]. None, to our knowledge, have performed a flow-wave decomposition such as that reported here. This flow wave decomposition yields a ROC curve with an AUC of 0.792 using impedance modulus and phase as classifiers, which does not statistically differ from the AUC of 0.716 using PI and diameter as classifiers. Nevertheless, with an AUC approaching 0.8, our findings suggest that wave decomposition has the potential to detect TBI.

4.5.2 Comparison of findings to previous studies

Both reduced [152, 154, 155] and elevated [155, 156, 157, 243] PI have been reported in connection with head trauma. This heterogeneity in the effect of TBI on PI may be attributed to the type of injury acquired. For example, Prasad et al. [155] divided patients into two groups: hypoperfusion and vasospasm (large artery closure). The hypoperfusion group showed increased PI in MCA relative to healthy (ie. non-injured) individuals, whereas the vasospasm group showed reduced PI. Vasospasm may be produced by sub-arachnoid hemorrhage, and results in a PI decrease via compensatory vasodilation of small arterioles [81]. Since there is significant hemorrhage in CCI, it is likely that vasospasm occurred in our model.

A previous study by our group (Macgowan et al. [4]) used a similar wave reflection methodology in 12-week-old C57BL/6J mice, the same background strain as those used in this study. The mean LCCA diameter was reported as 0.422 mm and the PWV was 1.3 m/s compared to a diameter of 0.509 ± 0.009 mm (LCCA) and a PWV of 2.3 m/s in this study. The difference may be explained by the isoflurane concentration (1 vs. 2 %) or the respiration conditions (ventilated vs. free-breathing). Isoflurane is a vasodilator, consistent with a larger carotid artery diameter in our study. There are likely other contributing factors, however, as another study [244] in CD-1 mice calculated similar PWV values to those reported here despite a similar vessel area to Macgowan et al. [4]. It should be noted that estimates of PWV obtained by the QA method have been reported to underestimate PWV due to the limited period of the cardiac cycle that is unaffected by reflection and the limited temporal resolution of pulsed Doppler measurements [245, 246]. There is no reason to expect that this underestimation would preferentially affect any of the subgroups in this present study. In humans, the ultrasound measurement technique described here can be used without anesthesia, eliminating depth of anesthesia as a source of variability from such studies.

Previous clinical studies using hemodynamic-based imaging technologies to diagnose TBI have reported accuracy, sensitivity and specificity greater than that reported here. For example, Karamzadeh et al. (2016) [247] used functional near-infrared spectroscopy of hemodynamic biomarkers in prefrontal cortex to classified TBI in humans with 85 % accuracy, 85 % sensitivity, and 84 % specificity using a Decision Tree machine learning algorithm. Thatcher et al. (2001) [248] performed EEG spectral analyses on 19 scalp locations in patients with mild, moderate, and severe TBI. Discriminant analysis between mild and severe TBI groups demonstrated 96 % accuracy, 95 % sensitivity, and 97 % specificity. Our methodology, in comparison had a 74 % accuracy, 79 % sensitivity, and 70 % specificity. Both Thatcher et al. [248] and Karamzadeh et al. [247] performed discriminant analysis on multiple variables per subject (16 for Thatcher et al. [248], 3 for Karamzadeh et al. [247]). In contrast, only two predictors (impedance modulus and phase) were used in our study. Future studies may combine multiple imaging modalities with the ultrasound methodology proposed here, such as Arterial Spin Labeling MRI as described in our previous work [198], infrared spectroscopy [247], and electrophysiological techniques such as EEG or magnetoencephalography [249] to provide complementary information.

4.6 Conclusions

The cerebral vasculature undergoes significant morphological and structural changes following TBI. These changes occur at the level of the microvasculature and are difficult to visualize in vivo in humans. Non-invasive techniques that indirectly detect these changes are potentially valuable in diagnosing and detecting TBI. This paper applied ultrasound wave reflection analysis in the carotid arteries to a mouse CCI model. Although pulsatility was reduced bilaterally, these changes were likely affected by physiological features such as arterial and cerebral perfusion pressure, in addition to vessel structural changes. In contrast, impedance phase only experienced ipsilateral reductions.

In addition, we demonstrated that quantification of cerebral vascular resistance with ultrasound has the potential to detect whether a mouse received a TBI. Translated to humans, this approach could allow for rapid and non-invasive monitoring of vascular changes following TBI and has potential applications to other disorders, such as stroke and Alzheimer’s disease, where vascular reorganization plays a crucial role.

Chapter 5

Discussion and Conclusions

5.1 Summary of Thesis

The thesis provides an improved understanding of the relationship between microvascular structure and function in TBI. Past descriptions of vascular remodeling in TBI have been restricted to 2D analyses [22, 86], with blood flow measurements often absent [21]. Since resistance to blood flow depends on network topology, 3D imaging is necessary to understand how an evolving vascular architecture impacts blood flow.

CBF and vascular architecture were correlated via a methodology that combined STPT and ASL MRI in an identical imaging space. Since STPT is performed ex vivo, it is unusable in clinical populations. To evaluate cerebrovascular changes in TBI without direct microvessel visualization, an ultrasound technique based on wave reflection theory was applied. This technique was used to assess whether a mouse had received a TBI.

Chapter 1 introduced the goals and background of the thesis. The rationale behind the research and the role of imaging in characterizing vascular remodeling were discussed. This chapter introduced technologies, such as ASL MRI, 2-photon fluorescence microscopy, and ultrasound, which were used to image vascular structure or function in later chapters.

Chapter 2 compared in vivo and ex vivo imaging of the microvasculature with 2PFM and optical clearing. The extent of vessel shrinkage was found to be dependent on vessel type (arterioles vs. capillaries) and size. This differential shrinkage was attributed to anesthesia, and possible effects of craniotomy on vessel diameter. It is also possible that 2 % gelatin does not provide enough structural stability for larger vessels, which may collapse following solidification of the gel. In addition, a segmentation method that accounted for anisotropic and varying resolution was developed. The algorithm was applied to the STPT data in Chapter 3 and detected differences in microvessel diameters of 7 %.

In Chapter 3, in vivo ASL MRI with a hypercapnic challenge and ex vivo STPT were used to examine the relationship between blood flow and microvascular structural changes in TBI. While vessel density and vascular volume recovered 1-month post-TBI, the reorganized vasculature possessed a radial pattern corresponding to low blood flow. This demonstrated that vascular architecture has a functional significance and changes to the vasculature persist long-term post-TBI.

Chapter 4 assessed wave reflection changes in mouse carotid arteries due to TBI. Input impedance and phase were demonstrated to be potential predictors of TBI. PI was demonstrated to be a poor indicator of vascular resistance in the injured state. PI did not correlate with input impedance ipsilaterally but did correlate contralaterally where cerebrovascular damage was reduced compared to the ipsilateral side.

The following section highlights technical considerations for the techniques developed. The chapter concludes with a discussion on Future Directions and Concluding Thoughts.

5.2 Technical Comments and Considerations

A previous 2015 study in our lab used STPT to acquire whole-brain images with spacing of 75 µm between coronal sections [29]. While a smaller brain region was imaged in this thesis, data was acquired at an isotropic voxel size of 2 µm. Since spacing between coronal sections (2 µm) was less than the diameter of a capillary, 3D segmentation of the microvasculature could be performed. Economo et al. (2016) [250] described acquisition of whole-brain mouse images with STPT at voxel size 0.3 x 0.3 x 1.0 μm^3, however their technique required clearing in a dimethyl sulfoxide (DMSO) based solution. DMSO-based clearing agents shrink tissue [167], whereas the thesis' technique does not distort tissue beyond the fixation and perfusion procedure, nor cause optical aberrations.

An advantage to this study is the use of mice with endothelial cells expressing tomato fluorescent protein. Ex vivo vascular images obtained via perfusing wild type mice with a fluorescent gel are susceptible to errors in the perfusion protocol, resulting in unlabeled vessels. This could lead to interpreting a brain region as possessing a low vessel density when it may have been poorly perfused. Although our study perfused the vasculature with a gel, because the endothelial cells were fluorescent, unperfused vessels were also detected. This yields more accurate calculations of vessel density.

Blood flow modeling is performed on vascular segmentations. It has been used in human brain data [251] to predict blood pressure, blood flow, and hematocrit distributions across the whole vascular network, and at the level of individual vessels. In addition, it is possible to model the effect of network flow on global and local vasodilation [252]. Combining ASL MRI with STPT, however, overcomes some of the limitations of flow modeling. Because modeling is performed on network segmentations, errors in the tree, such as spurious connections and gaps, affect the accuracy of calculations [253]. Modeling typically relies on assumptions such as Poiseuille flow in all vessels (cylindrical flow symmetry and minimal turbulence) [254]. The assumption of Poiseuille flow may be inaccurate as the curvature of a vessel increases. With increased curvature, a velocity peak is shifted towards the inside wall and a secondary peak grows toward the outside wall [255]. Since most vessels display curvature, the Poiseuille approximation is not necessarily wholly accurate. Since vessel tortuosity increases in TBI [199], this effect is exacerbated in injury or disease. In addition, flow is often not fully developed near the origin of arteries, as is often assumed in flow modeling [256]. Overall, direct flow measurements via MRI are more accurate and less prone to error.

A drawback to our implementation of STPT is that only the cerebral vasculature was fluorescently labeled. In contrast, Wu et al. [27] modified Nissl staining to label neurons, glia, and vasculature of an entire unsectioned mouse brain. Micro-optical sectioning tomography [119], an automated system that combines tissue slicing and light microscopy, was then used to obtain 3D reconstructions of cell bodies and vasculature. Different cell types were separately segmented, enabling determination of the spatial correlation between cells and blood vessels. Since the staining process requires 25 days [27], it is unfeasible for a TBI study requiring 40 mice. In 2018, Di Giovanna et al. [28] perfused the vasculature of mice whose neurons express fluorescent proteins. This method could be applied to rodent studies without additional sample preparation time beyond that described in this thesis.

5.3 Future Directions

STPT with ASL and ultrasound could be applied to different trauma models or be used to assess the effect of a treatment intervention on vascular architecture. The ultrasound methodology may also be applied to clinical populations. In addition, different vascular remodeling mechanisms may be examined. These points are discussed below.

(A) Applying the imaging methodologies to trauma models

Even at slower speeds and 'mild' CCI injuries, CCI produces strain rates (approximately 400 s^{-1} for a mild CCI) in rodents beyond moderate or severe human TBI [73, 257]. Strain rates are the rate of change in deformation or strain of a material with respect to time and are determined by impact speed [73]. Strain, on the other hand, is determined by deformation depth [73]. At typical CCI speeds, the strain rates range from 1150 to 1450 s^{-1} [73, 258]. In comparison, mild TBI in humans induces strain rates up to approximately 100 s^{-1}, while moderate to severe generally is within 200 s^{-1} [73]. Craniotomies and skull disruptions do not occur with a human concussion. An alternative to open-skull CCI is a closed-skull model, where the skull is impacted without craniotomy. Repeated, closed skull CCI in mice demonstrates angiogenesis together with impaired CBF and cerebrovascular reactivity [74]. Closed-skull impact finite element models are difficult to develop, with challenges present in quantifying mechanical interactions [73]. Nonetheless, these closed skull CCI models display similar features to human injury, such as lack of development of a necrotic cavity, even with multiple impacts [74]. This suggests that the biomechanical forces acting on the brain with closed-skull CCI more accurately resemble the human scenario.

In 2007, a rat injury model where the head was forced to rotate within a coronal plane was developed, where the severity of diffuse brain injury was controlled by adjusting the rate of angular acceleration [259]. More than half the rats displayed either sub-arachnoid hemorrhage distributed throughout the cerebral hemispheres or intraparenchymal lesions [259]. At this level of injury severity, scaling the rodent injury to a human results in an angular acceleration typical of human concussion [259].

While closed skull CCI more closely mirrors the human situation, it fails to account for head rotation, the predominant injury mechanism in concussion [260]. This is overcome via usage of rotational models [93, 259]. These models demonstrate features of human concussion such as unconsciousness and blood brain barrier leakage, with many animals not displaying macroscopic damage visible without a microscope [93, 259]. The models are well-suited to the methodologies in this thesis, since shear forces initiated by rotation often cause microvascular injury [93]. Application of STPT and MRI or ultrasound (either transcranial or via the carotid arteries) to closed skull models (either rotational or closed skull CCI) would better indicate whether the cerebrovascular alterations that occur in open-skull CCI are present clinically.

(B) The effect of exercise timing on vascular remodeling following TBI

Studies [261, 262, 263, 264] demonstrate that exercise improves cognition, delays memory decline, and protects against cortical contusion injuries. Proposed mechanisms for the beneficial effects of exercise include enhanced synaptic plasticity and production of growth factors to promote neuronal survival [265]. Exercise in healthy humans and animals leads to angiogenesis in hippocampus, cortex, and cerebellum. This angiogenesis occurs to support the increased energy and nutrient needs of exercise-induced changes such as enhanced plasticity and neurogenesis [265].

The effects of exercise on vasculature often appear following completion of the exercise regimen. In a mouse study by Pereira et al. (2007) [266], increases in cerebral blood volume (CBV) measured with MRI following a two-week exercise regimen occurred in the dentate gyrus, peaking two weeks post-exercise cessation. This CBV increase is likely caused by angiogenesis [267]. The increase correlated with increased neurogenesis, suggesting a relationship between vascular and neural growth [266]. Effects in mice are similar to those observed in humans, with 12-weeks of cardiovascular training in humans increasing dentate gyrus CBV and improving cognitive function [266].

The relationship between angiogenesis and neurogenesis in dentate gyrus is attributed to the proximity between newly formed cells and blood vessels. For example, Palmer et al. (2000) [268] observed in adult rats that dividing cells form dense clusters, with 37 % of cells within the cluster immunoreactive for endothelial markers. In addition, surrounding areas express VEGF, with cells within the cluster expressing VEGF receptors [268]. The clustering of endothelial and neural precursors is interpreted by Palmer et al. [268] as suggesting that neurogenesis involves shared signaling processes with endothelial precursors. Exercise increases the concentration of angiogenic molecules such as VEGF and angiopoietin 1 and 2 [265, 267, 269, 270]. VEGF is produced in response to exercise-induced hypoxia, since a hypoxic response element is present within the VEGF promoter and responds to HIF-1α binding, where HIF-1α is overexpressed in hypoxic conditions [271]. Even in aging rats (22 months old), exercising on a treadmill for 3 weeks at 30 minutes/day, 6 days/weeks increases vessel density in cortex and striatum following cessation of exercise [269]. This increased density corresponds to increased mRNA levels of Ang-1, Ang-2, and VEGF (three angiogenic factors) [269].

Increasing vessel density could potentially aid in restoring blood flow following TBI. In addition, while increasing vessel density through VEGF expression, VEGF also stimulates hippocampal neurogenesis in rats [272] and increases the number of surviving cultured mouse cortical neurons in response to hypoxia and glucose deprivation [273]. These findings suggest that exercise following TBI has the potential to restore blood flow and protect against neuronal death.

However, to optimize the effectiveness of exercise, the timing of its introduction post-injury requires consideration. In a study by Griesbach et al. (2004) [274] in rats that received a fluid percussion injury, animals were provided access to a running wheel immediately following injury (days 0 – 6, acute exercise group) or two-weeks post-injury (14 – 20 days, delayed exercise group). Griesbach et al. observed that mice in the delayed exercise group expressed elevated brain-derived neurotrophic factor (BDNF, a molecule that promotes neuronal survival) relative to the acute exercise group, which demonstrated impaired BDNF upregulation and significant decreases in CREB (transcription factor that contributes to synaptic plasticity). Other studies also suggest that exercise begun shortly after injury negatively impacts recovery. In rats, forced exercise during the first seven days after a motor cortex injury increases brain lesion size [275]. In student athletes, high levels of cognitive and physical activity post-injury reduce performance on visual memory and reaction time tests [276]. However, this study was conducted on data from patient records and did not specify the time frame for which these cognitive deficits occurred or whether they were permanent [276].

Other studies suggest remodeling could differ depending on the timing of exercise introduction. For example, VEGF increases blood-brain-barrier leakage, edema, and hemorrhage when administered 1 hour after stroke in rats. These effects are not present if administration is postponed 48 hours [277]. In a weight-drop model of TBI in mice, exposure to hypoxia 3 hours after injury exacerbated the inflammatory response and severity of secondary brain injury [278]. This suggests if mice exercise prematurely, the resulting hypoxia could increase inflammation. This hypothesis is backed by a study showing if exercise is initiated one week and lasts for four-weeks post-trauma in CCI in mice, there is an increase in neurotoxic, pro-inflammatory responses relative to mice who began exercising four-weeks post-injury [279]. Chronic inflammation is associated with increased macrophage infiltration, edema, and tissue damage [280].

The techniques developed in this thesis could be used to examine the effects of exercise on vascular remodeling post-TBI. In this hypothetical study, mice receive a TBI and are permitted to exercise beginning immediately following injury or 2-weeks post-injury as per Griesbach et al. [274]. Since previous studies have shown that four weeks of voluntary running-wheel exercise enhances cortical vascular efficiency [202] and improves blood flow and vascular function [281], four-weeks of exercise should be sufficient to induce observable effects. These effects would be visualized at the microvascular structural level with STPT, or macroscopically with ASL MRI or ultrasound. If exercise is therapeutic and produces a more efficient vascular network, perhaps the remodeled vasculature in TBI would differ from the abnormal radial pattern observed in Chapter 3. These results may contribute to improved guidelines for return to exercise activities in humans and to the successful use of exercise as a therapeutic tool.

(C) Use of ultrasound to distinguish between TBI and healthy condition

Chapter 4 demonstrated that ultrasound based on wave reflection has the potential to distinguish between the TBI and sham condition in the CCI model. Human concussions, however, do not display the severity of injury observed in CCI. Prior to applying wave reflection analysis to a clinical study, it may be examined in animal TBI models which do not display overt damage such as hematomas and swelling. This would help determine whether the differences observed in CCI animals are still present in more severe injury situations.

(D) Analyzing different vascular remodeling mechanisms

While this thesis described microvascular structural alterations in TBI and correlated them with macroscopic blood flow measurements, it did not examine mechanisms of vascular remodeling ie. the factors that cause vessel networks to remodel. Organization and remodeling of a vessel network occurs on multiple levels as described by Secomb and Pries (2016) [282]: vasculogenesis (de novo formation of new vessels); angiogenesis (sprouting of new capillaries from pre-existing capillaries, often in response to hypoxia); remodeling (changes in diameter and wall structure); and pruning (removal of vessels). These mechanisms likely work together through cell-to-cell signaling, and possibly communicate tissue metabolic state via signaling across tight junctions in vessels [282].

Optimal networks possess sufficient capillary numbers with a 3D distribution to minimize oxygen diffusion distances; and large diameter vessels (arteries, veins) to distribute the blood efficiently and minimize resistance to flow [283]. This optimal network is achieved through development of a hierarchical network structure, where a small number of branching vessels with varying diameter (arteries/arterioles, veins/venules) connect with the capillary bed [283]. Murray (1926) [210] mathematically demonstrated that to minimize 'work' in a hierarchical network, defined as the viscous energy dissipation in small vessels plus a term related to total blood volume, flow through each vessel is proportional to the cube of the diameter [283]. This is equivalent to a uniform wall shear stress throughout the vessel tree [283].

The analysis presented here quantifies vessel number and overall network architecture but does not shed light on remodeling mechanisms. In tumors, there is a high proportion of hypoxic tissue despite high VEGF expression and vessel density. VEGF disrupts vessel wall integrity and gap junction function [283, 284]. It has been suggested via hemodynamic modeling that poor tissue perfusion in tumors may be a result of functional shunting ie. flow not properly distributed between long and short pathways, often bypassing the capillary bed [283, 285, 286]. Such networks could display high perfusion, without providing appropriate metabolic support to tissue.

To quantify vessel network efficiency in future experiments, additional analysis techniques may be incorporated. Hemodynamic calculations on the segmented vascular trees may highlight whether wall sheer stress variation is minimized, as predicted by Murray [210]. Adams et al. (2018) [74] used Arterial Spin Labeling MRI in a closed-skull CCI mouse model to quantify arterial transit time. Vascular transit time may also be calculated via the in vivo 2-photon 'bolus tracking' methodology described by Dorr et al. (2012) [12], where the time for the fluorescent bolus to travel through the microvascular network is monitored. In vivo 2-photon microscopy may be utilized in a longitudinal study to visualize structural evolution of vessel networks following TBI. According to hemodynamic models [283], in vascular remodeling in healthy tissue, there is initially a disordered mesh of vessels that are formed in response to hypoxia. Vessels sprouts that experience higher flow and shear stress grow larger diameters, ultimately undergoing identity changes into arteries and veins [287]. Redundant vessels that experience minimal flow are pruned [283]. These changes are difficult to quantify with ex vivo microscopy. However, it is possible to visualize longitudinally with in vivo 2-photon microscopy, as demonstrated by Harb et al. (2012) [288] in mouse brains from neonates to aged adults (25 months old) . To determine whether this remodeling contributes to a uniform or reduced wall shear stress, in vivo 2-photon can be used to estimate shear stress for individual vessels through calculation of the vessel's diameter, blood velocity, and estimation of blood viscosity [289].

5.4 Concluding Thoughts

Vascular architecture and remodeling are critical in organ development [290], tumor hypoxia [291], and in a variety of injuries or diseases such as stroke [292] and diabetes [293]. 3D architecture has previously been described in rodents. Large diameter pial vessels and the capillary network form collaterals to protect against the effects of vessel occlusion [33, 36]. Penetrating arterioles deliver blood to a columnar region of tissue, and occlusion of these vessels leads to infarcts and cognitive deficits [35].

Studies assessing functionality of this architecture have been limited in the sample volume analyzed. Capillary-resolution data sets encompassed a small tissue volume, on the order of a few cubic millimeters [294]. In contrast, ASL and STPT were correlated over a volume of 8 mm^3. Vascular injury and disease will affect large volumes of tissue, with variations in vascular architecture occurring across cortical regions [295]. Techniques with limited imaging depth, such as confocal microscopy of 300 µm thick tissue slabs [175], do not capture this variation.

Previous studies have combined ASL with microvascular imaging in rodents in TBI, quantifying vessel density with registration to ASL [22, 30]. While valuable in characterizing vessel density and CBF change over time, questions remained: (1) Why is there often no correlation between CBF and density? (2) Why does revascularization occur in the cortex without concurrent CBF recovery? (3) What is the role of the 3D vascular architecture in influencing CBF?

The thesis sheds light on these questions. Vessel density most strongly correlates with CBF in the hypercapnic state. Since Hayward et al. [22, 30] only examined rest CBF, a correlation may have been found had hypercapnic CBF been measured. A similar observation has been noted in transgenic mice overexpressing VEGF, where CBF is barely raised in transgenic animals under rest despite a nearly three-fold increase in capillary density. Under hypercapnia there is a significantly greater increase in CBF compared to controls, indicating recruitment of additional vessel capacity [18].

Reduced vessel density only partially explains impaired CBF, since months following trauma increased vessel density corresponds to reduced blood flow [30]. Our results indicate that the radial pattern performs poorly in comparison to networks found in uninjured animals. Further evidence of the role of 3D network architecture is seen in the correlation between CBF and diameter scaling coefficient. A complete understanding of the relationship between CBF and vessel structure requires information on state (hypercapnia vs. rest), 2D metrics (such as vessel density and diameter), and 3D architecture (such as radial patterning and hierarchical branching).

The thesis' findings have ramifications for optimizing treatments for TBI or vascular-related diseases. Siddiq et al. (2012) [104] administered VEGF to rats following fluid percussion injury, demonstrating recovery of microvascular density two weeks post-injury in cortex relative to untreated animals. While VEGF administration has benefits such as reduced cell death [104], VEGF may act directly on neurons through inhibition of cell death pathways, as opposed to increasing blood flow. This is evident is the study by Wang et al. (2005) [296], where VEGF-overexpressing mice demonstrate reduced blood flow in ipsilateral cortex following MCA stroke in comparison with non-transgenic mice exposed to the same stroke. Vogel et al. [18] note that VEGF overexpressing mice likely have an inefficiently remodeled vasculature, such as elongated vessels which increase network tortuosity and resistance. Larger clinical trials for treatment of ischemia with VEGF have been unsuccessful, possibly due to this absence of increased flow and abnormal vessel structure [296, 297]. Treatments such as exercise, which are known to induce extensive vessel remodeling [23] and increased microvascular efficiency [202, 281], have the potential to simultaneously increase microvessel density and blood flow, and should be considered as possible replacement for VEGF administration. In highlighting the importance of vascular architecture, the thesis emphasizes that the most effective treatments should optimize network architecture, and not merely replace lost vessels.

To summarize, this thesis involved development of an imaging methodology for quantitative analysis of mouse cerebral vascular structure and function. Although applied to a TBI model, it is applicable to any disease or condition in any organ. Our findings suggest that assessing the effect of treatments must go beyond quantifying the number of vessels. In manipulating vessel remodeling, functional tissue depends on a network of capillaries and microvessels (arterioles and venules), a sufficient density of microvasculature, and the organization and connections between vessels in a network [298]. To generate a functional vascular network therefore may require therapies beyond administration of growth factors promoting angiogenesis.

References

[1] T. Ragan, L. R. Kadiri, K. U. Venkataraju, K. Bahlmann, J. Sutin, J. Taranda , I. Arganda-Carreras, Y. Kim, H. S. Seung and P. Osten, "Serial two-photon tomography for automated ex vivo mouse brain imaging," *Nature Methods,* vol. 9, pp. 255-258, 2012.

[2] J. A. Detre, J. S. Leigh, D. S. Williams and A. P. Koretsky, "Perfusion imaging," *Magnetic Resonance in Medicine,* vol. 23, pp. 37-45, 1992.

[3] B. P. Chugh, J. Bishop, Y. Q. Zhou, J. Wu, R. M. Henkelman and J. G. Sled, "Robust method for 3D arterial spin labeling in mice," *Magnetic Resonance in Medicine,* vol. 68, pp. 98-106, 2012.

[4] C. K. Macgowan, S. J. Stoops, Y. Q. Zhou, L. S. Cahill and J. G. Sled, "Evaluation of cerebrovascular impedance and wave reflection in mouse by ultrasound," *Journal of Cerebral Blood Flow and Metabolism,* vol. 35, pp. 521-526, 2015.

[5] D. Attwell and S. B. Laughlin, "An energy budget for signaling in the grey matter of the brain," *Journal of Cerebral Blood Flow and Metabolism,* vol. 21, pp. 1133-1145, 2001.

[6] P. S. Tsai, J. Kaufhold, P. Blinder , B. Friedman, P. J. Drew, H. J. Karten, P. D. Lyden and D. Kleinfeld, "Correlations of neuronal and microvascular densisties in murine cortex revealed by direct counting and colocalization of nuclei and vessels," *Journal of Neuroscience,* vol. 29, pp. 14553-14570, 2009.

[7] S. Zhang and T. H. Murphy, "Imaging the impact of cortical microcirculation on synaptic structure and sensory-evoked hemodynamic responses in vivo," *PLOS Biology,* vol. 5, p. e119, 2007.

[8] S. Zhang, J. Boyd, K. Delaney and T. H. Murphy, "Rapid reversible changes in dendritic spine structure in vivo gated by the degree of ischemia," *The Journal of Neuroscience,* vol. 25, pp. 5333-5338, 2005.

[9] B. Quirstorff, B. Chance and A. Hunding, "An experimental model of the Krogh tissue cylinder: two dimensional quantitation of the oxygen gradient," *Advances in Experimental Medicine and Biology,* vol. 94, pp. 127-136, 1977.

[10] G. A. Dienel and L. Hertz, "Astrocytic contributions to bioenergetics of cerebral ischemia," *Glia,* vol. 50, pp. 362-388, 2005.

[11] C. Morland, K. A. Andersson, Ø. P. Haugen, A. Hadzic, L. Kleppa, A. Gille, J. E. Rinholm, V. Palibrk, E. H. Diget, L. H. Kennedy, T. Stølen, E. Hennestad, O. Moldestad, Y. Cai, M. Puchades, S. Offermanns, K. Vervaeke, M. Bjørås, U. Wisløff, J. Storm-Mathisen and L. H. Bergersen, "Exercise induces cerebral VEGF and angiogenesis via the lactate receptor HCAR1," *Nature Communications,* vol. 8, p. 15557, 2017.

[12] A. Dorr, B. Sahota, V. Lakshminarayan, M. E. Brown, A. Y. Lai, K. Ma, C. A. Hawkes, J. McLaurin and B. Stefanovic, "Amyloid-β-dependent compromise of microvascular structure and function in a model of Alzheimer’s disease," *Brain,* vol. 135, pp. 3039-3050, 2012.

[13] R. Prakash, M. Johnson, S. C. Fagan and A. Ergul, "Cerebral neovascularization and remodeling patterns in two different models of type 2 diabetes," *PLOS One,* vol. 8, p. e56264, 2013.

[14] A. Letourneur, V. Chen, G. Waterman and P. J. Drew, "A method for longitudinal, transcranial imaging of blood flow and remodeling of the cerebral vasculature in postnatal mice," *Physiological Reports,* vol. 2, p. e12238, 2014.

[15] J. Liu, Y. Wang, Y. Akamatsu, C. C. Lee, R. A. Stetler, M. T. Lawton and G. Y. Yang, "Vascular remodeling after ischemic stroke: mechanisms and therapeutic potentials," *Progress in Neurobiology,* vol. 115, pp. 138-156, 2014.

[16] M. Dzietko, M. F. Wendland, Z. S. Vexler and D. M. Ferriero, "Delayed VEGF treatment enhances angiogenesis and recovery after neonatal focal rodent stroke," *Translational Stroke Research,* vol. 4, pp. 189-200, 2013.

[17] O. Thau-Zuchman, E. Shohami, A. G. Alexandrovich and R. R. Leker, "Subacute treatment with vascular endothelial growth factor after traumatic brain injury increases angiogenesis and gliogenesis," *Neuroscience,* vol. 202, pp. 334-341, 2012.

[18] J. Vogel, M. Gehrig, W. Kuschinsky and H. H. Marti, "Massive inborn angiogenesis in the brain scarcely raises cerebral blood flow," *Journal of Cerebral Blood Flow and Metabolism,* vol. 24, pp. 849-859, 2004.

[19] J. R. Less, M. C. Posner, T. C. Skalak, N. Wolmark and R. K. Jain, "Geometric resistance and microvascular network architecture of human colorectal carcinoma," *Microcirculation,* vol. 4, pp. 25-33, 1997.

[20] B. P. Chugh, J. P. Lerch, L. X. Yu, M. Pienkowski, R. V. Harrison, R. M. Henkelman and J. G. Sled, "Measurement of cerebral blood volume in mouse brain regions using micro-computed tomography," *NeuroImage,* vol. 47, pp. 1312-1318, 2009.

[21] E. Park, J. D. Bell, I. P. Siddiq and A. J. Baker, "An analysis of regional microvascular loss and recovery following two grades of fluid percussion trauma: a role for hypoxia-inducible factors in traumatic brain injury," *Journal of Cerebral Blood Flow and Metabolism,* vol. 29, pp. 575-584, 2009.

[22] N. M. Hayward, P. I. Tuunanen, R. Immonen, X. E. Ndode-Ekane, A. Pitkänen and O. Gröhn, "Magnetic resonance imaging of regional hemodynamic and cerebrovascular recovery after lateral fluid-percussion brain injury in rats," *Journal of Cerebral Blood Flow and Metabolism,* vol. 31, pp. 166-177, 2011.

[23] K. R. Isaacs, B. J. Anderson, A. A. Alcantara, J. E. Black and W. T. Greenough, "Exercise and the brain: angiogenesis in the adult rat cerebellum after vigorous physical activity and motor skill learning," *Journal of Cerebral Blood Flow and Metabolism,* vol. 12, pp. 110-119, 1992.

[24] B. Klein, W. Kuschinsky, H. Schrök and F. Vetterlein, "Interdependency of local capillary density, blood flow, and metabolism in rat brains," *The American Journal of Physiology,* vol. 251, pp. H1333-H1340, 1986.

[25] J. M. Hunter, J. Kwan, M. Malek-Ahmadi, C. L. Maarouf, T. A. Kokjohn, C. Belden, M. N. Sabbagh, T. G. Beach and A. E. Roher, "Morphological and pathological evolution of the brain microcirculation in aging and Alzheimer's disease," *PLOS One,* vol. 7, p. e36893, 2012.

[26] E. Lugo-Hernandez, A. Squire , N. Hagemann, A. Brenzel, M. Sardari, J. Schlechter, E. H. Sanchez-Mendoza, M. Gunzer, A. Faissner and D. M. Hermann, "3D visualization and quantification of microvessels in the whole ischemic mouse brain using solvent-based

clearing and light sheet microscopy," *Journal of Cerebral Blood Flow and Metabolism,* vol. 37, pp. 3355-3367, 2017.

[27] J. Wu, Y. He, C. Guo, Q. Luo, W. Zhou, S. Chen, A. Li, B. Xiong, T. Jiang and H. Gong, "3D BrainCV: Simultaneous visualization and analysis of cells and capillaries in a whole mouse brain with one-micron resolution," *NeuroImage,* vol. 87, pp. 199-208, 2014.

[28] A. P. Di Giovanna, A. Tibo, L. Silvestri, M. C. Mullenbroich, I. Costantini, A. L. Mascaro, L. Sacconi, P. Frasconi and F. S. Pavone, "Whole-brain vasculature reconstruction at the single capillary level," *Scientific Reports,* vol. 8, p. 12573, 2018.

[29] D. A. Vousden, J. Epp, H. Okuno, B. J. Nieman, M. van Eede, J. Dazai, T. Ragan, H. Bito, P. W. Frankland, J. P. Lerch and R. M. Henkelman, "Whole-brain mapping of behaviourally induced neural activation in mice," *Brain Structure and Function,* vol. 220, pp. 2043-2057, 2015.

[30] N. M. Hayward, R. Immonen, P. I. Tuunanen, X. E. Ndode-Ekane, O. Gröhn and A. Pitkänen, "Association of chronic vascular changes with functional outcome after traumatic brain injury in rats," *Journal of Neurotrauma,* vol. 27, pp. 2203-2219, 2010.

[31] A. Jullienne, A. Salehi, B. Affeldt, M. Baghchechi, E. Haddad, A. Avitua, M. Walsworth, I. Enjalric, M. Hamer, S. Bhakta, J. Tang, J. H. Zhang, W. J. Pearce and A. Obenaus, "Male and Female Mice Exhibit Divergent Responses of the Cortical Vasculature to Traumatic Brain Injury," *Journal of Neurotrauma,* vol. 35, pp. 1646-1658, 2018.

[32] D. I. Graham, J. H. Adams, J. A. Nicoll, W. L. Maxwell and T. A. Gennarelli, "The nature, distribution, and causes of traumatic brain injury," *Brain Pathology,* vol. 5, pp. 397-406, 1995.

[33] P. Blinder , A. Y. Shih, C. Rafie and D. Kleinfeld, "Topological basis for the robust distribution of blood to rodent neocortex," *PNAS,* vol. 107, pp. 12670-12675, 2010.

[34] J. A. Boero, J. Ascher, A. Arregui, C. Rovainen and T. A. Woolsey, "Increased brain capillaries in chronic hypoxia," *Journal of Applied Physiology,* vol. 86, pp. 1211-1219, 1999.

[35] A. Y. Shih, C. Rühlmann, P. Blinder, A. Devor, P. J. Drew, B. Friedman, P. M. Knutsen, P. D. Lyden, C. Mateo, L. Mellander, N. Nishimura, C. B. Schaffer, P. S. Tsai and D. Kleinfeld, "Robust and fragile aspects of cortical blood flow in relation to the underlying angioarchitecture," *Microcirculation,* vol. 22, pp. 204-218, 2015.

[36] A. Y. Shih, P. Blinder, P. S. Tsai, B. Friedman, G. Stanley, P. D. Lyden and D. Kleinfeld, "The smallest stroke: occlusion of one penetrating vessel leads to infarction and a cognitive deficit," *Nature Neuroscience,* vol. 16, pp. 55-63, 2013.

[37] S. Sakadžić, E. T. Mandeville, L. Gagnon, J. J. Musacchia, M. A. Yaseen, M. A. Yucel, J. Lefebvre, F. Lesage, A. M. Dale, K. Eikermann-Haerter, C. Ayata, V. J. Srinivasan, E. H. Lo, A. Devor and D. A. Boas, "Large arteriolar component of oxygen delivery implies a safe margin of oxygen supply to cerebral tissue," *Nature Communications,* vol. 5, p. 5734, 2014.

[38] J. C. de la Torre, "Alzheimer disease as a vascular disorder: nosological evidence," *Stroke,* vol. 33, pp. 1152-1162, 2002.

[39] P. Delafontaine-Martel, J. Lefebvre, P. Tardif, B. I. Lévy, P. Pouliot and F. Lesage, "Whole brain vascular imaging in a mouse model of Alzheimer's disease with two-photon microscopy," *Journal of Biomedical Optics,* vol. 23, p. 076501, 2018.

[40] J. C. de la Torre, "Cerebral hypoperfusion, capillary degeneration, and development of Alzheimer disease," *Alzheimer Disease and Associated Disorders,* vol. 14 (Suppl 1), pp. S72-S81, 2000.

[41] S. Janelidze, D. Lindqvist, V. Francardo, S. Hall, H. Zetterberg, K. Blennow, C. H. Adler, T. G. Beach, G. E. Serrano, D. van Westen, E. Londos, M. A. Cenci and O. Hansson, "Increased CSF biomarkers of angiogenesis in Parkinson disease," *Neurology,* vol. 85, pp. 1834-1842, 2015.

[42] S. Sarkar, J. Raymick, D. Mann, J. F. Bowyer, J. P. Hanig, L. C. Schmued, M. G. Paule and S. Chigurupati, "Neurovascular changes in acute, sub-acute, and chronic mouse models of Parkinson's disease," *Current Neurovascular Research,* vol. 11, pp. 48-61, 2014.

[43] C. Barcia, M. E. Emborg, E. C. Hirsch and M. T. Herrero, "Blood vessels and parkinsonism," *Frontiers in Bioscience,* vol. 9, pp. 277-282, 2004.

[44] V. E. Johnson, D. F. Meaney, D. K. Cullen and D. H. Smith, "Animal models of traumatic brain injury," *Handbook of Clinical Neurology,* vol. 127, pp. 115-128, 2015.

[45] G. W. Hawryluk and M. R. Bullock, "Chapter 47 - Design of acute neuroprotection studies," *Handbook of Clinical Neurology,* vol. 128, pp. 761-778, 2015.

[46] Y. Xiong, A. Mahmood and M. Chopp, "Animal models of traumatic brain injury," *Nature Reviews Neuroscience,* vol. 14, pp. 128-142, 2013.

[47] R. M. Guerriero, C. C. Giza and A. Rotenberg, "Glutamate and GABA imbalance following traumatic brain injury," *Current Neurology and Neuroscience Reports,* vol. 15, p. 27, 2015.

[48] T. A. Gennarelli, "Mechanisms of brain injury," *The Journal of Emergency Medicine,* vol. 11(Suppl 1), pp. 5-11, 1993.

[49] D. F. Meaney, B. Morrison and C. D. Bass, "The mechanics of traumatic brain injury: A review of what we know and what we need to know for reducing its societal burden," *Journal of Biomechanical Engineering,* vol. 136, pp. 0210081-02100814, 2014.

[50] T. A. Gennarelli, L. E. Thibault, J. H. Adams, D. I. Graham, C. J. Thompson and R. P. Marcincin, "Diffuse axonal injury and traumatic coma in the primate," *Annals of Neurology,* vol. 12, pp. 564-574, 1982.

[51] J. T. Povlishock, D. P. Becker, C. L. Cheng and G. W. Vaughan, "Axonal change in minor head injury," *Journal of Neuropathology and Experimental Neurology,* vol. 42, pp. 225-242, 1983.

[52] W. T. O'Connor, A. Smyth and M. D. Gilchrist, "Animal models of traumatic brain injury: A critical evaluation," *Pharmacology & Therapeutics,* vol. 130, pp. 106-113, 2011.

[53] C. W. Hoge, D. McGurk, J. L. Thomas, A. L. Cox, C. C. Engel and C. A. Castro, "Mild traumatic brain injury in U.S. soldiers returning from Iraq," *The New England Journal of Medicine,* vol. 358, pp. 453-463, 2008.

[54] E. Park, R. Eisen, A. Kinio and A. J. Baker, "Electrophysiological white matter dysfunction and association with neurobehavioral deficits following low-level primary blast trauma," *Neurobiology of Disease,* vol. 52, pp. 150-159, 2013.

[55] V. E. Koliatsos, I. Cernak, L. Xu, Y. Song, A. Savonenko, B. J. Crain, C. G. Eberhart, C. E. Frangakis, T. Melnikova, H. Kim and D. Lee, "A mouse model of blast injury to brain: initial

pathological, neuropathological, and behavioral characterization," *Journal of Neuropathology and Experimental Neurology,* vol. 70, pp. 399-416, 2011.

[56] P. B. Pun, E. M. Kan, A. Salim, Z. Li, K. C. Ng, S. M. Moochhala, E. A. Ling, M. H. Tan and K. Lu, "Low level primary blast injury in rodent brain," *Frontiers in Neurology,* vol. 2, p. 19, 2011.

[57] M. Liu, C. Zhang, W. Liu, P. Luo, L. Zhang, Y. Wang, Z. Wang and Z. Fei, "A novel rat model of blast-induced traumatic brain injury simulating different damage degree: implications for morphological, neurological, and biomarker changes," *Frontiers in Cellular Neuroscience,* vol. 9, p. 168, 2015.

[58] S. Lindgren and L. Rinder, "Experimental studies in head injury. I. Some factors influencing results of model experiments," *Biophysik,* vol. 2, pp. 320-329, 1965.

[59] T. Kita, T. Tanaka, N. Tanaka and Y. Kinoshita, "The role of tumor necrosis factor-α in diffuse axonal injury following fluid-percussive brain injury in rats," *International Journal of Legal Medicine,* vol. 113, pp. 221-228, 2000.

[60] S. Kleiven, "Why Most Traumatic Brain Injuries are Not Caused by Linear Acceleration but Skull Fractures are," *Frontiers in Bioengineering and Biotechnology,* vol. 1, p. 15, 2013.

[61] T. Gennarelli, L. Thibault, G. Tomei, R. Wiser, D. Graham and J. Adams, "Directional Dependence of Axonal Brain Injury due to Centroidal and Non-Centroidal Acceleration," in *SAE Technical Paper 872197*, 1987.

[62] D. M. Feeney, M. G. Boyeson, R. T. Linn, H. M. Murray and W. G. Dail, "Responses to cortical injury: I. Methodology and local effects of contusions in the rat," *Brain Research,* vol. 211, pp. 67-77, 1981.

[63] M. J. Kane, M. Angoa-Pérez, D. I. Briggs, D. C. Viano, C. W. Kreipke and D. M. Kuhn, "A mouse model of human repetitive mild traumatic brain injury," *Journal of Neuroscience Methods,* vol. 203, pp. 41-49, 2012.

[64] T. H. Hsieh, J. W. Kang, J. H. Lai, Y. Z. Huang, A. Rotenberg, K. Y. Chen, J. Y. Wang, S. Y. Chan, S. C. Chen, Y. H. Chiang and C. W. Peng, "Relationship of mechanical impact magnitude to neurologic dysfunction severity in a rat traumatic brain injury model," *PLOS One,* vol. 12, p. e1078186, 2017.

[65] E. M. Lillie, J. E. Urban, S. K. Lynch, A. A. Weaver and J. D. Stitzel, "Evaluation of Skull Cortical Thickness Changes With Age and Sex From Computed Tomography Scans," *Journal of Bone and Mineral Research,* vol. 31, pp. 299-307, 2016.

[66] T. J. McColl, R. D. Brady, S. R. Shultz, L. Lovick, K. M. Webster, M. Sun, S. J. McDonald, T. J. O'Brien and B. D. Semple, "Mild Traumatic Brain Injury in Adolescent Mice Alters Skull Bone Properties to Influence a Subsequent Brain Impact at Adulthood: A Pilot Study," *Frontiers in Neurology,* vol. 9, p. 372, 2018.

[67] M. Kawakami and K. Yamamura, "Cranial bone morphometric study among mouse strains," *BMC Evolutionary Biology,* vol. 8, p. 73, 2008.

[68] H. L. Laurer, P. M. Lenzlinger and T. K. McIntosh, "Models of traumatic brain injury," *European Journal of Trauma,* vol. 26, pp. 95-110, 2000.

[69] S. Villapol, K. R. Byrnes and A. J. Symes, "Temporal dynamics of cerebral blood flow, cortical damage, apoptosis, astrocyte-vasculature interaction and astrogliosis in the pericontusional region after traumatic brain injury," *Frontiers in Neurology,* vol. 5, p. 82, 2014.

[70] I. Cernak, "Animal models of head trauma," *NeuroRx,* vol. 2, pp. 410-422, 2005.

[71] S. Sangiorgi, A. De Benedictis, M. Protasoni, A. Manelli, M. Reguzzoni, A. Cividini, C. Dell'orbo, G. Tomei and S. Balbi, "Early-stage microvascular alterations of a new model of controlled cortical traumatic brain injury: 3D morphological analysis using scanning electron microscopy and corrosion casting," *Journal of Neurosurgery,* vol. 118, pp. 763-774, 2013.

[72] D. L. Brody, C. Mac Donald, C. C. Kessens, C. Yuede, M. Parsadanian, M. Spinner, E. Kim, K. E. Schwetye, D. M. Holtzman and P. V. Bayly, "Electromagnetic controlled cortical impact device for precise, graded experimental traumatic brain injury," *Journal of Neurotrauma,* vol. 24, pp. 657-673, 2007.

[73] Y. C. Chen, H. Mao, K. H. Yang, T. Abel and D. F. Meaney, "A modified controlled cortical impact technique to model mild traumatic brain injury mechanics in mice," *Frontiers in Neurology,* vol. 5, p. 100, 2014.

[74] C. Adams, P. Bazzigaluppi, T. L. Beckett, J. Bishay, I. Weisspapir, A. Dorr, J. R. Mester, J. Steinman, L. Hirschler, J. M. Warnking, E. L. Barbier, J. McLaurin, J. G. Sled and B. Stefanovic, "Neurogliovascular dysfunction in a model of repeated traumatic brain injury," *Theranostics,* vol. 8, pp. 4824-4836, 2018.

[75] J. Hekmatpanah and C. R. Hekmatpanah, "Microvascular alterations following cerebral contusion in rats. Light, scanning, and electron microscope study," *Journal of Neurosurgery,* vol. 62, pp. 888-897, 1985.

[76] H. C. Han , "Twisted blood vessels: symptoms, etiology and biomechanical mechanisms," *Journal of Vascular Research,* vol. 49, pp. 185-197, 2012.

[77] J. M. Ziebell, R. K. Rowe, J. L. Harrison, K. C. Eakin, T. Colburn, F. A. Willyerd and J. Lifshitz, "Experimental diffuse brain injury results in regional alteration of gross vascular pathology independent of neuropathology," *Brain Injury,* vol. 30, pp. 217-224, 2016.

[78] N. Hattori, S. C. Huang, H. M. Wu, W. Liao, T. C. Glenn, P. M. Vespa, M. E. Phelps, D. A. Hovda and M. Bergsneider, "PET investigation of post-traumatic cerebral blood volume and blood flow," *Acta Neurochirurgica Supplement,* vol. 86, pp. 49-52, 2003.

[79] E. P. Wei, W. D. Dietrich, J. T. Povlishock, R. M. Navari and H. A. Kontos, "Functional, morphological, and metabolic abnormalities of the cerebral microcirculation after concussive brain injury in cats," *Circulation Research,* vol. 46, pp. 37-47, 1980.

[80] R. H. Wilkins and G. L. Odom, "Intracranial arterial spasm associated with craniocerebral trauma," *Journal of Neurosurgery,* vol. 32, pp. 626-633, 1970.

[81] V. Rajajee, J. J. Fletcher, A. S. Pandey, J. J. Gemmete, N. Chaudhary, T. L. Jacobs and B. G. Thompson, "Low pulsatility index on transcranial Doppler predicts symptomatic large-vessel vasospasm after aneurysmal subarachnoid hemorrhage," *Neurosurgery,* vol. 70, pp. 1195-1206, 2012.

[82] J. P. Evans and I. M. Scheinker, "Histologic studies of the brain following head trauma. I. Post-traumatic cerebral swelling and edema," *Journal of Neurosurgery,* vol. 2, pp. 306-314, 1945.

[83] I. M. Scheinker, "Vasoparalysis of the central nervous system, a characteristic vascular syndrome. Significance in the pathology of the central nervous system," *Archives of Neurology and Psychiatry,* vol. 52, pp. 43-56, 1944.

[84] P. Toth, N. Szarka, E. Farkas, E. Ezer, E. Czeiter, K. Amrein, Z. Ungvari, J. A. Hartings, A. Buki and A. Koller, "Traumatic brain injury-induced autoregulatory dysfunction and spreading depression-related neurovascular uncoupling: Pathomechanisms, perspectives, and therapeutic implications," *American Journal of Physiology. Heart and Circulatory Physiology,* vol. 311, pp. H1118-H1131, 2016.

[85] M. Czosnyka, P. Smielewski, S. Piechnik, L. A. Steiner and J. D. Pickard, "Cerebral autoregulation following head injury," *Journal of Neurosurgery,* vol. 95, pp. 756-763, 2001.

[86] A. Obenaus, M. Ng, A. M. Orantes, E. Kinney-Lang, F. Rashid, M. Hamer, R. A. DeFazio, J. Tang, J. H. Zhang and W. J. Pearce, "Traumatic brain injury results in acute rarefication of the vascular network," *Scientific Reports,* vol. 7, p. 239, 2017.

[87] A. Salehi, A. Jullienne, M. Baghchechi, M. Hamer, M. Walsworth, V. Donovan, J. Tang, J. H. Zhang, W. J. Pearce and A. Obenaus, "Up-regulation of Wnt/β-catenin expression is accompanied with vascular repair after traumatic brain injury," *Journal of Cerebral Blood Flow and Metabolism,* vol. 38, pp. 274-289, 2018.

[88] P. Assis-Nascimento, Y. Tsenkina and D. J. Liebl, "EphB3 signaling induces cortical endothelial cell death and disrupts the blood–brain barrier after traumatic brain injury," *Cell Death and Disease,* vol. 9, p. 7, 2018.

[89] B. Lin, M. D. Ginsberg, W. Zhao, O. F. Alonso, L. Belayev and R. Busto, "Quantitative analysis of microvascular alterations in traumatic brain injury by endothelial barrier antigen immunohistochemistry," *Journal of Neurotrauma,* vol. 18, pp. 389-397, 2001.

[90] A. Muellner, M. Benz, C. U. Kloss, A. Mautes, D. Burggraf and G. F. Hamann, "Microvascular basal lamina antigen loss after traumatic brain injury in the rat," *Journal of Neurotrauma,* vol. 20, pp. 745-754, 2003.

[91] R. Morgan, C. W. Kreipke, G. Roberts , M. Bagchi and J. A. Rafols, "Neovascularization following traumatic brain injury: possible evidence for both angiogenesis and vasculogenesis," *Neurological Research,* vol. 29, pp. 375-381, 2007.

[92] S. C. Stein, X. H. Chen, G. P. Stinson and D. H. Smith, "Intravascular coagulation: a major secondary insult in nonfatal traumatic brain injury," *Journal of Neurosurgery,* vol. 97, pp. 1373-1377, 2002.

[93] C. A. Tagge, A. M. Fisher, O. V. Minaeva, A. Gaudreau-Balderrama, J. A. Moncaster, X.-L. Zhang, S. Saman, M. Ericsson, K. D. Onos, R. Veksler, V. V. Senatorov, A. Kondo, X. Z. Zhou, O. Miry, L. R. Rose, K. R. Gopaul, C. Upreti, C. J. Nowinski, R. C. Cantu, V. E. Alvarez, A. M. Hildebrandt, E. S. Franz, J. Konrad, J. A. Hamilton, N. Hua, Y. Tripodis, A. T. Anderson, G. R. Howell, D. Kaufer, G. F. Hall, K. P. Lu, R. M. Ransohoff, R. O. Cleveland, N. W. Kowall, T. D. Stein, B. T. Lamb, B. R. Huber, W. C. Moss, A. Friedman, P. K. Stanton, A. C. McKee and L. E.

Goldstein, "Concussion, microvascular injury, and early tauopathy in young athletes after impact head injury and an impact concussion mouse model," *Brain,* vol. 141, pp. 422-458, 2018.

[94] M. Daneyemez, "Microangiographic changes following cerebral contusion in rats," *Neuroscience,* vol. 92, pp. 783-790, 1999.

[95] N. Szarka, M. R. Pabbidi, K. Amrein, E. Czeiter, G. Berta, K. Pohoczky, Z. Helyes, Z. Ungvari, A. Koller, A. Buki and P. Toth, "Traumatic Brain Injury Impairs Myogenic Constriction of Cerebral Arteries: Role of Mitochondria-Derived H2O2 and TRPV4-Dependent Activation of BKCa Channels," *Journal of Neurotrauma,* vol. 35, pp. 930-939, 2018.

[96] E. M. Enevoldsen and F. T. Jensen, "Autoregulation and CO2 responses of cerebral blood flow in patients with acute severe head injury," *Journal of Neurosurgery,* vol. 48, pp. 689-703, 1978.

[97] T. C. Glenn, N. A. Martin, M. A. Horning, D. L. McArthur, D. A. Hovda, P. Vespa and G. A. Brooks, "Lactate: brain fuel in human traumatic brain injury: a comparison with normal healthy control subjects," *Journal of Neurotrauma,* vol. 32, pp. 820-832, 2015.

[98] E. P. Wei, R. J. Hamm, A. I. Baranova and J. T. Povlishock, "The long-term microvascular and behavioral consequences of experimental traumatic brain injury after hypothermic intervention," *Journal of Neurotrauma,* vol. 26, pp. 527-537, 2009.

[99] A. Lavinio, B. Ene-Iordache, I. Nodari, A. Girardini, E. Cagnazzi, F. Rasulo, P. Smielewski, M. Czosnyka and N. Latronico, "Cerebrovascular reactivity and autonomic drive following traumatic brain injury," *Acta Neurochirurgica Supplements,* vol. 102, pp. 3-7, 2008.

[100] A. Jullienne, A. Obenaus, A. Ichkova, C. Savona-Baron, W. J. Pearce and J. Badaut, "Chronic cerebrovascular dysfunction after traumatic brain injury," *Journal of Neuroscience Research,* vol. 94, pp. 609-622, 2016.

[101] J. A. Rafols, C. W. Kreipke and T. Petrov, "Alterations in cerebral cortex microvessels and the microcirculation in a rat model of traumatic brain injury: a correlative EM and laser Doppler flowmetry study," *Neurological Research,* vol. 29, pp. 339-347, 2007.

[102] A. Salehi, J. H. Zhang and A. Obenaus, "Response of the cerebral vasculature following traumatic brain injury," *Journal of Cerebral Blood Flow and Metabolism,* vol. 37, pp. 2320-2339, 2017.

[103] M. K. Sköld, C. von Gertten, A. C. Sandberg-Nordqvist, T. Mathiesen and S. Holmin, "VEGF and VEGF receptor expression after experimental brain contusion in rat," *Journal of Neurotrauma,* vol. 22, pp. 353-367, 2005.

[104] I. Siddiq, E. Park, E. Liu, S. K. Spratt, R. Surosky, G. Lee, D. Ando, M. Giedlin, G. M. Hare, M. G. Fehlings and A. J. Baker, "Treatment of traumatic brain injury using zinc-finger protein gene therapy targeting VEGF-A," *Journal of Neurotrauma,* vol. 29, pp. 2647-2659, 2012.

[105] M. A. Gama Sosa, R. De Gasperi, P. L. Janssen, F. J. Yuk, P. C. Anazodo, P. E. Pricop, A. J. Paulino, B. Wicinski, M. C. Shaughness, E. Maudlin-Jeronimo, A. A. Hall, D. L. Dickstein, R. M. McCarron, M. Chavko, P. R. Hof, S. T. Ahlers and G. A. Elder, "Selective vulnerability of the cerebral vasculature to blast injury in a rat model of mild traumatic brain injury," *Acta Neuropathologica Communications,* vol. 2, p. 67, 2014.

[106] A. Raza, M. J. Franklin and A. Z. Dudek, "Pericytes and vessel maturation during tumor angiogenesis and metastasis," *American Journal of Hematology,* vol. 85, pp. 593-598, 2010.

[107] M. Bjarnegård, M. Enge, J. Norlin, S. Gustafsdottir, S. Fredriksson, A. Abramsson, M. Takemoto, E. Gustafsson, R. Fässler and C. Betsholtz, "Endothelium-specific ablation of PDGFB leads to pericyte loss and glomerular, cardiac, and placental abnormalities," *Development,* vol. 131, pp. 1847-1857, 2004.

[108] M. Hellström, H. Gerhardt, M. Kalén, X. Li, U. Eriksson, H. Wolburg and C. Betsholtz, "Lack of pericytes leads to endothelial hyperplasia and abnormal vascular morphogenesis," *Journal of Cell Biology,* vol. 153, pp. 543-554, 2001.

[109] P. Dore-Duffy, C. Owen, R. Balabanov, S. Murphy, T. Beaumont and J. A. Rafols, "Pericyte migration from the vascular wall in response to traumatic brain injury," *Microvascular Research,* vol. 60, pp. 55-69, 2000.

[110] C. M. Zehendner, A. Sebastiani, A. Hugonnet, F. Bischoff, H. J. Luhmann and S. C. Thal, "Traumatic brain injury results in rapid pericyte loss followed by reactive pericytosis in the cerebral cortex," *Scientific Reports,* vol. 5, p. 13497, 2015.

[111] C. E. Brown, P. Li, J. D. Boyd, K. R. Delaney and T. H. Murphy, "Extensive turnover of dendritic spines and vascular remodeling in cortical tissues recovering from stroke," *The Journal of Neuroscience,* vol. 27, pp. 4101-4109, 2007.

[112] H. Sorg, C. Krueger and B. Vollmar, "Intravital insights in skin wound healing using the mouse dorsal skin fold chamber," *Journal of Anatomy,* vol. 211, pp. 810-818, 2007.

[113] B. Weber, A. L. Keller, J. Reichold and N. K. Logothetis, "The microvascular system of the striate and extrastriate visual cortex of the macaque," *Cerebral Cortex,* vol. 18, pp. 2318-2330, 2008.

[114] B. P. Chugh, Imaging Microvascular Changes Associated with Neurological Diseases (PhD Thesis), Toronto: University of Toronto, 2012.

[115] M. Y. Rennie, J. Detmar, K. J. Whiteley, J. Yang, A. Jurisicova, S. L. Adamson and J. G. Sled, "Vessel tortuousity and reduced vascularization in the fetoplacental arterial tree after maternal exposure to polycyclic aromatic hydrocarbons," *American Journal of Physiology Heart Circulatory Physiology,* vol. 300, pp. H675-H684, 2011.

[116] F. Helmchen and W. Denk, "Deep tissue two-photon microscopy," *Nature Methods,* vol. 2, pp. 932-940, 2005.

[117] P. Theer, M. T. Hasan and W. Denk, "Two-photon imaging to a depth of 1000 µm in living brains by use of a Ti:Al2O3 regenerative amplifier," *Optics Letters,* vol. 28, pp. 1022-1024, 2003.

[118] K. Becker , N. Jährling, S. Saghafi, R. Weiler and H. U. Dodt, "Chemical clearing and dehydration of GFP expressing mouse brains," *PLOS One,* vol. 7, p. e33916, 2012.

[119] A. Li, H. Gong, B. Zhang, Q. Wang, C. Yan, J. Wu, Q. Liu, S. Zeng and Q. Luo, "Micro-optical sectioning tomography to obtain a high-resolution atlas of the mouse brain," *Science,* vol. 330, pp. 1404-1408, 2010.

[120] S. Xue, H. Gong, T. Jiang, W. Luo, Y. Meng, Q. Liu, S. Chen and A. Li, "India-ink perfusion based method for reconstructing continuous vascular networks in whole mouse brain," *PLOS One,* vol. 9, p. e88067, 2014.

[121] W. Denk and H. Horstmann, "Serial block-face scanning electron microscopy to reconstruct three-dimensional tissue nanostructure," *PLOS Biology,* vol. 2, p. e329, 2004.

[122] P. S. Tsai , B. Friedman, A. I. Ifarraguerri, B. D. Thompson, V. Lev-Ram, C. B. Schaffer, Q. Xiong, R. Y. Tsien, J. A. Squier and D. Kleinfeld, "All-optical histology using ultrashort laser pulses," *Neuron,* vol. 39, pp. 27-41, 2003.

[123] K. S. Hendrich, P. M. Kochanek, D. S. Williams, J. K. Schiding, D. W. Marion and C. Ho, "Early perfusion after controlled cortical impact in rats: quantification by arterial spin-labeled MRI and the influence of spin-lattice relaxation time heterogeneity," *Magnetic Resonance in Medicine,* vol. 42, pp. 673-681, 1999.

[124] L. M. Foley, T. K. Hitchens, P. M. Kochanek, J. A. Melick, E. K. Jackson and C. Ho, "Murine orthostatic response during prolonged vertical studies: effect on cerebral blood flow measured by arterial spin-labeled MRI," *Magnetic Resonance in Medicine,* vol. 54, pp. 798-806, 2005.

[125] L. S. Cahill, L. M. Gazdzinski, A. K. Tsui, Y. Q. Zhou, S. Portnoy, E. Liu, C. D. Mazer, G. M. Hare, A. Kassner and J. G. Sled, "Functional and anatomical evidence of cerebral tissue hypoxia in young sickle cell anemia mice," *Journal of Cerebral Blood Flow and Metabolism,* vol. 37, pp. 994-1005, 2017.

[126] L. Hirschler, L. P. Munting , A. Khmelinskii, W. M. Teeuwisse, E. Suidgeest, J. M. Warnking, L. van der Weerd, E. L. Barbier and M. J. van Osch, "Transit time mapping in the mouse brain using time-encoded pCASL," *NMR in Biomedicine,* vol. 31, p. e3855, 2018.

[127] L. M. Parkes, "Quantification of cerebral perfusion using arterial spin labeling: two-compartment models," *Journal of Magnetic Resonance Imaging,* vol. 22, pp. 732-736, 2005.

[128] F. Sorond, N. K. Hollenberg, L. P. Panych and N. D. Fisher, "Brain blood flow and velocity: Correlations between magnetic resonance imaging and transcranial Doppler," *Journal of Ultrasound in Medicine,* vol. 29, pp. 1017-1022, 2010.

[129] T. Uppal and R. Mogra, "RBC motion and the basis of ultrasound Doppler instrumentation," *Australasian Journal of Ultrasound in Medicine,* vol. 13, pp. 32-34, 2010.

[130] R. S. Cobbold, Foundations of Biomedical Ultrasound, New York, New York: Oxford University Press, 2007.

[131] H. S. Markus, "Transcranial Doppler ultrasound," *Journal of Neurology Neurosurgery & Psychiatry,* vol. 67, pp. 135-137, 1999.

[132] S. Sarkar, S. Ghosh, S. K. Ghosh and A. Collier, "Role of transcranial Doppler ultrasonography in stroke," *Postgraduate Medical Journal,* vol. 83, pp. 683-689, 2007.

[133] A. Ghorbani, M. J. Ahmadi and H. Shemshaki, "The value of transcranial Doppler derived pulsatility index for diagnosing cerebral small-vessel disease," *Advanced Biomedical Research,* vol. 4, p. 54, 2015.

[134] L. M. McCowan, B. M. Mullen and K. Ritchie, "Umbilical artery flow velocity waveforms and the placental vascular bed," *American Journal of Obstetrics and Gynecology,* vol. 157, pp. 900-902, 1987.

[135] E. Michel and B. Zernikow, "Gosling's Doppler pulsatility index revisited," *Ultrasound in Medicine & Biology,* vol. 24, pp. 597-599, 1998.

[136] R. B. Panerai, "The critical closing pressure of the cerebral circulation," *Medical Engineering and Physics,* vol. 25, pp. 621-632, 2003.

[137] C. Puppo, J. Camacho, G. V. Varsos, B. Yelicich, H. Gómez, L. Moraes, A. Biestro and M. Czosnyka, "Cerebral Critical Closing Pressure: Is the Multiparameter Model Better Suited to Estimate Physiology of Cerebral Hemodynamics?," *Neurocritical Care,* vol. 25, pp. 446-454, 2016.

[138] M. Czosnyka, H. K. Richards, H. E. Whitehouse and J. D. Pickard, "Relationship between transcranial Doppler-determined pulsatility index and cerebrovascular resistance: an experimental study," *Journal of Neurosurgery,* vol. 84, pp. 79-84, 1996.

[139] A. Rahman , Detection of Placental Pathology Based on Umbilical Artery Wave Mechanics (MSc Thesis), Toronto: University of Toronto, 2016.

[140] C. J. Hartley, A. K. Reddy, S. Madala, M. L. Entman, L. H. Michael and G. E. Taffet, "Doppler velocity measurements from large and small arteries in mice," *American Journal of Physiology Heart and Circulatory Physiology,* vol. 301, pp. H269-H278, 2011.

[141] N. Westerhof, P. Sipkema, G. C. van den Bos and G. Elzinga, "Forward and backward waves in the arterial system," *Cardiovascular Research,* vol. 6, pp. 648-656, 1972.

[142] W. R. Milnor, Hemodynamics, Baltimore: Williams & Wilkins, 1982.

[143] S. Vulliémoz, N. Stergiopulos and R. Meuli, "Estimation of local aortic elastic properties with MRI," *Magnetic Resonance in Medicine,* vol. 47, pp. 649-654, 2002.

[144] L. S. Cahill, Y. Q. Zhou, J. Hoggarth, L. X. Yu, A. Rahman, G. Stortz, C. L. Whitehead, A. Baschat, J. C. Kingdom, C. K. Macgowan, L. Serghides and J. G. Sled, "Placental vascular abnormalities in the mouse alter umbilical artery wave reflections," *American Journal of Physiology Heart and Circulatory Physiology,* vol. 316, pp. H664-H672, 2019.

[145] P. Segers, E. R. Rietzschel, M. L. De Buyzere, S. J. Vermeersch, D. De Bacquer, L. M. Van Bortel, G. De Backer, T. C. Gillebert and P. R. Verdonck, "Noninvasive (input) impedance, pulse wave velocity, and wave reflection in healthy middle-aged men and women," *Hypertension,* vol. 49, pp. 1248-1255, 2007.

[146] M. R. Graham, P. Evans, B. Davies and J. S. Baker, "Arterial pulse wave velocity, inflammatory markers, pathological GH and IGF states, cardiovascular and cerebrovascular disease," *Vascular Health and Risk Management,* vol. 4, pp. 1361-1371, 2008.

[147] C. Li, H. Xiong, S. Pirbhulal, D. Wu, Z. Li, W. Huang, H. Zhang and W. Wu, "Heart-carotid pulse wave velocity a useful index of atherosclerosis in Chinese hypertensive patients," *Medicine (Baltimore),* vol. 94, p. e2343, 2015.

[148] A. C. Clevenger, T. Kilbaugh and S. S. Margulies, "Carotid artery blood flow decreases after rapid head rotation in piglets," *Journal of Neurotrauma,* vol. 32, pp. 120-126, 2015.

[149] O. Chaiwat, D. Sharma, Y. Udomphorn, W. M. Armstead and M. S. Vavilala, "Cerebral hemodynamic predictors of poor 6-Month Glasgow Outcome Score in severe pediatric traumatic brain injury," *Journal of Neurotrauma,* vol. 26, pp. 657-663, 2009.

[150] T. K. Len, P. J. Neary, G. J. Asmundson, D. G. Goodman, B. Bjornson and Y. N. Bhambhani, "Cerebrovascular reactivity impairment after sport-induced concussion," *Medicine & Science in Sports & Exercise,* vol. 43, pp. 2241-2248, 2011.

[151] T. K. Len, J. P. Neary, G. J. Asmundson, D. G. Candow, D. G. Goodman, B. Bjornson and Y. N. Bhambhani, "Serial monitoring of CO2 reactivity following sport concussion using hypocapnia and hypercapnia," *Brain Injury,* vol. 27, pp. 346-353, 2013.

[152] N. A. Martin, R. V. Patwardhan, M. J. Alexander, C. Z. Africk, J. H. Lee, E. Shalmon, D. A. Hovda and D. P. Becker, "Characterization of cerebral hemodynamic phases following severe head trauma: hypoperfusion, hyperemia, and vasospasm," *Journal of Neurosurgery,* vol. 87, pp. 9-19, 1997.

[153] N. A. Martin, C. Doberstein, C. Zane, M. J. Caron, K. Thomas and D. P. Becker, "Posttraumatic cerebral arterial spasm: transcranial Doppler ultrasound, cerebral blood flow, and angiographic findings," *Journal of Neurosurgery,* vol. 77, pp. 575-583, 1992.

[154] C. M. Thibeault, S. Thorpe, M. J. O'Brien, N. Canac, M. Ranjbaran, I. Patanam, A. Sarraf, J. LeVangie, F. Scalzo, S. J. Wilk, R. Diaz-Arrastia and R. B. Hamilton, "A Cross-Sectional Study on

Cerebral Hemodynamics After Mild Traumatic Brain Injury in a Pediatric Population," *Frontiers in Neurology,* vol. 9, p. 200, 2018.

[155] B. K. Prasad, M. Chamarthi and P. Isireddy, "Role of Transcranial Doppler as a Predictor of Prognosis in Patients with Traumatic Brain Injury," *International Journal of Contemporary Medicine Surgery and Radiology,* vol. 2, pp. 139-142, 2017.

[156] C. Zweifel, M. Czosnyka, E. Carrera, N. de Riva, J. D. Pickard and P. Smielewski, "Reliability of the blood flow velocity pulsatility index for assessment of intracranial and cerebral perfusion pressures in head-injured patients," *Neurosurgery,* vol. 71, pp. 853-861, 2012.

[157] N. de Riva, K. P. Budohoski, P. Smielewski, M. Kasprowicz, C. Zweifel, L. A. Steiner, M. Reinhard, N. Fábregas, J. D. Pickard and M. Czosnyka, "Transcranial doppler pulsatility index: what it is and what it isn't," *Neurocritical Care,* vol. 17, pp. 58-66, 2012.

[158] J. Steinman, M. M. Koletar, B. Stefanovic and J. G. Sled, "3D morphological analysis of the mouse cerebral vasculature: Comparison of in vivo and ex vivo methods," *PLOS One,* vol. 12, p. e0186676, 2017.

[159] O. C. Suter, T. Sunthorn, R. Kraftsik, J. Straubel, P. Darekar, K. Khalili and J. Miklossy, "Cerebral hypoperfusion generates cortical watershed microinfarcts in Alzheimer disease," *Stroke,* vol. 33, pp. 1986-1992, 2002.

[160] N. Schuff, S. Matsumoto, J. Kmiecik, C. Studholme, A. Du, F. Ezekiel, B. L. Miller, J. H. Kramer, W. J. Jagust, H. C. Chui and M. W. Weiner, "Cerebral blood flow in ischemic vascular dementia and Alzheimer's disease, measured by arterial spin-labeling magnetic resonance imaging," *Alzheimer's & Dementia,* vol. 5, pp. 454-462, 2009.

[161] W. R. Brown and C. R. Thore, "Review: cerebral microvascular pathology in ageing and neurodegeneration," *Neuropathology and Applied Neurobiology,* vol. 37, pp. 56-74, 2011.

[162] S. Hirsch, J. Reichold, M. Schneider, G. Székely and B. Weber , "Topology and hemodynamics of the cortical cerebrovascular system," *Journal of Cerebral Blood Flow and Metabolism,* vol. 32, pp. 952-967, 2012.

[163] T. W. Secomb, R. Hsu, N. B. Beamer and B. M. Coull, "Theoretical simulation of oxygen transport to brain by networks of microvessels: effects of oxygen supply and demand on tissue hypoxia," *Microcirculation,* vol. 7, pp. 237-247, 2000.

[164] P. B. Gorelick et al., "Vascular contributions to cognitive impairment and dementia: a statement for healthcare professionals from the American Hear Association/American Stroke Association," *Stroke,* vol. 42, pp. 2672-2713, 2011.

[165] H. Hama, H. Kurokawa , H. Kawano, R. Ando, T. Shimogori, H. Noda, A. Sakaue-Sawano and A. Miyawaki, "Scale: a chemical approach for fluorescence imaging and reconstruction of transparent mouse brain," *Nature Neuroscience,* vol. 14, pp. 1481-1488, 2011.

[166] J. P. Lerch, J. B. Carroll, A. Dorr, S. Spring, A. C. Evans, M. R. Hayden, J. G. Sled and R. M. Henkelman, "Cortical thickness measured from MRI in the YAC128 mouse model of Huntington's disease," *NeuroImage,* vol. 41, pp. 243-251, 2008.

[167] A. J. Moy, M. P. Wiersma and B. Choi, "Optical histology: a method to visualize microvasculature in thick tissue sections of mouse brain," *PLOS One,* vol. 8, p. e53753, 2013.

[168] A. Ertürk, C. P. Mauch, F. Hellal, F. Förstner, T. Keck, K. Becker, N. Jährling, H. Steffens, M. Richter, M. Hübener, E. Kramer, F. Kirchhoff, H. U. Dodt and F. Bradke, "Three-dimensional

imaging of the unsectioned adult spinal cord to assess axon regeneration and glial responses after injury," *Nature Medicine,* vol. 18, pp. 166-171, 2012.

[169] M. T. Ke, S. Fujimoto and T. Imai, "SeeDB: a simple and morphology-preserving optical clearing agent for neuronal circuit reconstruction," *Nature Neuroscience,* vol. 16, pp. 1154-1161, 2013.

[170] K. Masamoto, H. Takuwa, C. Seki, J. Taniguchi, Y. Itoh, Y. Tomita, H. Toriumi, M. Unekawa, H. Kawaguchi, H. Ito, N. Suzuki and I. Kanno, "Microvascular sprouting, extension, and creation of new capillary connections with adaptation of the neighboring astrocytes in adult mouse cortex under chronic hypoxia," *Journal of Cerebral Blood Flow and Metabolism,* vol. 34, pp. 325-331, 2014.

[171] M. Emmenlauer, O. Ronneberger, A. Ponti, P. Schwarb, A. Griffa, A. Filippi, R. Nitschke, W. Driever and H. Burkhardt, "XuvTools: free, fast and reliable stitching of large 3D datasets," *Journal of Microscopy,* vol. 233, pp. 42-60, 2009.

[172] Y. Fridman, S. M. Pizer, S. Aylward and E. Bullitt, "Extracting branching tubular object geometry via cores," *Medical Image Analysis,* vol. 8, pp. 169-176, 2004.

[173] P. Coupe, P. Yger, S. Prima, P. Hellier, C. Kervrann and C. Barillot, "An optimized blockwise nonlocal means denoising filter for 3-D magnetic resonance images," *IEEE Transactions on Medical Imaging,* vol. 27, pp. 425-441, 2008.

[174] F. L. Bookstein, "Principal warps: thin-plate splines and the decomposition of deformations," *IEEE Transactions on Pattern Analysis and Machine Intelligence,* vol. 11, pp. 567-585, 1989.

[175] F. Lauwers, F. Cassot, V. Lauwers-Cances, P. Puwanarajah and H. Duvernoy, "Morphometry of the human cerebral cortex microcirculation: general characteristics and space-related profiles," *NeuroImage,* vol. 39, pp. 936-948, 2008.

[176] L. Risser, F. Plouraboue, P. Cloetens and C. Fonta, "A 3D-investigation shows that angiogenesis in primate cerebral cortex mainly occurs at capillary level," *International Journal of Developmental Neuroscience,* vol. 27, pp. 185-196, 2009.

[177] H. M. Duvernoy, S. Delon and J. L. Vannson, "Cortical blood vessels of the human brain," *Brain Research Bulletin,* vol. 7, pp. 519-579, 1981.

[178] K. A. Kasischke, E. M. Lambert, B. Panepento, A. Sun, H. A. Gelbard, R. W. Burgess, T. H. Foster and M. Nedergaard, "Two-photon NADH imaging exposes boundaries of oxygen diffusion in cortical vascular supply regions," *Journal of Cerebral Blood Flow and Metabolism,* vol. 31, pp. 68-81, 2011.

[179] D. Kobat , M. E. Durst, N. Nishimura, A. W. Wong, C. B. Schaffer and C. Xu, "Deep tissue multiphoton microscopy using longer wavelength excitation," *Optics Express,* vol. 17, pp. 13354-13364, 2009.

[180] F. Haiss, R. Jolivet, M. T. Wyss, J. Reichold, N. B. Braham, F. Scheffold, M. P. Krafft and B. Weber, "Improved in vivo two-photon imaging after blood replacement by perfluorocarbon," *The Journal of Physiology,* vol. 587, pp. 3153-3158, 2009.

[181] W. S. Cleveland and S. J. Devlin, "Locally weighted regression: An approach to regression analysis by local fitting," *Journal of the American Statistical Association,* vol. 83, pp. 596-610, 1988.

[182] Y. Sekiguchi, H. Takuwa, H. Kawaguchi, T. Kikuchi, E. Okada, I. Kanno, H. Ito, Y. Tomita, Y. Itoh, N. Suzuki, R. Sudo, K. Tanishita and K. Masamoto, "Pial arteries respond earlier than penetrating arterioles to neural activation in the somatosensory cortex in awake mice exposed to chronic hypoxia: an additional mechanism to proximal integration signaling?," *Journal of Cerebral Blood Flow and Metabolism,* vol. 34, pp. 1761-1770, 2014.

[183] M. Choi, T. Ku, K. Chong, J. Yoon and C. Choi, "Minimally invasive molecular delivery into the brain using optical modulation of vascular permeability," *PNAS,* vol. 108, pp. 9256-9261, 2011.

[184] B. Minnich and A. Lametschwandtner, "Lengths measurements in microvascular corrosion castings: two-dimensional versus three-dimensional morphometry," *Scanning,* vol. 22, pp. 173-177, 2000.

[185] H. U. Dodt, U. Leischner, A. Schierloh, N. Jährling, C. P. Mauch, K. Deininger, J. M. Deussing, M. Eder, W. Zieglgänsberger and K. Becker, "Ultramicroscopy: three-dimensional visualization of neuronal networks in the whole mouse brain," *Nature Methods,* vol. 4, pp. 331-336, 2007.

[186] C. J. Engelbrecht and E. H. Stelzer, "Resolution enhancement in a light-sheet-based microscope (SPIM)," *Optics Letters,* vol. 31, pp. 1477-1479, 2006.

[187] M. Stefaniuk, E. J. Gualda, M. Pawlowska, D. Legutko, P. Matryba, P. Koza, W. Konopka, D. Owczarek, M. Wawryniak, P. Loza-Alvarez and L. Kaczmarek, "Light-sheet microscopy imaging of a whole cleared rat brain with Thy1-GFP transgene," *Scientific Reports,* vol. 6, p. 28209, 2016.

[188] L. Silvestri, A. Bria, L. Sacconi, G. Iannello and F. S. Pavone, "Confocal light sheet microscopy: micron-scale neuroanatomy of the entire mouse brain," *Optics Express,* vol. 20, pp. 20582-20598, 2012.

[189] D. A. Tata and B. J. Anderson, "A new method for the investigation of capillary structure," *Journal of Neuroscience Methods,* vol. 113, pp. 199-206, 2002.

[190] B. T. Altura and B. M. Altura, "Effects of barbiturates, phencyclidine, ketamine and analogs on cerebral circulation and cerebrovascular muscle," *Microcirculation, Endothelium, and Lymphatics,* vol. 1, pp. 169-184, 1984.

[191] S. Tetrault, O. Chever, A. Sik and F. Amzica, "Opening of the blood-brain barrier during isoflurane anaesthesia," *European Journal of Neuroscience,* vol. 28, pp. 1330-1341, 2008.

[192] Z. L. Brookes, C. S. Reilly and N. J. Brown, "Differential effects of propofol, ketamine, and thiopental anaesthesia on the skeletal muscle microcirculation of normotensive and hypertensive rats in vivo," *British Journal of Anaesthesia,* vol. 93, pp. 249-256, 2004.

[193] Y. R. Gao, S. E. Greene and P. J. Drew, "Mechanical restriction of intracortical vessel dilation by brain tissue sculpts the hemodynamic response," *NeuroImage,* vol. 115, pp. 162-176, 2015.

[194] R. M. Navari, E. P. Wei, H. A. Kontos and J. L. Patterson, "Comparison of the open skull and cranial window preparations in the study of the cerebral microcirculation," *Microvascular Research,* vol. 16, pp. 304-315, 1978.

[195] E. F. Hauck, S. Apostel, J. F. Hoffmann, A. Heimann and O. Kempski, "Capillary flow and diameter changes during reperfusion after global cerebral ischemia studied by intravital video microscopy," *Journal of Cerebral Blood Flow and Metabolism,* vol. 24, pp. 383-391, 2004.

[196] A. Roggan, M. Friebel, K. Doerschel, A. Hahn and G. J. Mueller, "Optical properties of circulating human blood in the wavelength range 400-2500 nm," *Journal of Biomedical Optics,* vol. 1999, pp. 36-46, 1999.

[197] J. Steinman, M. Koletar, B. Stefanovic and J. G. Sled, "Comparison of in vivo and ex vivo imaging of the microvasculature with 2-photon fluorescence microscopy," *SPIE BiOS,* p. 97121V, 2016.

[198] J. Steinman, L. S. Cahill, M. M. Koletar, B. Stefanovic and J. G. Sled, "Acute and chronic stage adaptations of vascular architecture and cerebral blood flow in a mouse model of TBI," *bioRxiv,* 2018.

[199] J. Steinman, L. S. Cahill, M. M. Koletar , B. Stefanovic and J. G. Sled, "Acute and chronic stage adaptations of vascular architecture and cerebral blood flow in a mouse model of TBI," *NeuroImage,* vol. 202, p. 116101, 2019.

[200] U. W. Thomale, S. N. Kroppenstedt, T. F. Beyer, K. D. Schaser, A. W. Unterberg and J. F. Stover, "Temporal profile of cortical perfusion and microcirculation after controlled cortical impact injury in rats," *Journal of Neurotrauma,* vol. 19, pp. 403-413, 2002.

[201] S. P. Amato, F. Pan, J. Schwartz and T. M. Ragan, "Whole Brain Imaging with Serial Two-Photon Tomography," *Frontiers in Neuroanatomy,* vol. 10, p. 31, 2016.

[202] A. Dorr, L. A. Thomason, M. M. Koletar, I. L. Joo, J. Steinman, L. S. Cahill, J. G. Sled and B. Stefanovic, "Effects of voluntary exercise on structure and function of cortical microvasculature," *Journal of Cerebral Blood Flow and Metabolism,* vol. 37, pp. 1046-1059, 2017.

[203] T. Motoike, S. Loughna, E. Perens, B. L. Roman, W. Liao, T. C. Chau, C. D. Richardson, T. Kawate, J. Kuno, B. M. Weinstein, D. Y. Stainier and T. N. Sato, "Universal GFP reporter for the study of vascular development," *Genesis,* vol. 28, pp. 75-81, 2000.

[204] A. W. Unterberg, R. Stroop, U. W. Thomale, K. L. Kiening, S. Päuser and W. Vollmann, "Characterisation of brain edema following "controlled cortical impact injury" in rats," *Acta Neurochirurgica Supplement,* vol. 70, pp. 106-108, 1997.

[205] L. S. Cahill, C. L. Laliberté, J. Ellegood, S. Spring, J. A. Gleave, M. C. van Eede, J. P. Lerch and R. M. Henkelman, "Preparation of fixed mouse brains for MRI," *NeuroImage,* vol. 60, pp. 933-939, 2012.

[206] J. Dazai, S. Spring, L. S. Cahill and R. M. Henkelman, "Multiple-mouse Neuroanatomical Magnetic Resonance Imaging," *Journal of Visualized Experiments,* vol. 48, p. e2497, 2011.

[207] T. L. Spencer Noakes, R. M. Henkelman and B. J. Nieman, "Partitioning k-space for cylindrical three-dimensional rapid acquisition with relaxation enhancement imaging in the mouse brain," *NMR in Biomedicine,* vol. 30, 2017.

[208] S. Preibisch, S. Saalfeld and P. Tomancak, "Globally optimal stitching of tiled 3D microscopic image acquisitions," *Bioinformatics,* vol. 25, pp. 1463-1465, 2009.

[209] T. F. Sherman, "On connecting large vessels to small. The meaning of Murray's Law.," *The Journal of General Physiology,* vol. 78, pp. 431-453, 1981.

[210] C. D. Murray, "The Physiological Principle of Minimum Work: I. The Vascular System and the Cost of Blood Volume.," *PNAS,* vol. 12, pp. 207-214, 1926.

[211] C. D. Murray, "The Physiological Principle of Minimum Work: II. Oxygen Exchange in Capillaries," *PNAS,* vol. 12, pp. 299-304, 1926.

[212] D. A. Nordsletten, S. Blackett, M. D. Bentley, E. L. Ritman and N. P. Smith, "Structural morphology of renal vasculature," *American Journal of Physiology Heart Circulatory Physiology,* vol. 291, pp. H296-H309, 2006.

[213] M. Y. Rennie, J. Detmar, K. J. Whiteley, A. Jurisicova, S. L. Adamson and J. G. Sled, "Expansion of the fetoplacental vasculature in late gestation is strain dependent in mice," *American Journal of Physiology Heart and Circulatory Physiology,* vol. 302, pp. H1261-H1273, 2012.

[214] J. T. Cole, A. Yarnell, W. S. Kean, E. Gold, B. Lewis, M. Ren, D. C. McMullen, D. M. Jacobowitz, H. B. Pollard, J. T. O'Neill, N. E. Grunberg, C. L. Dalgard, J. A. Frank and W. D. Watson, "Craniotomy: true sham for traumatic brain injury, or a sham of a sham?," *Journal of Neurotrauma,* vol. 28, pp. 359-369, 2011.

[215] N. C. Rivron, E. J. Vrij, J. Rouwkema, S. Le Gac, A. van den Berg, R. K. Truckenmüller and C. A. van Blitterswijk, "Tissue deformation spatially modulates VEGF signaling and angiogenesis," *PNAS,* vol. 109, pp. 6886-6891, 2012.

[216] R. A. Hill, L. Tong, P. Yuan, S. Murikinati, S. Gupta and J. Grutzendler, "Regional blood flow in the normal and ischemic brain is controlled by arteriolar smooth muscle cell contractility and not by capillary pericytes," *Neuron,* vol. 87, pp. 95-110, 2015.

[217] C. E. Lynch, G. Crynen, S. Ferguson, B. Mouzon, D. Paris, J. Ojo, P. Leary, F. Crawford and C. Bachmeier, "Chronic cerebrovascular abnormalities in a mouse model of repetitive mild traumatic brain injury," *Brain Injury,* vol. 30, pp. 1414-1427, 2016.

[218] K. Engelhard and C. Werner, "The effects of general anesthesia and variations in hemodynamics on cerebral perfusion," *Applied Cardiopulmonary Pathophysiology,* vol. 13, pp. 157-159, 2009.

[219] E. B. Hutchinson, B. Stefanovic , A. P. Koretsky and A. C. Silva, "Spatial flow-volume dissociation of the cerebral microcirculatory response to mild hypercapnia," *NeuroImage,* vol. 32, pp. 520-530, 2006.

[220] B. C. Fry, T. K. Roy and T. W. Secomb, "Capillary recruitment in a theoretical model for blood flow regulation in heterogeneous microvessel networks," *Physiological Reports,* vol. 1, p. e00050, 2013.

[221] U. Göbel, B. Klein, H. Schrök and W. Kuschinsky, "Lack of capillary recruitment in the brains of awake rats during hypercapnia," *Journal of Cerebral Blood Flow and Metabolism,* vol. 9, pp. 491-499, 1989.

[222] M. L. Forbes, K. S. Hendrich, P. M. Kochanek, D. S. Williams, J. K. Schiding, S. R. Wisniewski, S. F. Kelsey, S. T. DeKosky, S. H. Graham, D. W. Marion and C. Ho, "Assessment of cerebral blood flow and CO2 reactivity after controlled cortical impact by perfusion magnetic resonance

imaging using arterial spin-labeling in rats," *Journal of Cerebral Blood Flow and Metabolism,* vol. 17, pp. 865-874, 1997.

[223] L. Østergaard, T. S. Engedal, R. Aamand, R. Mikkelsen, N. K. Iversen, M. Anzabi, E. T. Næss-Schmidt, K. R. Drasbek, V. Bay, J. U. Blicher, A. Tietze, I. K. Mikkelsen, B. Hansen, S. N. Jespersen, N. Juul, J. C. Sørensen and M. Rasmussen, "Capillary transit time heterogeneity and flow-metabolism coupling after traumatic brain injury," *Journal of Cerebral Blood Flow and Metabolism,* vol. 34, pp. 1585-1598, 2014.

[224] U. Scherbel, R. Raghupathi, M. Nakamura, K. E. Saatman, J. Q. Trojanowski, E. Neugebauer, M. W. Marino and T. K. McIntosh, "Differential acute and chronic responses of tumor necrosis factor-deficient mice to experimental brain injury," *PNAS,* vol. 96, pp. 8721-8726, 1999.

[225] H. E. Holmes, N. M. Powell, D. Ma, O. Ismail, I. F. Harrison, J. A. Wells, N. Colgan, J. M. O'Callaghan, R. A. Johnson, T. K. Murray, Z. Ahmed, M. Heggenes, A. Fisher, M. J. Cardoso, M. Modat, M. J. O'Neill, E. C. Collins, E. M. Fisher, S. Ourselin and M. F. Lythgoe, "Comparison of In Vivo and Ex Vivo MRI for the Detection of Structural Abnormalities in a Mouse Model of Tauopathy," *Frontiers in Neuroinformatics,* vol. 11, p. 20, 2017.

[226] F. Clausen and L. Hillered, "Intracranial pressure changes during fluid percussion, controlled cortical impact and weight drop injury in rats," *Acta Neurochirurgica,* vol. 147, pp. 775-780, 2005.

[227] L. Krasznai and E. H. Grote, "Acute vasoparalysis after subarachnoid haemorrhage and cerebral trauma: general reflex phenomenon?," *Neurological Research,* vol. 16, pp. 40-44, 1994.

[228] A. D. Wright, J. D. Smirl, K. Bryk, S. Fraser, M. Jakovac and P. van Donkelaar, "Sport-Related Concussion Alters Indices of Dynamic Cerebral Autoregulation," *Frontiers in Neurology,* vol. 9, p. 196, 2018.

[229] A. Rahman, Y. Q. Zhou, Y. Yee, J. Dazai, L. S. Cahill, J. Kingdom, C. K. Macgowan and J. G. Sled, "Ultrasound detection of altered placental vascular morphology based on hemodynamic pulse wave reflection," *American Journal of Physiology. Heart and Circulatory Physiology,* vol. 312, pp. H1021-H1029, 2017.

[230] G. James, D. Witten, T. Hastie and R. Tibshirani, An Introduction to Statistical Learning, Springer, 2013.

[231] M. F. O'Rourke and M. G. Taylor, "Vascular Impedance of the Femoral Bed," *Circulation Research,* vol. 18, pp. 126-139, 1966.

[232] X. Robin, N. Turck, A. Hainard, N. Tiberti, F. Lisacek, J. C. Sanchez and M. Müller, "pROC: an open-source package for R and S+ to analyze and compare ROC curves," *BMC Bioinformatics,* vol. 12, p. 77, 2011.

[233] M. G. Taylor, "The input impedance of an assembly of randomly branching elastic tubes," *Biophysical Journal,* vol. 6, pp. 29-51, 1966.

[234] C. E. Dixon, G. L. Clifton, J. W. Lighthall, A. A. Yaghmai and R. L. Hayes, "A controlled cortical impact model of traumatic brain injury in the rat," *Journal of Neuroscience Methods,* vol. 39, pp. 253-262, 1991.

[235] M. Khan, H. Sakakima, T. S. Dhammu, A. Shunmugavel, Y. B. Im, A. G. Gilg, A. K. Singh and I. Singh, "S-Nitrosoglutathione reduces oxidative injury and promotes mechanisms of

neurorepair following traumatic brain injury in rats," *Journal of Neuroinflammation,* vol. 8, p. 78, 2011.

[236] M. Dobrzeniecki, A. Trofimov and D. E. Bragin, "Cerebral arterial compliance in traumatic brain injury," *Acta Neurochirurgica. Supplement.,* vol. 126, pp. 21-24, 2018.

[237] S. Laxminarayan, R. Laxminarayan, G. J. Langewouters and A. V. Vos, "Computing total arterial compliance of the arterial system from its input impedance," *Medical & Biological Engineering & Computing,* vol. 17, pp. 623-628, 1979.

[238] D. J. Farrar, H. D. Green, M. G. Bond, W. D. Wagner and R. A. Gobbee, "Aortic pulse wave velocity, elasticity, and composition in a nonhuman primate model of atherosclerosis," *Circulation Research,* vol. 43, pp. 52-62, 1978.

[239] D. H. Bergel, "The static elastic properties of the arterial wall," *The Journal of Physiology,* vol. 156, pp. 445-457, 1961.

[240] K. L. Monson, M. I. Converse and G. T. Manley, "Cerebral blood vessel damage in traumatic brain injury," *Clinical Biomechanics (Bristol, Avon),* 2018.

[241] K. S. Wong, H. Li, Y. L. Chan, A. Ahuja, W. W. Lam , A. Wong and R. Kay, "Use of transcranial Doppler ultrasound to predict outcome in patients with intracranial large-artery occlusive disease," *Stroke,* vol. 31, pp. 2641-2647, 2000.

[242] K. Reuter-Rice, "Transcranial Doppler Ultrasound Use in Pediatric Traumatic Brain Injury," *Journal of Radiology Nursing,* vol. 36, pp. 3-9, 2017.

[243] P. Bouzat, L. Almeras, P. Manhes, L. Sanders, A. Levrat, J. S. David, R. Cinotti, R. Chabanne, A. Gloaguen, X. Bobbia, S. Thoret, L. Oujamaa, J. L. Bosson, J. F. Payen, K. Asehnoune, P. Pes, J. Y. Lefrant, S. Mirek, F. Albasini, C. Scrimgeour, J. M. Thouret, F. Chartier, M. Ginet and TBI-TCD Study Investigators, "Transcranial Doppler to Predict Neurologic Outcome After Mild to Moderate Traumatic Brain Injury," *Anesthesiology,* vol. 125, pp. 346-354, 2016.

[244] R. Williams, A. Needles, E. Cherin, Y. Q. Zhou, R. M. Henkelman, S. L. Adamson and F. S. Foster, "Noninvasive ultrasonic measurement of regional and local pulse-wave velocity in mice," *Ultrasound in Medicine & Biology,* vol. 33, pp. 1368-1375, 2007.

[245] P. Segers, A. Swillens, L. Taelman and J. Vierendeels, "Wave reflection leads to over- and underestimation of local wave speed by the PU- and QA-loop methods: theoretical basis and solution to the problem," *Physiological Measurement,* vol. 35, pp. 847-861, 2014.

[246] L. S. Cahill, J. Pilmeyer, L. X. Yu, J. Steinman, G. M. Hare, A. Kassner, C. K. Macgowan and J. G. Sled, "Ultrasound detection of abnormal cerebrovascular morphology in a mouse model of sickle cell disease based on wave reflection," *Ultrasound in Medicine & Biology,* vol. 45, pp. 3269-3278, 2019.

[247] N. Karamzadeh, F. Amyot, K. Kenney, A. Anderson, F. Chowdhry, H. Dashtestani, E. M. Wassermann, V. Chernomordik, C. Boccara, E. Wegman, R. Diaz-Arrastia and A. H. Gandjbakche, "A machine learning approach to identify functional biomarkers in human prefrontal cortex for individuals with traumatic brain injury using functional near-infrared spectroscopy," *Brain and Behavior,* vol. 6, p. e00541, 2016.

[248] R. W. Thatcher, D. M. North, R. T. Curtin, R. A. Walker, C. J. Biver, J. F. Gomez and A. M. Salazar, "An EEG severity index of traumatic brain injury," *The Journal of Neuropsychiatry and Clinical Neurosciences,* vol. 13, pp. 77-87, 2001.

[249] F. Amyot, D. B. Arciniegas, M. P. Brazaitis, K. C. Curley, R. Diaz-Arrastia, A. Gandjbakhche, P. Herscovitch, S. R. Hinds, G. T. Manley, A. Pacifico, A. Razumovsky, J. Riley, W. Salzer, R. Shih, J. G. Smirniotopoulos and D. Stocker, "A Review of the Effectiveness of Neuroimaging Modalities for the Detection of Traumatic Brain Injury," *Journal of Neurotrauma,* vol. 32, pp. 1693-1721, 2015.

[250] M. N. Economo, N. G. Clack, L. D. Lavis, C. R. Gerfen, K. Svoboda, E. W. Myers and J. Chandrashekar, "A platform for brain-wide imaging and reconstruction of individual neurons," *eLIFE,* vol. 5, p. e10566, 2016.

[251] S. Lorthois, F. Cassot and F. Lauwers, "Simulation study of brain blood flow regulation by intra-cortical arterioles in an anatomically accurate large human vascular netowrk: Part I: Methodology and baseline flow," *NeuroImage,* vol. 54, pp. 1031-1042, 2011.

[252] S. Lorthois, F. Cassot and F. Lauwers , "Simulation study of brain blood flow regulation by intra-cortical arterioles in an anatomically accurate large human vascular network. Part II: flow variations induced by global or localized modifications of arteriolar diameters," *NeuroImage,* vol. 54, pp. 2840-2853, 2011.

[253] J. P. Kaufhold, P. S. Tsai, P. Blinder and D. Kleinfeld, "Vectorization of optically sectioned brain microvasculature: Learning aids completion of vascular graphs by connecting gaps and deleting open-ended segments," *Medical Image Analysis,* vol. 16, pp. 1241-1258, 2012.

[254] Y. Gandica, T. Schwarz, O. Oliveira and R. D. Travasso, "Hypoxia in vascular networks: A complex system approach to unravel the diabetic paradox," *PLOS One,* vol. 9, p. e113165, 2014.

[255] R. S. Chadwick, "Asymptotic analysis of Stokes flow in a tortuous vessel," *Quarterly of Applied Mathematics,* vol. 43, pp. 325-336, 1985.

[256] D. N. Ku, "Blood Flow in Arteries," *Annual Review of Fluid Mechanics,* vol. 29, pp. 399-434, 1997.

[257] H. Mao, L. Zhang, K. H. Yang and A. I. King, "Application of a finite element model of the brain to study traumatic brain injury mechanisms in the rat," *Stapp Car Crash Journal,* vol. 50, pp. 583-600, 2006.

[258] H. Mao, X. Jin, L. Zhang, K. H. Yang, T. Igarashi, L. J. Noble-Haeusslein and A. I. King, "Finite element analysis of controlled cortical impact-induced cell loss," *Journal of Neurotrauma,* vol. 27, pp. 877-888, 2010.

[259] R. J. Fijalkowski, B. D. Stemper, F. A. Pintar, N. Yoganandan, M. J. Crowe and T. A. Gennarelli, "New rat model for diffuse brain injury using coronal plane angular acceleration," *Journal of Neurotrauma,* vol. 24, pp. 1387-1398, 2007.

[260] D. F. Meaney and D. H. Smith, "Biomechanics of concussion," *Clinics in Sports Medicine,* vol. 30, pp. 19-31, 2011.

[261] H. van Praag, "Exercise and the brain: something to chew on," *Trends in Neurosciences,* vol. 32, pp. 283-290, 2009.

[262] C. H. Hillman, K. I. Erickson and A. F. Kramer, "Be smart, exercise your heart: exercise effects on brain and cognition," *Nature Reviews Neuroscience,* vol. 9, pp. 58-65, 2008.

[263] M. Guo, V. Lin, W. Davis, T. Huang, A. Carranza, S. Sprague, R. Reyes, D. Jimenez and Y. Ding, "Preischemic induction of TNF-alpha by physical exercise reduces blood-brain barrier dysfunction in stroke," *Journal of Cerebral Blood Flow and Metabolism,* vol. 28, pp. 1422-1430, 2008.

[264] G. S. Griesbach, D. A. Hovda, F. Gomez-Pinilla and R. L. Sutton, "Voluntary exercise or amphetamine treatment, but not the combination, increases hippocampal brain-derived neurotrophic factor and synapsin I following cortical contusion injury in rats," *Neuroscience,* vol. 154, pp. 530-540, 2008.

[265] C. W. Cotman, N. C. Berchtold and L. A. Christie, "Exercise builds brain health: key roles of growth factor cascades and inflammation," *Trends in Neurosciences,* vol. 30, pp. 464-472, 2007.

[266] A. C. Pereira, D. E. Huddleston, A. M. Brickman, A. A. Sosunov, R. Hen, G. M. McKhann, R. Sloan, F. H. Gage, T. R. Brown and S. A. Small, "An in vivo correlate of exercise-induced neurogenesis in the adult dentate gyrus," *PNAS,* vol. 104, pp. 5638-5643, 2007.

[267] H. van Praag, T. Shubert, C. Zhao and F. H. Gage, "Exercise enhances learning and hippocampal neurogenesis in aged mice," *The Journal of Neuroscience,* vol. 25, pp. 8680-8685, 2005.

[268] T. D. Palmer, A. W. Willhoite and F. H. Gage, "Vascular niche for adult hippocampal neurogenesis," *The Journal of Comparative Neurology,* vol. 425, pp. 479-494, 2000.

[269] Y. H. Ding, J. Li, Y. Zhou, J. A. Rafols, J. C. Clark and Y. Ding, "Cerebral angiogenesis and expression of angiogenic factors in aging rats after exercise," *Current Neurovascular Research,* vol. 3, pp. 15-23, 2006.

[270] J. E. Black, K. R. Isaacs, B. J. Anderson, A. A. Alcantara and W. T. Greenough, "Learning causes synaptogenesis, whereas motor activity causes angiogenesis, in cerebellar cortex of adult rats," *PNAS,* vol. 87, pp. 5568-5572, 1990.

[271] K. Tang, F. C. Xia, P. D. Wagner and E. C. Breen, "Exercised-induced VEGF transcriptional activation in brain, lung and skeletal muscle," *Respiratory Physiology & Neurobiology,* vol. 170, pp. 16-22, 2010.

[272] K. Jin, Y. Zhu, Y. Sun, X. O. Mao, L. Xie and D. A. Greenberg, "Vascular endothelial growth factor (VEGF) stimulates neurogenesis in vitro and in vivo," *PNAS,* vol. 99, pp. 11946-11950, 2002.

[273] K. L. Jin, X. O. Mao and D. A. Greenberg, "Vascular endothelial growth factor: Direct neuroprotective effect in in vitro ischemia," *PNAS,* vol. 97, pp. 10242-10247, 2000.

[274] G. S. Griesbach, D. A. Hovda, R. Molteni, A. Wu and F. Gomez-Pinilla, "Voluntary exercise following traumatic brain injury: brain-derived neurotrophic factor upregulation and recovery of function," *Neuroscience,* vol. 125, pp. 129-139, 2004.

[275] J. L. Humm, D. A. Kozlowski, D. C. James, J. E. Gotts and T. Schallert, "Use-dependent exacerbation of brain damage occurs during an early post-lesion vulnerable period," *Brain Research,* vol. 783, pp. 286-292, 1998.

[276] C. W. Majerske, J. P. Mihalik, D. Ren, M. W. Collins, C. C. Reddy, M. R. Lovell and A. K. Wagner, "Concussion in sports: postconcussive activity levels, symptoms, and neurocognitive performance," *Journal of Athletic Training,* vol. 43, pp. 265-274, 2008.

[277] Z. G. Zhang, L. Zhang, Q. Jiang, R. Zhang, K. Davies, C. Powers, N. Bruggen and M. Chopp, "VEGF enhances angiogenesis and promotes blood-brain barrier leakage in the ischemic brain," *The Journal of Clinical Investigation,* vol. 106, pp. 829-838, 2000.

[278] M. D. Goodman, A. T. Makley, N. L. Huber, C. N. Clarke, L. A. Friend, R. M. Schuster, S. R. Bailey, S. L. Barnes, W. C. Dorlac, J. A. Johannigman, A. B. Lentsch and T. A. Pritts, "Hypobaric hypoxia exacerbates the neuroinflammatory response to traumatic brain injury," *The Journal of Surgical Research,* vol. 165, pp. 30-37, 2011.

[279] C. S. Paio, B. A. Stoica, J. Wu, B. Sabirzhanov, Z. Zhao, R. Cabatbat, D. J. Loane and A. I. Faden, "Late exercise reduces neuroinflammation and cognitive dysfunction after traumatic brain injury," *Neurobiology of Disease,* vol. 54, pp. 252-263, 2013.

[280] J. S. Pober and W. C. Sessa, "Inflammation and the blood microvascular system," *Cold Spring Harbor Perspectives in Biology,* vol. 7, p. a016345, 2015.

[281] L. S. Cahill, J. Bishop, L. M. Gazdzinski, A. Dorr, B. Stefanovic and J. G. Sled, "Altered cerebral blood flow and cerebrovascular function after voluntary exercise in adult mice," *Brain Structure and Function,* vol. 222, pp. 3395-3405, 2017.

[282] T. W. Secomb and A. R. Pries, "Microvascular plasticity: angiogenesis in health and disease. Preface.," *Microcirculation,* vol. 23, pp. 93-94, 2016.

[283] A. R. Pries and T. W. Secomb, "Making microvascular networks work: angiogenesis, remodeling, and pruning," *Physiology,* vol. 29, pp. 446-455, 2014.

[284] S. Suarez and K. Ballmer-Hofer, "VEGF transiently disrupts gap junctional communication in endothelial cells," *Journal of Cell Science,* vol. 114, pp. 1229-1235, 2001.

[285] A. R. Pries, A. J. Cornelissen, A. A. Sloot, M. Hinkeldey, M. R. Dreher, M. Höpfner, M. W. Dewhirst and T. W. Secomb, "Structural adaptation and heterogeneity of normal and tumor microvascular networks," *PLOS Computational Biology,* vol. 5, p. e1000394, 2009.

[286] A. R. Pries, M. Höpfner, F. Le Noble, M. W. Dewhirst and T. W. Secomb, "The shunt problem: control of functional shunting in normal and tumour vasculature," *Nature Reviews Cancer,* vol. 10, pp. 587-593, 2010.

[287] S. S. Nunes, H. Rekapally, C. C. Chang and J. B. Hoying, "Vessel arterial-venous plasticity in adult neovascularization," *PLOS One,* vol. 6, p. e27332, 2011.

[288] R. Harb, C. Whiteus, C. Freitas and J. Grutzendler, "In vivo imaging of cerebral microvascular plasticity from birth to death," *Journal of Cerebral Blood Flow and Metabolism,* vol. 33, pp. 146-156, 2012.

[289] M. Lasch, K. Nekolla, A. H. Klemm, J. I. Buchheim, U. Pohl, S. Dietzel and E. Deindl, "Estimating hemodynamic shear stress in murine peripheral collateral arteries by two-photon line scanning," *Molecular and Cellular Biochemistry,* vol. 453, pp. 41-51, 2019.

[290] A. R. Pries, B. Reglin and T. W. Secomb, "Modeling of angioadaptation: insights for vascular development," *The International Journal of Developmental Biology,* vol. 55, pp. 399-405, 2011.

[291] K. I. Wiffels, J. H. Kaanders, P. F. Rijken, J. Bussink, F. J. van den Hoogen, H. A. Marres, P. C. de Wilde, J. A. Raleigh and A. J. van der Kogel, "Vascular architecture and hypoxic profiles in human head and neck squamous cell carcinomas," *British Journal of Cancer,* vol. 83, pp. 674-683, 2000.

[292] J. Liu, Y. Wang, Y. Akamatsu, C. C. Lee, R. A. Stetler, M. T. Lawton and G. Y. Yang, "Vascular remodeling after ischemic stroke: mechanisms and therapeutic potentials," *Progress in Neurobiology,* vol. 115, pp. 138-156, 2014.

[293] A. Ergul, M. Abdelsaid, A. Y. Fouda and S. C. Fagan, "Cerebral neovascularization in diabetes: implications for stroke recovery and beyond," *Journal of Cerebral Blood Flow and Metabolism,* vol. 34, pp. 553-563, 2014.

[294] P. Blinder, P. S. Tsai, J. P. Kaufhold, P. M. Knutsen, H. Suhl and D. Kleinfeld, "The cortical angiome: an interconnected vascular network with noncolumnar patterns of blood flow," *Nature Neuroscience,* vol. 16, p. 889, 2013.

[295] J. Steinman, Development of a Novel Imaging Methodology for Quantitative Analysis of the Mouse Cortical Vasculature (MSc Thesis), Toronto: University of Toronto , 2013.

[296] Y. Wang, E. Kilic, U. Kilic, B. Weber, C. L. Bassetti, H. H. Marti and D. M. Hermann, "VEGF overexpression induces post-ischaemic neuroprotection, but facilitates haemodynamic steal phenomena," *Brain,* vol. 128, pp. 52-63, 2005.

[297] T. D. Henry, B. H. Annex, G. R. McKendall, M. A. Azrin, J. J. Lopez, F. J. Giordano, P. K. Shah, J. T. Willerson, R. L. Benza, D. S. Berman, C. M. Gibson, A. Bajamonde, A. C. Rundle, J. Fine and E. R. McCluskey and VIVA Investigators, "The VIVA trial: Vascular endothelial growth factor in Ischemia for Vascular Angiogenesis," *Circulation,* vol. 107, pp. 1359-1365, 2003.

[298] L. Krishnan, C. C. Chang, S. S. Nunes, S. K. Williams, J. A. Weiss and J. B. Hoying, "Manipulating the microvasculature and its microenvironment," *Critical Reviews in Biomedical Engineering,* vol. 41, pp. 91-123, 2013.